UNL-VRTM, A Testbed for Aerosol Remote Sensing: Model Developments and Applications

Xiaoguang Xu and Jun Wang

1 Introduction

The Unified Linearized Vector Radiative Transfer Model (UNL-VRTM) was specifically designed as a testbed for remote sensing of Earth atmosphere and surface, especially for aerosols. Since its debut in 2014 (Wang et al. 2014), UNL-VRTM has been applied to various studies in remote sensing of aerosols, clouds, trace gas, and ground surface. The model itself has also gained many important updates. In this chapter, we aim to provide a comprehensive description of its physics, philosophy, and capabilities, and also to review recent updates and applications.

We begin in Sect. 1.1 with a brief overview of recent advancements in aerosol remote sensing techniques — these provide justification for the necessity to develop a remote sensing testbed tool such as UNL-VRTM. In Sect. 2, we describe the components of the UNL-VRTM forward model with emphasis on the physics of each component and how the components are coupled. Section 3 presents the theory of inverse modeling and information content analysis, which is deployed in UNL-VRTM to provide objective assessments of any observation system. Section 4 reviews recent applications and demonstrates the capabilities of UNL-VRTM in spectroscopic and polarimetric remote sensing of aerosol microphysical properties. In Sect. 5, we highlight the limitations of the model and discuss several ongoing important updates.

X. Xu (✉)
University of Maryland Baltimore County, Baltimore, Maryland, USA
e-mail: xxu@umbc.edu

X. Xu · J. Wang
The University of Iowa, Iowa City, Iowa, USA
e-mail: jun-wang-1@uiowa.edu

A. Kokhanovsky (ed.), *Springer Series in Light Scattering*, Springer Series in Light Scattering, https://doi.org/10.1007/978-3-030-20587-4_1

1.1 Current and Future Aerosol Remote Sensing

Atmospheric aerosols emitted from both natural and anthropogenic sources have diverse impacts on Earth's weather, climate, and environment. On one hand, fine aerosol particles present in ambient air can degrade visibility and pose a hazardous threat to human health (World Health Organization 2017). On the other hand, they affect Earth's energy budget directly by scattering and absorbing solar and terrestrial radiation, and indirectly through changes in cloud formation, lifetime, and radiative properties (Boucher et al. 2013). However, quantification of these effects in current climate models represents the largest uncertainty in estimates of anthropogenic radiative forcing. The global average of the aerosol effective radiative forcing was estimated to range from –0.1 to –1.9 Wm^{-2} with the best estimate of –0.9 Wm^{-2} (Myhre et al. 2013), indicating that the cooling effects of aerosol might partially offset the estimated warming effect of 1.82 ± 0.19 Wm^{-2} caused by the increase of carbon dioxide (CO_2) since the industrial revolution. The climate effects of aerosol particles depend on their geographical distribution, optical properties, and chemical composition. To fully understand the role of aerosol particles in global climate change and to monitor air pollution migration, observations of the global distribution of aerosol properties are highly desirable.

Remote sensing observations from satellite and ground-based platforms have provided key datasets for understanding the role of aerosols in physical processes governing changes of air quality, visibility, surface temperature, clouds, and precipitation (Hoff and Christopher 2009; Kaufman et al. 2002). Global data records of aerosol parameters have emerged on a routine basis since the launch of the Terra satellite in 1999 that carries the Moderate Resolution Imaging Spectroradiometers (MODIS) and the Multi-angle Imaging SpectroRadiometer (MISR) instruments. Following that, the 'A-Train' afternoon constellation of satellites comprises several dedicated satellite sensors in sun-synchronous low-Earth (LEO) orbits (Fig. 1), providing an unprecedented view of the global aerosol system. These sensors include another MODIS instrument on the Aqua platform launched in 2002, Ozone Monitoring Instrument (OMI) on the Aura satellite launched in 2004, POLarization and Directionality of the Earth's Reflectances (POLDER) polarimeter on the PARASOL satellite launched in 2004, and the Cloud-Aerosol Lidar with Orthogonal Polarization (CALIOP) launched in 2006. In addition, the European Envisat satellite launched in 2002 was equipped with several sensors for aerosol retrievals (see a review in Kokhanovsky et al. (2007)), including the MEdium Resolution Imaging Spectrometer (MERIS), the Advanced Along Track Scanning Radiometer (AATSR), and the SCanning Imaging Absorption spectroMeter for Atmospheric CHartographY (SCIAMACHY).

Except for CALIOP, which is an active remote sensing instrument probing the vertical distribution of aerosol lidar backscattering, the other A-train satellites are passive remote sensing instruments and are complementary to each other in their observation strategies and abilities to characterize aerosol parameters. Aside from the usual retrieval of aerosol optical depth (AOD), examples include the additional

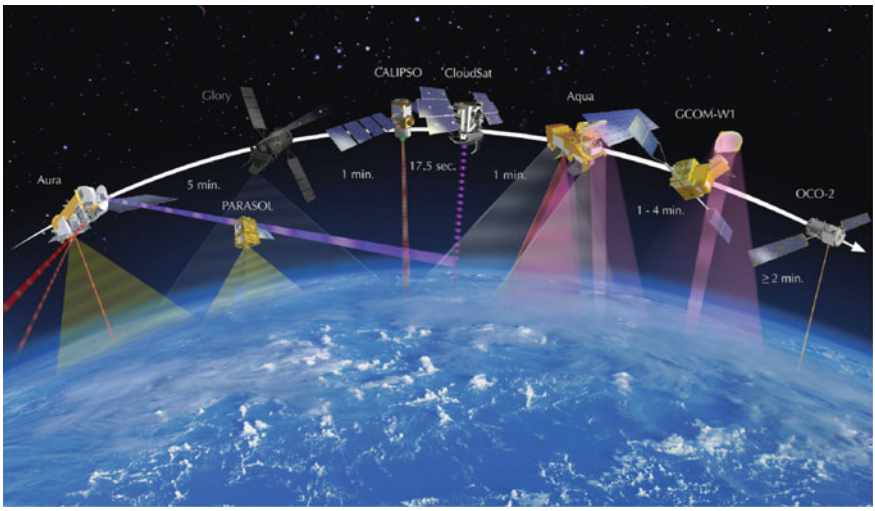

Fig. 1 The A-train afternoon constellation satellites as of 2011. *Source* https://atrain.nasa.gov/

determination of fine- and coarse-mode AOD ratios from MODIS's multispectral radiance data (Levy et al. 2007; Remer et al. 2005), derivation of AOD for non-spherical particles and up to three size modes from the MISR's multispectral multi-angular radiance data (Kahn et al. 1997; Kalashnikova and Kahn 2006), absorbing AODs of high-elevation aerosols from the OMI's ultraviolet (UV) radiance data (Torres et al. 2007), aerosol particle size distribution and refractive index (or single scattering albedo) from POLDER's multispectral multi-angular polarization data (Dubovik et al. 2011; Tanre et al. 2011), and aerosol plume height retrieval over the ocean from MERIS and POLDER radiance measurements in the O_2 A band (Dubuisson et al. 2009). Additionally, the Aerosol Polarimetry Sensor (APS) was designed to provide accurate aerosol microphysical properties from its multi-angular multispectral polarimetric measurements (Mishchenko et al. 2007). Unfortunately, APS was carried by the Glory satellite, which did not reach its orbit in 2011 due to a malfunction on the launch vehicle.

Recent years have seen several more aerosol-related sensors launched, most of which were intended heritage instrument of related A-Train sensors, but with enhanced capabilities. These include the Visible Infrared Imaging Radiometer Suite (VIIRS) onboard the Suomi-NPP and JPSS-1 satellites launched in 2011 and 2017 respectively. VIIRS is a MODIS heritage instrument but with enhanced spatial coverage and the addition of a Day/Night Band (DNB) (Jackson et al. 2013). The VIIRS DNB has been found useful for night-time aerosol monitoring from its measurements over artificial urban lights (McHardy et al. 2015; Wang et al. 2016). The TROPOspheric Monitoring Instrument (TROPOMI), onboard the Sentinel-5P satellite launched in 2017, is a heritage of OMI and SCIAMACHY spectrometers but with a higher spatial resolution and with a spectral range extended to the shortwave

infrared (Veefkind et al. 2012). TROPOMI promises to provide aerosol layer height retrievals along with UV absorbing aerosol properties (Sanders et al. 2015). The Earth Polychromatic Imaging Camera (EPIC) is carried by the Deep Space Climate Observatory (DSCOVR) spacecraft, situated around 1.5 million km distance at the Earth-Sun Lagrange-1 point. EPIC observes the entire sun-lit disk of the Earth every 1–2 h, offering potential for aerosol height retrievals multiple times daily from the measurements in O_2 A and B bands (Xu et al. 2017, 2018).

Ground-based remote sensing, though much more sparsely distributed compared to that from satellite observations, can provide aerosol measurements of higher accuracy. One example is the Aerosol Robotic Network (AERONET). With more than one thousands locations (as of 2019) around the world, most AERONET sites are equipped with an automatic sun and sky scanning spectral radiometer, or the CIMEL-318 type sun photometer, to measure direct and diffuse solar radiation in various atmospheric window channels (Giles et al. 2019; Holben et al. 1998). The direct-sun radiance data are used to infer the spectral AOD, with an uncertainty of about 0.01. The sky radiances are inverted to retrieve aerosol particle size distribution, refractive index, and fraction of non-spherical particles (Dubovik and King 2000; Dubovik et al. 2006). AERONET AOD and inversion products have been widely used to study the regional climatology of aerosol optical properties (Dubovik et al. 2002) and to develop and validate satellite aerosol retrieval algorithms for sensors like MODIS (Levy et al. 2007; Remer et al. 2005).

Progress in aerosol remote sensing during the last two decades suggests that for a full characterization of aerosol optical properties, future satellite missions should rely on a combination of multispectral and multi-angular measurements of radiance and polarization (Mishchenko et al. 2004, 2007). Indeed, supported by recent advancements in the polarimetric aerosol retrieval algorithms [see reviews by Dubovik et al. (2019), Kokhanovsky et al. (2015)], several satellite missions have been planned to launch polarimeters in the next few years (see Dubovik et al. (2019) for a complete list). These include Hyper-Angular Rainbow Polarimeter-2 (HARP-2) and SpexOne on the PACE satellite, Multi-Angle Imager for Aerosols (MAIA) on the OTB-2 satellite (Diner et al. 2018), and Multi-View Multi-Channel Multi-Polarization Imaging (3MI) instrument on the MetOp-SG satellites (Fougnie et al. 2018). Though different in their spectral and angular configurations, these sensors all aim at determination of detailed aerosol particle size distribution and refractive index from multispectral multi-angular polarimetric observations (Dubovik et al. 2019).

In contrast to future sensors based on the polarimertic capability, several other aerosol-related satellite missions are planned to observe aerosols along with trace gases or the Earth's surface from the hyperspectral perspective. These include the TEMPO (Tropospheric EMissions: Monitoring of POllution) instrument (Zoogman et al. 2017), the Geostationary Environment Monitoring Spectrometer (GEMS) mission (Bak et al. 2013), and the Ocean Color Instrument (OCI) of the PACE mission (Omar 2018).

1.2 The Need for a Remote Sensing Testbed

As discussed above, aerosol remote sensing is approaching a new era that embraces both multispectral multi-angular polarimetric and hyperspectral observations. A vital question arises when it comes to designing a new observation system or a new satellite mission: *how can the observation system be optimally configured (in terms the selection of a sensor's spectral wavelengths, view angles, and measured quantities such as radiance and polarization) to fulfill the mission scientific requirements, given the constraints associated with the mission's budget?*

UNL-VRTM was designed to address this kind of question in a cost-effective manner (Wang et al. 2014). It was designed to provide an objective assessment of the aerosol information content resulting from any set of (planned or real) instrument configurations. This capability is achieved through the integrated combination of forward models for particle scattering and radiative transfer together with formal inversion theory that uses a standard set of variables (such as Degree of Freedom for Signal, or DFS) to quantify the retrievable information (Rodgers 2000). Since aerosol retrieval is in essence an inverse problem, formal inversion theory is well suited for the full investigation of aerosol information content for any given set of synthetic or real observation data, and the comprehensive assessment of retrieval accuracy and its dependence on sources of uncertainty in a priori constraints, model parameterizations and intrinsic model assumptions, and instrument error.

As noted in Wang et al. (2014), the UNL-VRTM testbed is expected to address the following challenges in order to manipulate increasingly complicated remote sensing observations:

1. The tool will allow users to incorporate instrument errors and prior constraints in the retrieval and information analysis;
2. The tool will allow users to readily change algorithm definition factors (such as selection of wavelengths and angles);
3. The tool will compute in a direct manner the sensitivity of measured quantities (such as radiance and polarization) with respect to retrieved aerosol parameters (such as coarse/fine-mode AOD, aerosol particle size parameters, refractive indices, and aerosol shape factor, vertical profiles, etc.);
4. The tool should treat the relevant physical processes (such as absorption spectra of trace gases, molecular scattering in the atmosphere, and surface reflectance) in a rigorous manner;
5. The tool will allow for the analysis of information content, degree of freedom for signal and sources of retrieval error for all desired aerosol parameters to be retrieved.

In December 2014, we made the UNL-VRTM version v1.3 package available to the aerosol remote sensing community and public through https://unl-vrtm.org. The website also serves as a platform to broadcast model updates and advance collaborations. As shown in Fig. 2, as of January 2019 the model is applied by over 50 users from 8 countries. It has been used for a wide variety of remote sensing applications

Fig. 2 Map of UNL-VRTM user groups as of January 2019. *Source* https://unl-vrtm.org

not limited for aerosol studies, but also for remote sensing of trace gas, clouds, and ground surfaces.

We have been continuously improving and upgrading the UNL-VRTM capabilities. The current release version is v2.0.2, which includes several major updates from v1.3: (a) extending the spectral range from shortwave-only to thermal infrared (0.2–40 μm); (b) adding the continuum absorption for H_2O, CO_2, O_2, and N_2; (c) enabling calculation of Jacobian with respect to trace gas absorption and mixing ratio; (d) adding a surface reflectance library for typical surface types; (e) enhancing flexibilities for defining sensor configuration; (f) adding interfaces for incorporation into global climate models.

2 The UNL-VRTM Forward Model

As shown in Fig. 3, the UNL-VRTM testbed combines a forward radiative transfer operator that simulates remote sensing observations, and the optimal estimation theory that assesses and inverts the observations. This section focuses on the forward model part, and the inverse modeling and information content analysis are discussed in Sect. 3.

The UNL-VRTM forward model constitutes six components:

1. A vector radiative transfer model, VLIDORT (Spurr 2006);
2. A linearized Mie electromagnetic scattering code (Spurr et al. 2012);
3. A linearized T-matrix electromagnetic scattering code (Spurr et al. 2012);
4. A module computing molecular scattering in the atmosphere;
5. A module computing gaseous absorption in the atmosphere;
6. A module computing various bidirectional reflectance/polarization distribution functions (BRDF/BPDF);

These modules are integrated for the forward calculation of radiation such as the light radiance and state of polarization. Mathematically, the radiation field is described by a Stokes 4-vector (**I**) specified at user-defined spectral wavelengths, atmospheric levels, and viewing directions. As such, the model can be specified to simulate any set of remote sensing measurements from the UV to the thermal IR (the current default wavelength range stretches from 0.2 μm to 40 μm) taken by instruments from satellite, airborne, or ground-based platforms.

The inputs for the forward calculation are (a) spectral and geometrical definitions that characterize specifications of an observing sensor; (b) the profiles of atmospheric properties and constituents (e.g., air temperature, pressure, gaseous mixing ratios, and aerosol concentrations); (c) mono- or multi-modal aerosol microphysical parameters, such as particle size distribution (PSD) and refractive index; (d) parameters characterizing surface reflectance.

One of the outstanding features of the UNL-VRTM model, thanks to the VLIDORT (Spurr 2006) and the linearized Mie/T-matrix scattering codes (Spurr et al. 2012), is the simultaneous calculation of Jacobians of the Stokes vector **I** with respect to a suite of particle, gas, and surface parameters. The latter include (but are not limited to) AOD, aerosol single scattering albedo and phase function, aerosol PSD parameters and refractive index, gas absorption and mixing ratio, and surface reflectance related parameters. The Jacobians, also frequently called weighting functions, can be calculated for both bulk property (total column) and profile parameters, for example, the total-column AOD and profile AODs for individual atmospheric layers.

The UNL-VRTM forward model also features a simple and user-friendly interface (Xu and Wang 2018). We have combined all the modeling options and switches into a single input file, in which users may specify options related to assumptions in radiative transfer modeling, including spectral samplings, atmospheric profiles, air molecular optics, aerosol physical and optical properties, surface property, and variables to be diagnosed, etc. These model settings are grouped into menus with each menu controlling the options for a particular aspect of UNL-VRTM model. Model outputs are saved in a single file of 'netcdf' format. A complementary Python util-

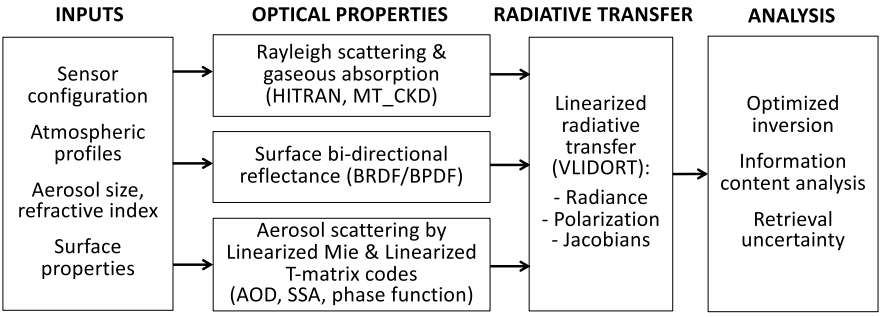

Fig. 3 Flowchart of the UNL-VRTM components. See text for detail

ity package, pyunlvrtm (available at https://github.com/xxu2/pyunlvrtm, accessed 12 Jan 2019), has been developed for efficient processing of UNL-VRTM inputs and simulated data.

In the following text of this section, we start with a brief review of the Stokes-vector parameters used to describe the electromagnetic filed as detected by any remote sensing instrument (Sect. 2.1). Then, we describe the development of the component modules that make up the UNL-VRTM forward model (Sects. 2.2–2.8). Finally, UNL-VRTM benchmark simulations and model verifications are presented in Sect. 2.9.

2.1 Definitions of Stokes Parameters

The radiance and polarization of light at any wavelength can be represented by a Stokes column vector $\mathbf{I}$ having four elements (Hansen and Travis 1974):

$$\mathbf{I} = [I, Q, U, V]^T, \tag{1}$$

where I is the total intensity (or radiance) of the light beam, Q describes the amount of linear horizontal or vertical polarization, U describes the amount of linear polarization at $\pm 45°$, V describes the state of circular polarization, and T indicates the transpose operation. It should be noted that all radiation fields and optical parameters are functions of the light wavelength λ. For simplicity, however, λ is omitted in all formulas of this chapter.

The degree of linear polarization (DOLP) is defined by

$$\text{DOLP} = \frac{\sqrt{Q^2 + U^2}}{I}. \tag{2}$$

The angle of polarization (ψ) is defined to satisfy

$$\tan 2\psi = \frac{U}{Q}, \quad \text{or} \quad \psi = \frac{1}{2}\tan^{-1}\left(\frac{U}{Q}\right) + \psi_0, \tag{3}$$

where $\psi_0 = 0$ if $Q > 0$ and $U \geq 0$; $\psi_0 = \pi$ if $Q > 0$ and $U < 0$; $\psi_0 = \pi/2$ if $Q < 0$.

Stokes parameters are always defined with respect to a plane of reference. Although the choice of a reference plane is arbitrary, observational or theoretical considerations will dictate the use of one plane in preference to the others. For instance, in the solar principal plane, U is negligibly small for a solar beam traveling in a homogeneous atmosphere. In this case, Eq. (2) becomes $\text{DOLP} = -Q/I$.

We often need to convert the Stokes parameters by transforming the plane of reference. Such a transformation can be done with a rotation matrix defined by

$$\mathbf{L}(\alpha) = \begin{bmatrix} 1 & 0 & 0 & 0 \\ 0 & \cos 2\alpha & \sin 2\alpha & 0 \\ 0 & -\sin 2\alpha & \cos 2\alpha & 0 \\ 0 & 0 & 0 & 1 \end{bmatrix}, \tag{4}$$

where α is the angle of rotation, $\alpha \geq 0$. The rotation is *in anti-clockwise when looking in the direction of light propagation* (Hovenier and van der Mee 1983). For Stokes parameters in the new reference plane (denoted by the prime symbol), we can write

$$\mathbf{I}' = \mathbf{L}(\alpha)\mathbf{I}. \tag{5}$$

Stokes parameters I and V are invariant for such a transformation, but Q and U, as well as ψ, will change:

$$Q' = Q\cos 2\alpha + U\sin 2\alpha, \tag{6}$$

$$U' = -Q\sin 2\alpha + U\cos 2\alpha. \tag{7}$$

Equations (6) and (7) show that DOLP is also invariant for the transformation.

In most situations, Stokes parameters measured from satellite polarimeters (such as POLDER) are reported in terms of the local-view meridian plane, i.e., the plane containing scatted beam in the view direction and local surface normal. For specific applications, Q and U often need to be transformed to the solar meridian plane (the plane containing solar beam and surface norm) or the scattering plane (the plane containing solar beam and viewing vector).

Figure 4 illustrates the relationships between the view meridian plane (colored in blue), solar meridian plane (colored in red), and the scattering plane (through *OBA*). Here, the incident solar beam *OA* is specified by an azimuth angle of ϕ_0 and a zenith angle of θ_0. The scattered light is in the view direction OB with an azimuth angle of ϕ and a zenith angle of θ. Points A, B, and Z are located on the unit sphere, with OZ as the local normal. From this sketch, we see that:

- A *rotation of* σ_2 is required to transform the reference plane for the scattered light *from the view meridian plane to the scattering plane*;
- A *rotation of* σ_1 is required to transform the reference plane for the scattered light *from scattering plane to solar meridian plane*;
- A *rotation of* $-(\phi - \phi_0)$ is required to transform the reference plane for the scattered light *from the view meridian plane to the solar meridian plane*. Here we use negative $\phi - \phi_0$ because the rotation is clockwise when looking in the direction of light propagation.

Note that the condition $\pi < \phi - \phi_0 < 2\pi$ is equivalent to f $0 < \phi - \phi_0 < \pi$. And, if $\phi - \phi_0$ equals 0 or π, both the incident and view meridian planes coincide with the scattering plane.

It is convenient to derive these rotation angles in the conventional spherical coordinate system. Indeed, the sides of the spherical triangle *OBA* in Fig. 4 are θ_0, θ, and ξ, facing to its angles are σ_2, σ_1, and $\phi - \phi_0$, respectively. Here, ξ is called phase angle

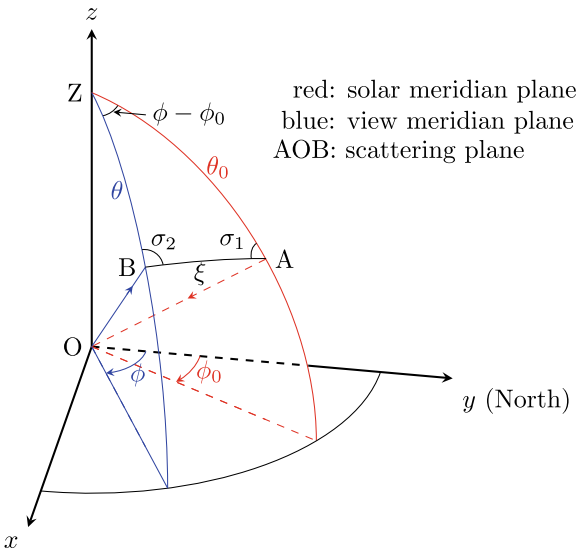

Fig. 4 Illustration of relationships between the meridian planes and the scattering plane. An incident solar beam from A is scattered by a local element at O (e.g., surface or the atmospheric medium). OZ is the local surface normal. The direction of incident light is AO specified by an azimuth angle of ϕ_0 and a zenith angle of θ_0. The scattered light is in the direction of OB with an azimuth angle of ϕ and a zenith angle of θ. Hence, the scattering plane is through AOB; view and solar meridian planes are blue and red, respectively. Points A, B, and Z are located on the unit sphere. After Fig. 3 of Hovenier and van der Mee (1983)

of scattering, which is supplementary to the scattering angle Θ, i.e., $\xi = \pi - \Theta$. From spherical trigonometry, these angles satisfy

$$\cos\xi = \cos\theta_0 \cos\theta + \sin\theta_0 \sin\theta \cos(\phi - \phi_0), \tag{8}$$

$$\cos\sigma_1 = \frac{\cos\theta - \cos\theta_0 \cos\xi}{\sin\theta_0 \sin\xi}, \tag{9}$$

$$\cos\sigma_2 = \frac{\cos\theta_0 - \cos\theta \cos\xi}{\sin\theta \sin\xi}. \tag{10}$$

From the spherical sine law, we have in addition

$$\frac{\sin\sigma_1}{\sin\theta} = \frac{\sin\sigma_2}{\sin\theta_0} = \frac{\sin(\phi - \phi_0)}{\sin\xi} \tag{11}$$

From Eqs. (8)–(11), one thus can determine the rotation matrix to transform the Stokes vector over the angle of σ_1(and similarly for σ_2) by using

$$\cos 2\sigma_1 = 2\cos^2\sigma_1 - 1, \tag{12}$$

$$\sin 2\sigma_1 = 2\sin\sigma_1 \cos\sigma_1. \tag{13}$$

2.2 The Vector Radiative Transfer with VLIDORT

The radiative transfer solver in the current UNL-VRTM is the Vector Linearized Discrete Ordinate Radiative Transfer (VLIDORT) model version 2.6 developed by Spurr (2006). VLIDORT is a linearized pseudo-spherical vector discrete ordinate radiative transfer model for multiple scattering of diffuse radiation in a stratified multi-layer atmosphere. It computes four elements of the Stokes vector **I** for down-welling and upwelling radiation at any desired atmospheric level. The VLIDORT includes the pseudo-spherical approximation to calculate solar beam attenuation in a curved medium. It also uses the delta-M approximation for dealing with sharply peaked forward scattering. In addition, the VLIDORT package contains a kernel-based BRDF implementation for both the scalar and vector surface reflection (Spurr 2004).

With its full linearization facility, VLIDORT simultaneously computes the Jacobians of **I** with respect to any specified total-column or profile atmospheric quantity or with respect to any surface property. Details on the linearization of the vector radiative transfer solutions are addressed in Spurr (2006). As discussed in Sect. 2.8 below, such Jacobian calculations require specifications of linearized optical property inputs.

With an atmospheric parameter noted by x, the Jacobian vector with respect to x calculated by VLIDORT is given by

$$\mathbf{k} = x\frac{\partial \mathbf{I}}{\partial x}. \tag{14}$$

Here, atmospheric-property Jacobians are normalized derivatives. It shoud be noted that VLIDORT surface-property Jacobians are unnormalized. Essentially, the above equation yields the derivatives of radiance I and DOLP with respect to x, i.e., $\frac{\partial I}{\partial x}$ and $\frac{\partial \mathrm{DOLP}}{\partial x}$. While obtaining $\frac{\partial I}{\partial x}$ is straightforward, $\frac{\partial \mathrm{DOLP}}{\partial x}$ can be derived from Eq. (2) as

$$\frac{\partial \mathrm{DOLP}}{\partial x} = -\frac{\mathrm{DOLP}}{I}\frac{\partial I}{\partial x} + \frac{Q\frac{\partial Q}{\partial x} + U\frac{\partial U}{\partial x}}{I\sqrt{Q^2+U^2}}. \tag{15}$$

2.2.1 Theoretical Basis of Vector RTE

Here we briefly describe the vector radiative transfer equation (RTE) solved by VLIDORT in a theoretical context. Let $\mathbf{I}_0 = [I_0, 0, 0, 0]^T$ denote the Stokes vector for incident solar radiation at the top of the atmosphere (TOA) from the direction (θ_0, ϕ_0), where θ_0 and ϕ_0 are the incident solar zenith and azimuth angles, respectively. For a plane-parallel atmosphere, the vector RTE in atmospheric medium for the Stokes vector **I** of light propagating in the viewing direction (θ, ϕ) can be written (Hovenier et al. 2004; Mishchenko et al. 2002):

$$\mu \frac{\partial \mathbf{I}(\tau, \mu, \phi)}{\partial \tau} = \mathbf{I}(\tau, \mu, \phi) - \mathbf{J}(\tau, \mu, \phi; \mu_0, \phi_0), \tag{16}$$

where the vector source term $\mathbf{J}$ in shortwave has the form:

$$\mathbf{J}(\tau, \mu, \phi; \mu_0, \phi_0) = \frac{\omega}{4\pi} \int_{-1}^{1} \int_{0}^{2\pi} \mathbf{Z}(\mu, \mu_0, \Delta\phi)\mathbf{I}(\tau, \mu_0, \phi_0)\mathrm{d}\phi_0 \mathrm{d}\mu_0 + \frac{\omega}{4\pi} \mathbf{Z}(\mu, \mu_0, \Delta\phi)\mathbf{I}_0 \exp(-\tau/\mu_0). \tag{17}$$

Here, τ is the extinction optical depth measured from TOA, $\Delta\phi = \phi - \phi_0$ is the relative azimuth angle, μ and μ_0 are cosines of θ and θ_0, respectively, ω is the single scattering albedo and $\mathbf{Z}$ is the phase matrix of scattering by the medium. It should be noted that the relative azimuth angle for VLIDORT input is defined as $\pi - \Delta\phi$ for the case shown in Fig. 4. The first term on the right-hand side of Eq. (17) represents multiple scattering contributions, while the second indicates homogeneous light source scattered by atmospheric medium from the attenuated solar beam.

Matrix $\mathbf{Z}$ relates scattering and incident light with respect to the *meridian* planes, i.e., the plane containing surface normal and incident or scattered beam, which is also the plane of reference defined for Stokes vector of incident light or scattered beam, respectively. The equivalent matrix for Stokes vectors with respect to the *scattering* plane is the phase matrix $\mathbf{F}$. In general, $\mathbf{F}$ depends on the scattering angle Θ between the incident and scattered beam. Matrix $\mathbf{Z}$ is related to $\mathbf{F}(\Theta)$ through application of two rotation matrices (Hovenier et al. 2004):

$$\mathbf{Z}(\mu, \mu_0, \Delta\phi) = \mathbf{L}(\pi - \sigma_2)\mathbf{F}(\Theta)\mathbf{L}(-\sigma_1). \tag{18}$$

The first rotation over the angle $-\sigma_1$ transforms the incident beam's plane of reference from incident meridian plane into scattering plane, and then the second rotation over an angle of $\pi - \sigma_2$ to transforms the scattered beam's plane of reference from the scattering plane to the scattered meridian plane. The rotation angles $-\sigma_1$ and $\pi - \sigma_2$ can be determined from incident and viewing geometries. Indeed, such a transformation is analogous to (but in the reverse seqnse) the rotation of Stokes parameters from view meridian plane to scattering plane and then to the solar meridian plane. The rotation angles here have an opposite sign to those defined in Fig. 4. The rotation matrix is same to the one defined by Eq. (4), which satisfies $\mathbf{L}(\pi - \sigma) = \mathbf{L}(-\sigma)$.

For a medium containing a collection of randomly oriented mirror-symmetric particles (such as homogeneous spheres, spheroids, or cylinders), the scattering phase matrix is a function of scattering angle only and has at most six independent elements (Hansen and Travis 1974),

$$\mathbf{F}(\Theta) = \begin{bmatrix} a_1(\Theta) & b_1(\Theta) & 0 & 0 \\ b_1(\Theta) & a_2(\Theta) & 0 & 0 \\ 0 & 0 & a_3(\Theta) & b_2(\Theta) \\ 0 & 0 & -b_2(\Theta) & a_4(\Theta) \end{bmatrix}. \tag{19}$$

By definition, $a_1(\Theta)$ is the scalar scattering phase function, which satisfies

$$\int_{4\pi} a_1(\Theta) d\Omega = 4\pi, \tag{20}$$

where Ω indicates the solid angle.

In solving the vector RTE with the discrete ordinates method in VLIDORT, it is advantageous to expand the scattering phase matrix elements in terms of generalized spherical function denoted by $P^j_{m,n}(\cos\Theta)$ (Hovenier et al. 2004):

$$a_1(\Theta) = \sum_{j=0}^{J} \beta_j P^j_{0,0}(\cos\Theta), \tag{21}$$

$$a_2(\Theta) + a_3(\Theta) = \sum_{j=2}^{J} (\alpha_j + \zeta_j) P^j_{2,2}(\cos\Theta), \tag{22}$$

$$a_2(\Theta) - a_3(\Theta) = \sum_{j=2}^{J} (\alpha_j - \zeta_j) P^j_{2,-2}(\cos\Theta), \tag{23}$$

$$a_4(\Theta) = \sum_{j=0}^{J} \delta_j P^j_{0,0}(\cos\Theta), \tag{24}$$

$$b_1(\Theta) = \sum_{j=2}^{J} \gamma_j P^j_{0,2}(\cos\Theta), \tag{25}$$

$$b_2(\Theta) = -\sum_{j=2}^{J} \varepsilon_j P^j_{0,2}(\cos\Theta). \tag{26}$$

The above expansion coefficients in these phase matrix elements can thus be expressed by a matrix with six sets of "Greek" constants for each moment j, known as the "Greek matrix" (Spurr 2006):

$$\mathbf{B}^j = \begin{bmatrix} \beta_j & \gamma_j & 0 & 0 \\ \gamma_j & \alpha_j & 0 & 0 \\ 0 & 0 & \zeta_j & -\varepsilon_j \\ 0 & 0 & \varepsilon_j & \delta_j \end{bmatrix}. \tag{27}$$

Conversely, a set of Greek matrices $\mathbf{B}^j$ for $0 \le j \le J$ can be used to reconstruct the scattering phase matrix $\mathbf{F}(\Theta)$. Reproduction of the phase matrix is less accurate with fewer moments (J). Note that the generalized spherical functions are additive, i.e., the jth Greek matrix for the sum of two scattering matrices $a\mathbf{F}_1(\Theta) + b\mathbf{F}_2(\Theta)$ is $a\mathbf{B}^j_1 + b\mathbf{B}^j_2$, given $\mathbf{B}^j_1$ as the jth Greek matrix for $\mathbf{F}_1(\Theta)$ and $\mathbf{B}^j_2$ for $\mathbf{F}_2(\Theta)$. This feature is important when combining the scattering matrices of different media, for instance, the molecular and particle scattering.

2.2.2 VLIDORT Optical Property Inputs

Based on the above discussion, we can see that the input optical parameters required to solve the RTE (16) are the layer optical depth τ, the layer single scattering albedo ω, and the layer Greek matrix $\langle \mathbf{B}^j \rangle_{j=0\ldots J}$ at each atmospheric layer, plus the reflection matrix $\mathbf{R}(\mu, \mu_0, \Delta\phi)$ of the underlying surface. These quantities are exactly the inputs required by VLIDORT. Here, $<>_{j=0,J}$ denotes a set that consists of elements having the similar expression as that inside $<>$ but for $j = 0 \ldots J$. Matrix $\mathbf{R}$ is defined as the boundary condition at the bottom of the atmosphere, which relates the downwelling and upwelling radiation fields at surface level (Sect. 2.7).

Here we use $\left[\tau, \omega, \langle \mathbf{B}^j \rangle_{j=0\ldots J}\right]$ to denote the optical property set being supplied to VLIDORT. Considering a cloud-free atmosphere, the solar radiation is attenuated by molecular scattering, gaseous absorption, and aerosol scattering and absorption. For a given layer, we thus have the optical property set given by

$$\tau = \tau_{\mathrm{A}} + \tau_{\mathrm{R}} + \tau_{\mathrm{G}}, \tag{28}$$

$$\omega = \frac{\tau_{\mathrm{A}}\omega_{\mathrm{A}} + \tau_{\mathrm{R}}}{\tau}, \tag{29}$$

$$\langle \mathbf{B}^j \rangle_{j=0\ldots J} = \frac{\tau_{\mathrm{A}}\omega_{\mathrm{A}}}{\tau_{\mathrm{A}}\omega_{\mathrm{A}} + \tau_{\mathrm{R}}} \langle \mathbf{B}_{\mathrm{A}}^j \rangle_{j=0\ldots J} + \frac{\tau_{\mathrm{R}}}{\tau_{\mathrm{A}}\omega_{\mathrm{A}} + \tau_{\mathrm{R}}} \langle \mathbf{B}_{\mathrm{R}}^j \rangle_{j=0\ldots J}, \tag{30}$$

where τ_{A}, τ_{R}, and τ_{G} are optical depth of aerosol extinction, Rayleigh scattering of air density fluctuations, and gaseous absorption, respectively. ω_{A} is the aerosol single scattering albedo. $\langle \mathbf{B}_{\mathrm{A}}^j \rangle_{j=0\ldots J}$ and $\langle \mathbf{B}_{\mathrm{R}}^j \rangle_{j=0\ldots J}$ are the sets of Greek matrix coefficients that characterize the scattering phase matrix elements for aerosol particles $\mathbf{F}_{\mathrm{A}}(\Theta)$ and Rayleigh scattering $\mathbf{F}_{\mathrm{R}}(\Theta)$, respectively. The forward modeling development thus requires the computation of single scattering properties for aerosols and air density fluctuations, a rigorous treatment for absorption of trace gases, an accurate representation of reflectance/polarization by surface, and the realistic simulation of polarimetric radiative transfer.

To enable VLIDORT to compute Jacobians, additional inputs are needed — these are the linearized versions of set of optical property inputs, that is, the partial derivatives of these inputs with respect to the desired Jacobian parameter(s). Specification of linearized inputs is dealt with in Sect. 2.8.

2.3 Atmospheric Profiles

Here, the term "atmospheric profile" refers to vertical distribution of air temperature, pressure, and air number density at each atmospheric layer. In UNL-VRTM, the profile also considers the gaseous and particle constituents at each atmospheric layer, including mixing ratio of trace gases, and concentration of aerosols (or clouds) in each atmospheric layer.

We have implemented profiles for six standard atmospheres from the database of McClatchey et al. (1972): (1) Tropical, (2) Mid-Latitude Summer, (3) Mid-Latitude Winter, (4) High-Latitude Summer, (5) High-Latitude Winter, and (6) US standard 1976. Each atmosphere has vertical profiles of pressure, temperature, and mixing ratios for eight gases (H_2O, CO_2, O_3, N_2O, CO, CH_4, O_2, and NO). From the same database, we have also implemented a set of common profiles for other 14 trace gases: SO_2, NO_2, NH_3, HNO_3, OH, HF, KCl, HBr, HI, ClO, OCS, H_2CO, HOC_1, and N_2. Figure 5 shows the mixing ratio of these 22 gases for the Mid-Latitude Summer atmosphere.

Starting with this set of standard atmospheres, users have the flexibility to scale the columnar amount of each gas by setting a scaling factor in the model input. For instance, although the CO_2 mixing ratio is 330 ppm for these standard atmospheres, this value should really be set to a more modern concentration level (e.g., about 400 ppm in 2015) when simulating IR observations in the CO_2 bands. Alternatively, the user may specify the pressure-temperature profile and mixing ratios of any gases from other data sources, such as atmospheric sounding data or global model simulations.

The vertical distribution of the particulate medium in the atmosphere also needs to be defined. This can be supplied either by the user as a dedicated model input, or it can defined by one of a set of pre-specified aerosol profile types. As we will see in Sect. 2.6, the particulate medium may have one or two modes, with vertical loading profiles treated independently for each mode. We have implemented three aerosol-loading vertical profiles in UNL-VRTM; these include uniform, exponential-decreasing, and quasi-Gaussian profile shapes. For the uniform profile, aerosols

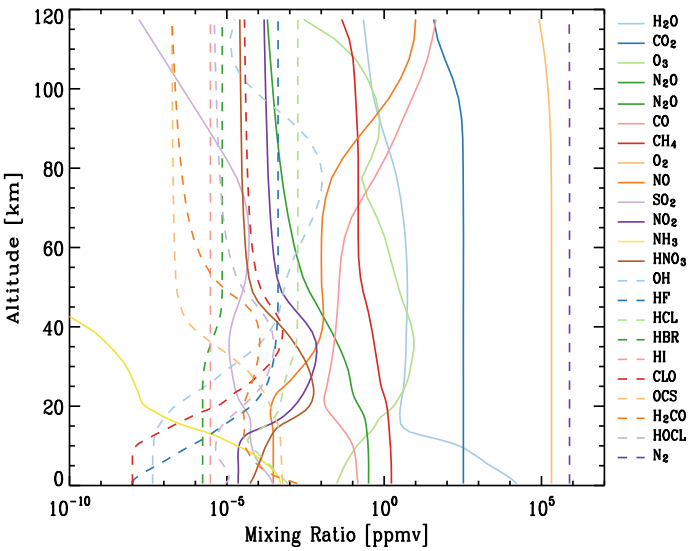

Fig. 5 Profile of trace gas mixing ratios for the Mid-Latitude Summer atmosphere

are assumed evenly distributed with height. The AOD profile for the exponential-decreasing case follows the form

$$\int_{z}^{+\infty} \tau_{\mathrm{A}}(z)\mathrm{d}z = \tau_{\mathrm{a0}} \exp\left(-\frac{z}{H_{\mathrm{s}}}\right) \tag{31}$$

where τ_{a0} is the columnar AOD, and H_s is a scale height parameter. The quasi-Gaussian profile is derived from a generalized distribution function (Spurr and Christi 2014)

$$\tau_{\mathrm{A}}(z) = C\frac{\exp(-\gamma|z - z_{\mathrm{peak}}|)}{[1 + \exp(-\gamma|z - z_{\mathrm{peak}}|)]^2} \tag{32}$$

where C is a constant related to τ_{a0}, γ is related to the half-width constant σ through $\gamma = \ln(3 + \sqrt{8})/\sigma$, and z_{peak} is the height with peak aerosol concentration.

2.4 Gaseous Absorption

The absorption optical depth (τ_{G}) of any atmospheric layer for K different trace gases is given by

$$\tau_{\mathrm{G}} = \Delta H \sum_{i=1}^{K} N_{\mathrm{gas},i}\sigma_{\mathrm{G},i}(T, P) \tag{33}$$

where ΔH is the thickness (cm) of the layer, $N_{\mathrm{gas},i}$ is the number density of ith gas (molec cm^{-3}), and $\sigma_{\mathrm{G},i}$ is the corresponding absorption cross section (cm^{2}molec^{-1}), a function of temperature and pressure.

UNL-VRTM currently accounts for absorptions by a total of 22 trace gases (Sect. 2.3). The determination of σ_{G} for each gas is based on three data sources, namely, the HITRAN (2012) line-spectroscopic database for all of these 22 gases (Rothman et al. 2009, 2013); the cross-section library complementary to HITRAN for O_3, NO_2, SO_2, O_2–O_2, and H_2CO in UV and visible (Orphal and Chance 2003); continuum absorption by H_2O, CO_2, O_2, and N_2 modeled with the MT_CKD approach (Clough et al. 1989; Mlawer et al. 2012). Below, we briefly review the calculation of cross sections from HITRAN line spectroscopy data, using an accurate Voigt profile code kindly provided by Dr. Kelly Chance.

The HITRAN database provides line-spectroscopic absorption parameters that account for the temperature correction of line intensity and pressure-shift correction of line position. These parameters include resonant frequency ν_0 in units of cm^{-1}, the spectral line intensity per absorbing molecule S (cm^{-1}cm^{2}molec^{-1}), the Lorentz line width parameter α_0 (cm^{-1}atm^{-1}), and the energy of lower state E_η (cm^{-1}). In the lower atmosphere where Lorentz broadening dominates, the extinction cross section for a gas molecule (cm^{2}molec^{-1}) at a specific frequency ν is (Liou 2002):

$$k_\alpha(\nu) = \frac{S}{\pi}\frac{\alpha}{(\nu-\nu_0)^2+\alpha^2} = Sf(\nu-\nu_0), \tag{34}$$

where α is the half width of the line at half-maximum (HWHM) and $f(\nu-\nu_0)$ is called shape factor of a spectral line. By definition,

$$\int_{-\infty}^{\infty} k(\nu)d\nu = S. \tag{35}$$

In the HITRAN database, values for α_0 and S are stored for reference values of pressure 1013.25 hPa and temperature T_0 296.15 K. Line intensity at other atmospheric pressures and temperatures is calculated through

$$S(T) = S(T_0)\frac{Q(T_0)}{Q(T)}\frac{e^{-c_2E_\eta/T}}{e^{-c_2E_\eta/T_0}}\frac{1-e^{-c_2\nu_0/T}}{1-e^{-c_2\nu_0/T_0}}, \tag{36}$$

where $c_2 = hd/k = 1.4388$ (cm K) is the second radiation constant. Here h, d, and k are the Planck constant, speed of light, and the Boltzmann constant, respectively. The partition function $Q(T)$ is determined from third-degree Lagrange interpolation of the HITRAN partition sums database, which was reorganized and shortened to include only the Earth atmospheric temperature range of 148–342 K.

The calculation of α also needs to account for the effect of temperature and pressure:

$$\alpha(p,T) = \left(\frac{T_0}{T}\right)^n \left[\alpha_{\text{air}}(P_0,T_0)(p-p_s) + \alpha_{\text{self}}(P_0,T_0)p_s\right], \tag{37}$$

where α_{air} and α_{self} are the HWHM for air broadening and self-broadening, respectively; p and p_s are the air pressure and partial pressure for that gas molecule (both normalized to the standard pressure P_0), respectively. For most applications, α_{self} can be assumed equal to α_{air}, and hence:

$$\alpha(p,T) = \left(\frac{T_0}{T}\right)^n \alpha_{\text{air}}(P_0,T_0)p. \tag{38}$$

From Eqs. (36) and (38), one can compute the absorption cross-section of each gas at any temperature and pressure:

$$k(\nu) = \frac{S(T)}{\pi}\frac{\alpha(p,T)}{[\nu-(\nu_0+\delta p)]^2+\alpha^2(p,T)}, \tag{39}$$

where δ is the air-broadened pressure shift (in the units of $\text{cm}^{-1}\text{atm}^{-1}$) from HITRAN dataset. Again, p is pressure normalized to the reference 1013.25 hPa.

Equation (38) can only be applied to the lower atmosphere. In the upper atmosphere, the Doppler broadening becomes important. The width for Doppler broad-

ening is:

$$\alpha_{\mathrm{D}} = \frac{\nu_0}{c}\left(\frac{2kT}{m}\right)^{\frac{1}{2}} = 4.30140 \times 10^{-7}\left(\frac{T}{M}\right)^{\frac{1}{2}}, \tag{40}$$

where M is the molecular weight, k is the Boltzmann constant, and m is the molecular mass The HWHM for Doppler broadening is $\sqrt{2}\alpha_{\mathrm{D}}$ and the molecular absorption cross section due to Doppler broadening is

$$k_{\alpha_{\mathrm{D}}}(\nu) = \frac{S}{\alpha_{\mathrm{D}}\sqrt{\pi}} e^{-\left(\frac{\nu-\nu_0}{\alpha_{\mathrm{D}}}\right)^2}. \tag{41}$$

Lorentz and Doppler line shapes are convolved in the Voigt profile (Liou 2002):

$$f(\nu-\nu_0) = \frac{1}{\alpha_{\mathrm{D}}\sqrt{\pi}}\frac{y}{\pi}\int_{-\infty}^{\infty}\frac{1}{y^2+(x-t)^2}e^{-t^2}dt, \tag{42}$$

where $y = \alpha/\alpha_{\mathrm{D}}$ and $x = (\nu-\nu_0)/\alpha_{\mathrm{D}}$. In our code, the calculation of Voigt profiles follows the method of Gautschi (1970).

2.5 Rayleigh Scattering

The Rayleigh scattering optical depth (τ_{R}) at a given wavelength in any atmospheric layer is computed via

$$\tau_{\mathrm{R}} = N_{\mathrm{air}}\Delta H\sigma_{\mathrm{R}}, \tag{43}$$

where N_{air} is the air molecular number density of that layer (molec cm^{-3}), and ΔH is the layer thickness (cm), and σ_{R} is the Rayleigh scattering cross-section (cm^2 molec^{-1}) computed following (Bodhaine et al. 1999):

$$\sigma_{\mathrm{R}} = \frac{24\pi^3(n_{\mathrm{s}}^2-1)^2}{\lambda^4 N_{\mathrm{s}}^2(n_{\mathrm{s}}^2+2)^2}\left(\frac{6+3\rho}{6-7\rho}\right). \tag{44}$$

Here, n_{s} and N_{s} respectively are the refractive index and molecular number density of standard atmosphere at the temperature of 288.15 K and pressure of 1013.25 hPa, λ is the wavelength (in centimeters) of incident light, and ρ is the depolarization factor related to the molecular anisotropy. The term $(6+3\rho)/(6\text{-}7\rho)$ is known as the King or F factor. Indeed, ρ is the ratio of light intensity parallel and perpendicular to the plane of scattering. For isotropic Rayleigh scattering $\rho = 0$, and in general $\rho \approx 0.03$ for air. As will be shown, ρ is determined by the King factor values of the primary gases in the atmosphere.

In our tool, we set N_s as 2.546899×10^{19} molec cm^{-3} and parameterize n_s as a function of λ (Bodhaine et al. 1999):

$$n_s = 1 + \left[10^{-8} \times \left(8060.51 + \frac{2480990}{132.274 - \lambda^{-2}} + \frac{17455.7}{39.32957 - \lambda^{-2}}\right)\right] \times \left[1 + 0.54(C_{CO_2} - 0.0003)\right]. \quad (45)$$

Note in Eq. (45), the units of λ is micrometers (μm). The term in the first square bracket on the right is the refractive index of dry air with the mixing ratio of CO_2 of 300 ppm for the standard atmosphere; the term in the second square bracket accounts for the change of air refractive index as a function of CO_2 mixing ratio, expressed by C_{CO_2} in the units of parts per volume.

The F-factor of air is computed as sum of F-factors for the four most abundant gases (i.e., N_2, O_2, Ar, and CO_2) in the atmosphere weighted by their corresponding mixing ratios (Bodhaine et al. 1999):

$$F_{air} = \frac{78.084F_{N_2} + 20.946F_{O_2} + 0.934F_{Ar} + 100C_{CO_2}F_{CO_2}}{78.084 + 20.946 + 0.934 + 100C_{CO_2}} \quad (46)$$

where F_{N_2}=$1.034 + 3.17 \times 10^{-4}\lambda^{-2}$, $F_{O_2} = 1.096 + 1.385 \times 10^{-3}\lambda^{-2} + 1.448 \times 10^{-4}\lambda^{-4}$, $F_{Ar} = 1.0$, and $F_{CO_2} = 1.15$, and λ is expressed in the units of μm. From F_{air} one can determine the depolarization factor ρ, i.e., $\rho = (6F_{air} - 6)/(7F_{air} + 3)$.

Note that in Eq. (44), the refractive index and molecular number density do not need to be specified as parameters for the standard atmosphere, as long as they are consistent and expressed for the same temperature and pressure. However, as shown by Penndorf (1957), $(n_s^2 - 1)^2(n_s^2 + 2)^{-2}$ is proportional to N_s^2 regardless of whether n_s and N_s are values for the standard atmosphere or not. Hence, σ_R computed from Eq. (44) for the standard atmosphere can be used for most optical applications that deal with ambient atmospheres with varying temperature and pressure (Bodhaine et al. 1999).

The phase matrix for Rayleigh scattering is (Hansen and Travis 1974):

$$\mathbf{F}_R(\Theta) = a\begin{bmatrix} \frac{3}{4}(1+\cos^2\Theta) & -\frac{3}{4}\sin^2\Theta & 0 & 0 \\ -\frac{3}{4}\sin^2\Theta & \frac{3}{4}(1+\cos^2\Theta) & 0 & 0 \\ 0 & 0 & \frac{3}{2}\cos\Theta & 0 \\ 0 & 0 & 0 & \frac{3b}{2}\cos\Theta \end{bmatrix} + (1-a)\begin{bmatrix} 1 & 0 & 0 & 0 \\ 0 & 0 & 0 & 0 \\ 0 & 0 & 0 & 0 \\ 0 & 0 & 0 & 0 \end{bmatrix}, \quad (47)$$

where Θ is the scattering angle, and parameters a and b accounts for molecular anisotropy:

$$a = \frac{1-\rho}{1+\rho/2}, \quad b = \frac{1-2\rho}{1-\rho}, \tag{48}$$

Neglecting molecular anisotropy implies that a and b are unity for $\rho = 0$, and Eq. (47) reduces to the phase matrix for isotropic Rayleigh scattering. With the aid of Eqs. (21)–(26), one can show that $\mathbf{F}_{\mathrm{R}}(\Theta)$ is fully represented by a 3-term spherical-function expansion using the following three "Greek" matrices (Hovenier et al. 2004; Spurr 2006):

$$\langle \mathbf{B}_{\mathrm{R}}^{j} \rangle_{j=0\ldots2} = \begin{bmatrix} 1 & 0 & 0 & 0 \\ 0 & 0 & 0 & 0 \\ 0 & 0 & 0 & 0 \\ 0 & 0 & 0 & 0 \end{bmatrix}_{j=0}, \begin{bmatrix} 0 & 0 & 0 & 0 \\ 0 & 0 & 0 & 0 \\ 0 & 0 & 0 & 0 \\ 0 & 0 & 0 & \frac{3(1-2\rho)}{2+\rho} \end{bmatrix}_{j=1},$$
$$\text{and} \begin{bmatrix} \frac{1-\rho}{2+\rho} & -\frac{\sqrt{6}(1-\rho)}{2+\rho} & 0 & 0 \\ -\frac{\sqrt{6}(1-\rho)}{2+\rho} & \frac{6(1-\rho)}{2+\rho} & 0 & 0 \\ 0 & 0 & 0 & 0 \\ 0 & 0 & 0 & 0 \end{bmatrix}_{j=2}. \tag{49}$$

2.6 *Aerosol Single Scattering*

Aerosol single scattering properties necessary for radiative transfer calculations include the aerosol optical depth τ_{A} that is related to the extinction efficiency factor Q_{ext}, the aerosol single scattering albedo ω_{A}, and the scattering phase matrix $\mathbf{F}_{\mathrm{A}}(\Theta)$ as represented by the set of "Greek" matrices $\langle \mathbf{B}_{\mathrm{A}}^{j} \rangle_{j=0\ldots J}$. Calculation of these properties is done using a Linearized Mie (LMIE) scattering code for spherical particles and a Linearized T-matrix (LTMATRIX) scattering code for non-spherical convex and axially symmetric particles (Spurr et al. 2012). The LMIE code originates from the Mie code of de Rooij et al. (1984), and the LTMATRIX code originates from the T-Matrix code developed by Mishchenko and Travis (1998); both codes include a full linearization capability as implemented by Spurr et al. (2012).

Shared inputs for both codes are the parameters describing *aerosol microphysics*: the complex refractive index $(m_{\mathrm{r}} + im_{\mathrm{i}})$ at spectral wavelengths and the particle size distribution (PSD) parameters. The codes have several analytical functions that are commonly used to model natural aerosol *number PSDs*; these include the so-called 'gamma', 'modified gamma', 'lognormal', and 'power law' size distributions (Mishchenko and Travis 1998; Spurr et al. 2012). Each PSD function is characterized by two or three non-linear "PSD parameters". Expressions for these PSD functions and their associated PSD parameters are presented in Appendix 1. For non-spherical particles, the specified PSD is interpreted as surface-area equivalent spheres in the linearized T-matrix calculation, regardless of particle shape.

In the present version of UNL-VRTM, aerosol particles are described by one or two size modes, with each mode following one of after-mentioned PSDs. For instance, studies have shown that the size range of aerosol particles often follows a bi-modal lognormal distribution:

$$\frac{\mathrm{d}V}{\mathrm{d}\ln r} = \sum_{i=1}^{2} \frac{V_0^i}{\sqrt{2\pi}\ln\sigma_\mathrm{g}^i} \exp\left[-\frac{(\ln r - \ln r_\mathrm{v}^i)^2}{2\ln^2\sigma_\mathrm{g}^i}\right], \tag{50}$$

where V_0, r_v, and σ_g are the total volume concentration, geometric *volume* median radius, and geometric standard deviation, respectively. The superscript i indicates the size mode. Particle size ranges from 0.01 to 10 μm for the fine mode and from 0.05 to 20 μm for the coarse mode will cover >99.9% of the total volume. An advantage of the lognormal distribution is that standard deviations for the *number*, *area*, and *volume* PSD functions are identical, allowing that the median radii for these PSD functions to be converted from one to another (Seinfeld et al. 2006). For instance, the volume median radius r_v relates to the number geometric median radius r_g by $r_\mathrm{v} = r_\mathrm{g}\exp(3\ln^2\sigma_\mathrm{g})$ (see Appendix 1 for details.)

The LMIE and LTMATRIX codes compute the aerosol extinction efficiency factor Q_ext, single scattering albedo ω_A, and phase matrix $\mathbf{F}(\Theta)$, as well as partial derivatives of these quantities with respect to input parameters including r_eff, v_eff, m_r, and m_i. The phase matrix and its derivatives are expressed in terms of the expansion coefficients $\langle \mathbf{B}_\mathrm{A}^j \rangle_{j=0\ldots J}$ for each moment j. Let $\boldsymbol{\Lambda}$ denotes the vector of aerosol microphysical parameters, $\boldsymbol{\Lambda} = [V_0, r_\mathrm{eff}, v_\mathrm{eff}, m_\mathrm{r}, m_\mathrm{i}]^T$, and $\mathbf{M}$ the vector of aerosol optical parameters, $\mathbf{M} = [\tau_\mathrm{A}, \omega_\mathrm{A}, \langle \mathbf{B}_\mathrm{A}^j \rangle_{j=0\ldots J}]^T$, where τ_A is related to Q_ext through $\tau_\mathrm{A} = \frac{3V_0 Q_\mathrm{ext}}{4r_\mathrm{eff}}$. The LMIE/LTMATRIX codes act as operators mapping vector $\boldsymbol{\Lambda}$ to $\mathbf{M}$. The Jacobian matrix of $\mathbf{M}$ with respect to $\boldsymbol{\Lambda}$, or $\frac{\partial \mathbf{M}}{\partial \boldsymbol{\Lambda}}$, is calculated by means of the LMIE/LTMATRIX linearization capability.

2.7 Surface Reflection Models

The intrinsic reflectance properties of surface can be represented by a 4 × 4 reflection matrix $\mathbf{R}(\mu, \mu_0, \Delta\phi)$, which is a function of incident angle, reflected angle, and spectral wavelength. It describes the connection between the Stokes vector of reflected and incident light at the atmosphere-surface boundary:

$$\mathbf{I}_\mathrm{s}(\mu, \phi) = \mathbf{R}(\mu, \mu_0, \Delta\phi)\mathbf{I}_\mathrm{s}^\mathrm{inc}(\mu_0, \phi_0), \tag{51}$$

where $\mathbf{I}_\mathrm{s}^\mathrm{inc}(\mu_0, \phi_0)$ is the Stokes vector of the incident beam to the surface, with cosine of zenith angle μ_0 and azimuth angle ϕ_0, $\mathbf{I}_\mathrm{s}(\mu, \phi)$ is the Stokes vector of the reflected beam with geometry specified by μ and ϕ, and $\Delta\phi$ is the relative azimuth angle. The reflection matrix is actually analogous to a scattering matrix in the redistribution of incident radiation fields to all directions in the upwelling hemisphere.

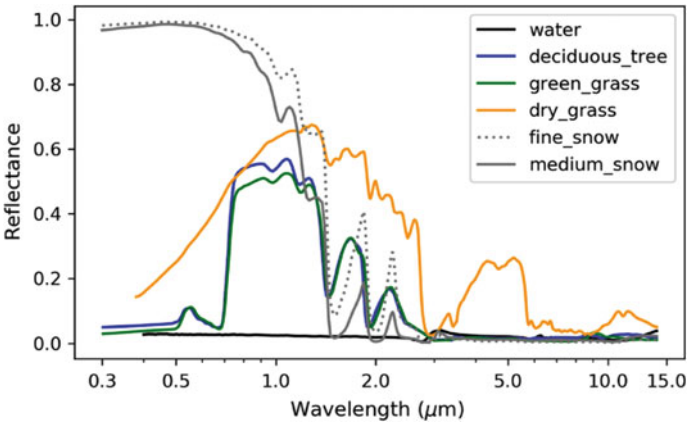

Fig. 6 Reflectance spectra obtained from the ASTER Spectral Library (Baldridge et al. 2009) for various surface types

When the incident radiation is unpolarized, the first three Stokes-vector elements of the reflected beam can be expressed by (Kokhanovsky et al. 2015; Litvinov et al. 2011):

$$I_s = R_{11} I_s^{inc}, \quad Q_s = R_{21} I_s^{inc}, \quad \text{and} \quad U_s = R_{31} I_s^{inc}. \tag{52}$$

Here, the element R_{11} of the matrix $\mathbf{R}$ is the surface total reflectance, which is often referred as bidirectional reflectance distribution function (BRDF). The elements R_{21} and R_{31} describe the surface polarized reflectance, and the surface linearly polarized reflectance is given by

$$R_p = \sqrt{R_{21}^2 + R_{31}^2}. \tag{53}$$

R_p is often called surface bidirectional polarization distribution function (BPDF) (Litvinov et al. 2011). Studies have shown that the BPDF for land surfaces is generally rather small and is "spectrally neutral" (Litvinov et al. 2011; Maignan et al. 2009). Most empirical BPDF models are based on the Fresnel surface reflection (Appendix 2).

For a Lambertian surface, incident light is scattered equally in all directions in the upwelling hemisphere. In this case, the BRDF is isotropic. In UNL-VRTM, we have included a set of reflectance spectra obtained from the ASTER Spectral Library (Baldridge et al. 2009); Fig. 6 shows some of these spectra for typical surface types (water, vegetation, and snow).

VLIDORT (version 2.6) has a supplementary module for the specification of surface BRDF in terms of a linear combination of (up to three) semi-empirical kernel functions (Spurr 2004). A full list of these functions is presented in Appendix 2. The BRDF kernels applicable to vegetation canopy include: the Ross-thin and Ross-thick kernels that are based on *volume scattering* models of light reflectance (Ross 1981); the Li-sparse and Li-dense (1992), and the Roujean et al. (1992) kernels that

are based on *geometric-optical* modeling, and the Rahman (1993) and Hapke (1993) kernels. VLIDORT also incorporated the one-parameter Maignan-2009 BPDF model developed by Maignan et al. (2009), which was derived from analyses of several years of land surface POLDER/PARASOL measurements and can be applicable to land surface. Additionally, VLIDORT has an ocean surface glitter kernel based on the Cox-Munk model (Cox et al. 1954) and a vector glitter kernel based on the description in Mishchenko and Travis (1997).

UNL-VRTM has incorporated all of those BRDF/BPDF kernels. For instance, the commonly used MODIS-type BRDF model is a linear combination of isotropic (Lambertian), Ross-thick K_{vol}, and Li-sparse K_{geo} kernels (Lucht et al. 2000; Wanner et al. 1995),

$$\rho_{\text{R}}(\mu, \mu_0, \Delta\phi) = f_{\text{iso}} + f_{\text{vol}} K_{\text{vol}}(\mu, \mu_0, \Delta\phi) + f_{\text{geo}} K_{\text{geo}}(\mu, \mu_0, \Delta\phi). \tag{54}$$

Expanded expressions for K_{vol} and K_{geo} appear in Wanner et al. (1995) and in Appendix 2 of this chapter. The MODIS BRDF products, reported every 16 days at a 1 km resolution (Lucht et al. 2000), supply the corresponding three coefficients (f_{iso}, f_{vol}, and f_{geo}) in the first 7 MODIS bands.

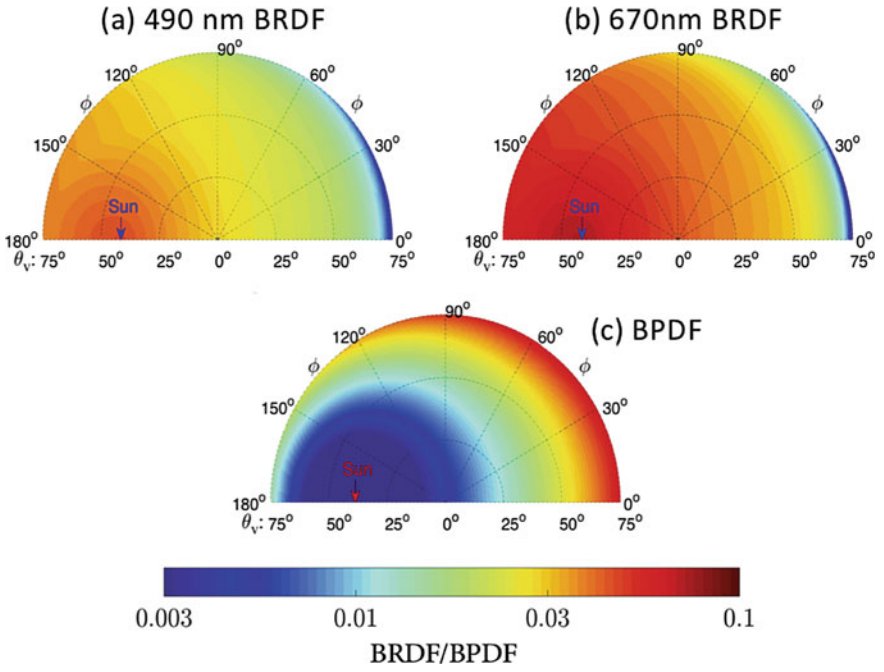

Fig. 7 Polar plots of the angular distribution of a MODIS-type BRDF at 490 nm (**a**) and 670 nm (**b**) and a Maignan-2009 BPDF (**c**) for a vegetated surface. Adapted from Hou et al. (2018)

Figure 7a, b illustrates a simulated MODIS-type BRDF at 490 and 670 nm, and Fig. 7c shows a polar plot for the Maignan-2009 BPDF (assumed to be independent of spectral wavelength). The simulations are for a vegetation surface at a solar zenith angle of 40°. The so-called "hot spot" of BRDF is clearly seen in the backscattering direction of the illuminating source. In contrast, BPDF values are smallest in the backscattering direction and increase with reduced scattering angle.

Finally, the VLIDORT supplementary BRDF module is fully linearized (see Appendix 2). It provides partial derivatives of BRDFs not only with respect to the kernel weighting factors, but also with respect to kernel parameters (such as the wind speed for glitter reflectance). As a result, VLIDORT has the capability to calculate the Jacobians of Stokes parameters with respect to those BRDF and BPDF parameters (Spurr 2004).

2.8 Jacobian Capability

This section describes the methods by which UNL-VRTM calculates Jacobians of $\mathbf{I}$ with respect to various aerosol related parameters (including τ_A, ω_A, $\mathbf{B}_A$, refractive index, PSD parameters, and aerosol vertical profile) and trace gas parameters (τ_G and mixing ratio). This capability is based up on the direct coupling of the linearized radiative transfer model (VLIDORT) with analytical linearization output from other forward modeling components.

2.8.1 Jacobians with Respect to Aerosol Parameters

As discussed in Sect. 2.2.2, computation of the Stokes vector in VLIDORT requires input of optical property sets $[\tau, \omega, \langle \mathbf{B}^j \rangle_{j=0,J}]$ for each atmospheric layer L, as noted in Eqs. (28)–(30). For ease of exposition, we will drop the layer index L in the following.

VLIDORT also generates Jacobians with respect to layer-integrated single scattering properties in each atmospheric layer as well as column-integrated properties, while on the other hand the LMIE and LTMATRIX codes generate weighting functions of aerosol scattering properties with respect to microphysical aerosol physical parameters. Thus an integrated use of VLIDORT and LTMATRIX/LMIE can, in principle, provide the Jacobians of Stokes parameters with respect to both aerosol single scattering properties as well as aerosol microphysical parameters (as expressed by Eqs. (14) and (15)). From a practical standpoint, the VLIDORT calculation of Jacobians of any Stokes parameter ξ with respect to any aerosol parameter x proceeds according to

Table 1 Elements of the transformation vector for various aerosol single scattering parameters

x	ϕ_x	φ_x	$\boldsymbol{\Psi}_x^j$
τ_A	$\frac{\tau_A}{\tau}$	$\frac{\tau_A}{\tau}\left(\frac{\omega_A}{\omega}-1\right)$	$\begin{cases} \frac{\omega_A\tau_A}{\omega\tau}\left(\frac{\mathbf{B}_A^j}{\mathbf{B}^j}-1\right) & \text{for } j<3 \\ \frac{\tau_R}{\omega\tau} & \text{for } j\geq 3 \end{cases}$
ω_A	0	$\frac{\tau_A\omega_A}{\tau_A\omega_A+\tau_R}$	Same as above
$\mathbf{B}_A^l$	0	0	$\begin{cases} \frac{\omega_A\tau_A\mathbf{B}_A^j}{\omega_A\tau_A\mathbf{B}_A^j+\tau_R\mathbf{B}_R^j} & \text{for } l=j<3 \\ 1 & \text{for } l=j\geq 3 \\ 0 & \text{for } l\neq j \end{cases}$

$$
\begin{aligned}
x\frac{\partial\xi}{\partial x} &= x\left[\frac{\partial\xi}{\partial\tau},\frac{\partial\xi}{\partial\omega},\langle\frac{\partial\xi}{\partial\mathbf{B}^j}\rangle_{j=1,J}\right]\left[\frac{\partial\tau}{\partial x},\frac{\partial\omega}{\partial x},\langle\frac{\partial\mathbf{B}^j}{\partial x}\rangle_{j=1,J}\right]^T \\
&= \left[\tau\frac{\partial\xi}{\partial\tau},\omega\frac{\partial\xi}{\partial\omega},\langle\mathbf{B}^j\frac{\partial\xi}{\partial\mathbf{B}^j}\rangle_{j=1,J}\right]\left[\phi_x,\varphi_x,\langle\boldsymbol{\Psi}_x^j\rangle_{j=1,J}\right]^T .
\end{aligned}
\tag{55}
$$

The first square bracket on the right-hand side of Eq. (55) contains quantities computed internally by VLIDORT, while the second "transformation vector" must be supplied by the user and is defined as:

$$
\phi_x = \frac{x}{\tau}\frac{\partial\tau}{\partial x};\quad \varphi_x = \frac{x}{\omega}\frac{\partial\omega}{\partial x};\quad \boldsymbol{\Psi}_x^j = \frac{x}{\mathbf{B}^j}\frac{\partial\mathbf{B}^j}{\partial x}. \tag{56}
$$

As we are interested in aerosol parameters, this transformation vector can be further expanded as

$$
\left[\phi_x,\varphi_x,\langle\boldsymbol{\Psi}_x^j\rangle_{j=1,J}\right]^T = \boldsymbol{\Pi}\left[\phi_x',\varphi_x',\langle\boldsymbol{\Psi}_x'^j\rangle_{j=1,J}\right]^T, \tag{57}
$$

where

$$
\phi_x' = x\frac{\partial\tau_{\mathbf{A}}}{\partial x},\quad \varphi_x' = x\frac{\partial\delta_{\mathbf{A}}}{\partial x},\quad \text{and}\quad \boldsymbol{\Psi}_x'^j = x\frac{\partial\mathbf{B}_{\mathbf{A}}^j}{\partial x}, \tag{58}
$$

and $\boldsymbol{\Pi}$ is a transformation matrix expressed by

$$
\boldsymbol{\Pi} = \begin{bmatrix} \frac{1}{\tau} & \mathbf{0} & \mathbf{0} \\ -\frac{1}{\tau} & \frac{1}{\delta_A+\tau_R} & \mathbf{0} \\ \mathbf{0} & \langle\frac{\mathbf{B}_A^j-\mathbf{B}_R^j}{\mathbf{B}^j(\delta_A+\tau_R)}\rangle_{j=1,J} & \langle\frac{\delta_A}{\mathbf{B}^j(\delta_A+\tau_R)}\rangle_{j=1,J} \end{bmatrix}. \tag{59}
$$

Here, δ_A is the scattering optical depth of aerosols. A detailed derivation of the matrix $\boldsymbol{\Pi}$ is found in Appendix 3. Hence, the transformation vector for calculating Stokes profile Jacobians with respect to τ_A, ω_A, $\mathbf{B}_A^l$ can be obtained by combining Eqs. (57) and (59), and the components of this vector are listed in Table 1.

In an atmosphere where both fine (denoted by superscript 'f') and coarse (denoted superscript 'c') aerosol particles co-exist, the bulk aerosol optical properties may be derived by assuming external mixing regime:

$$\begin{cases} \tau_{\mathrm{A}} &= \tau_{\mathrm{A}}^{\mathrm{f}} + \tau_{\mathrm{A}}^{\mathrm{c}} \\ \delta_{\mathrm{A}} &= \delta_{\mathrm{A}}^{\mathrm{f}} + \delta_{\mathrm{A}}^{\mathrm{c}} \\ \mathbf{B}_{\mathrm{A}}^{j} &= \frac{\delta_{\mathrm{A}}^{\mathrm{f}} + \delta_{\mathrm{A}}^{\mathrm{c}}}{\delta_{\mathrm{A}}^{\mathrm{f}} \mathbf{B}_{\mathrm{A}}^{\mathrm{f},j} + \delta_{\mathrm{A}}^{\mathrm{c}} \mathbf{B}_{\mathrm{A}}^{\mathrm{c},j}} \end{cases} \tag{60}$$

We can generate the transformation vectors (as listed in Table 2) for any of the following parameters: $\tau_{\mathrm{A}}^{\mathrm{f}}, \omega_{\mathrm{A}}^{\mathrm{f}}, V_0^{\mathrm{f}}, m_{\mathrm{r}}^{\mathrm{f}}, m_{\mathrm{i}}^{\mathrm{f}}, r_{\mathrm{g}}^{\mathrm{f}}, \sigma_{\mathrm{g}}^{\mathrm{f}}, \varepsilon^{\mathrm{f}}, H^{\mathrm{f}}$, and $\tau_{\mathrm{A}}^{\mathrm{c}}, \omega_{\mathrm{A}}^{\mathrm{c}}, V_0^{\mathrm{c}}, m_{\mathrm{r}}^{\mathrm{c}}, m_{\mathrm{i}}^{\mathrm{c}}, r_{\mathrm{g}}^{\mathrm{c}}, \sigma_{\mathrm{g}}^{\mathrm{c}}$, ε^{c}, and H^{c}. Here, $r_{\mathrm{g}}, \sigma_{\mathrm{g}}$, and H denote the median and standard deviation of the PSD (e.g., two parameters in the lognormal aerosol number distribution), and the scale height of aerosol extinction, respectively. V_0 is the aerosol volume concentration and ε the shape factor of the non-spherical particle. Details of the algebra for deriving the transformation vectors may be found in Appendix 3.

Analytical formulas for ϕ'_x, φ'_x, and $\boldsymbol{\Psi}'^{j}_{x}$ for coarse mode aerosol parameters are the same as their counterparts for fine-mode aerosols; we need only replace superscript 'f' with 'c' in the Table 2 entries. Jacobians with respect to the fine mode fraction, either in terms of AOD (fmf_τ) or in terms of the volume concentration ($\mathrm{fmf}_{\mathrm{v}}$), can be derived from the corresponding Jacobians with respect to modal AOD and volume, respectively:

$$\mathrm{fmf}_\tau \frac{\partial \xi}{\partial \mathrm{fmf}_\tau} = \tau_{\mathrm{A}}^{\mathrm{f}} \frac{\partial \xi}{\partial \tau_{\mathrm{A}}^{\mathrm{f}}} - \frac{\mathrm{fmf}_\tau}{1 - \mathrm{fmf}_\tau} \tau_{\mathrm{A}}^{\mathrm{c}} \frac{\partial \xi}{\partial \tau_{\mathrm{A}}^{\mathrm{c}}} \tag{61}$$

$$\mathrm{fmf}_{\mathrm{v}} \frac{\partial \xi}{\partial \mathrm{fmf}_{\mathrm{v}}} = V_0^{\mathrm{f}} \frac{\partial \xi}{\partial {V_0}^{\mathrm{f}}} - \frac{\mathrm{fmf}_{\mathrm{v}}}{1 - \mathrm{fmf}_{\mathrm{v}}} V_0^{\mathrm{c}} \frac{\partial \xi}{\partial {V_0}^{\mathrm{c}}} \tag{62}$$

Detailed derivations of these VLIDORT inputs may be found in Appendix 3, and a comprehensive validation of these Jacobian calculations is given in Sect. 2.9.[1]

2.8.2 Jacobians with Respect to Trace Gases

With some derivations using Eqs. (28)–(30), inputs [denoted in Eq. (56)] to VLIDORT for calculating the Jacobian of $\mathbf{I}$ with respect to τ_{G} at any atmospheric layer are given by

$$\phi_x = \frac{\tau_{\mathrm{G}}}{\tau}; \quad \varphi_x = -\frac{\tau_{\mathrm{G}}}{\tau}; \quad \boldsymbol{\Psi}^{j}_{x} = 0 \quad \text{for} \quad j = 0 \ldots J. \tag{63}$$

Here, τ_{G} is total absorption optical depth of all trace gases in an atmospheric layer as calculated in Eq. (33).

[1] Expressions are shown only for fine-mode parameters; expressions for coarse-mode parameters are the same but with superscripts replaced by 'c'.

Table 2 Elements of the transformation vector for various microphysical parameters of fine and coarse mode aerosols

x	$\phi'_{x^{\mathrm{f}}}$	$\varphi'_{x^{\mathrm{f}}}$	$\boldsymbol{\Psi}'^{j}_{x^{\mathrm{f}}}$
$\tau_{\mathrm{A}}^{\mathrm{f}}$	$\tau_{\mathrm{A}}^{\mathrm{f}}$	$\delta_{\mathrm{A}}^{\mathrm{f}}$	$\frac{\delta_{\mathrm{A}}^{\mathrm{f}}}{\tau_{\mathrm{A}}}(\mathbf{B}_{\mathrm{A}}^{\mathrm{f}j} - \mathbf{B}_{\mathrm{A}}^{j})$
ω_{A}	0	$\delta_{\mathrm{A}}^{\mathrm{f}}$	$\frac{\delta_{\mathrm{A}}^{\mathrm{f}}}{\tau_{\mathrm{A}}}(\mathbf{B}_{\mathrm{A}}^{\mathrm{f}j} - \mathbf{B}_{\mathrm{A}}^{j})$
V_0^{f}	$\frac{3V_0^{\mathrm{f}}Q_{\mathrm{ext}}^{\mathrm{f}}}{4r_{\mathrm{eff}}^{\mathrm{f}}}$	$\frac{3V_0^{\mathrm{f}}Q_{\mathrm{sca}}^{\mathrm{f}}}{4r_{\mathrm{eff}}^{\mathrm{f}}}$	$\frac{\delta_{\mathrm{A}}^{\mathrm{f}}}{\tau_{\mathrm{A}}}(\mathbf{B}_{\mathrm{A}}^{\mathrm{f}j} - \mathbf{B}_{\mathrm{A}}^{j})$
$m_{\mathrm{r}}^{\mathrm{f}}, m_{\mathrm{i}}^{\mathrm{f}}$	$\tau_{\mathrm{A}}^{\mathrm{f}}\frac{x^{\mathrm{f}}}{Q_{\mathrm{ext}}^{\mathrm{f}}}\frac{\partial Q_{\mathrm{ext}}^{\mathrm{f}}}{\partial x^{\mathrm{f}}}$	$\delta_{\mathrm{A}}^{\mathrm{f}}\frac{x^{\mathrm{f}}}{Q_{\mathrm{sca}}^{\mathrm{f}}}\frac{\partial Q_{\mathrm{sca}}^{\mathrm{f}}}{\partial x^{\mathrm{f}}}$	$\frac{\varphi'_{x^{\mathrm{f}}}}{\delta_{\mathrm{A}}^{\mathrm{f}}}(\mathbf{B}_{\mathrm{A}}^{\mathrm{f}j} - \mathbf{B}_{\mathrm{A}}^{j}) + x^{\mathrm{f}}\frac{\partial \mathbf{B}_{\mathrm{A}}^{\mathrm{f}j}}{\partial x^{\mathrm{f}}}$
$r_{\mathrm{g}}^{\mathrm{f}}, \sigma_{\mathrm{g}}^{\mathrm{f}}, \varepsilon^{\mathrm{f}}$	$\tau_{\mathrm{A}}^{\mathrm{f}}\left(\frac{x^{\mathrm{f}}}{Q_{\mathrm{ext}}^{\mathrm{f}}}\frac{\partial Q_{\mathrm{ext}}^{\mathrm{f}}}{\partial x^{\mathrm{f}}} - \frac{x^{\mathrm{f}}}{r_{\mathrm{eff}}^{\mathrm{f}}}\frac{\partial r_{\mathrm{eff}}^{\mathrm{f}}}{\partial x^{\mathrm{f}}}\right)$	$\delta_{\mathrm{A}}^{\mathrm{f}}\left(\frac{x^{\mathrm{f}}}{Q_{\mathrm{sca}}^{\mathrm{f}}}\frac{\partial Q_{\mathrm{sca}}^{\mathrm{f}}}{\partial x^{\mathrm{f}}} - \frac{x^{\mathrm{f}}}{r_{\mathrm{eff}}^{\mathrm{f}}}\frac{\partial r_{\mathrm{eff}}^{\mathrm{f}}}{\partial x^{\mathrm{f}}}\right)$	$\frac{\varphi'_{x^{\mathrm{f}}}}{\delta_{\mathrm{A}}^{\mathrm{f}}}(\mathbf{B}_{\mathrm{A}}^{\mathrm{f}j} - \mathbf{B}_{\mathrm{A}}^{j}) + x^{\mathrm{f}}\frac{\partial \mathbf{B}_{\mathrm{A}}^{\mathrm{f}j}}{\partial x^{\mathrm{f}}}$
H^{f}	$H^{\mathrm{f}}\frac{\partial \tau_{\mathbf{A}}}{\partial H^{\mathrm{f}}}$	$\phi'_{x^{\mathrm{f}}}\omega_{\mathrm{A}}^{\mathrm{f}}$	$\frac{\delta_{\mathrm{A}}^{\mathrm{f}}}{\tau_{\mathrm{A}}}(\mathbf{B}_{\mathrm{A}}^{\mathrm{f}j} - \mathbf{B}_{\mathrm{A}}^{j})$

To obtain the Jacobian with respect to mixing ratio q_i of a gas i. q_i in units of ppm, we use the definition $q_i = 10^6 N_{\mathrm{gas},i}/N_{\mathrm{air}}$, where $N_{\mathrm{gas},i}$ and N_{air} are the averaged density of that gas and air molecules in the atmospheric layer, respectively. Then Eq. (33) becomes

$$\tau_{\mathrm{G}} = 10^{-6} N_{\mathrm{air}} \Delta H \sum_{i=1}^{K} q_i \sigma_{\mathrm{G},i}(T, P). \tag{64}$$

One can derive the Jacobian with respect to q_i as follows:

$$q_i \frac{\partial \mathbf{I}}{\partial q_i} = \frac{\tau_{\mathrm{G},i}}{\tau_{\mathrm{G}}}\left(\tau_{\mathrm{G}}\frac{\partial \mathbf{I}}{\partial \tau_{\mathrm{G}}}\right). \tag{65}$$

2.9 Model Benchmarking and Verification

Figure 8a shows the downward solar spectral irradiance at the top-of-atmosphere and at the surface for a solar zenith angle of 30°. Spectral regions dominated by gas absorption can be clearly identified, including the O_3 Hartley-Huggins bands in the UV, the O_2 B band (0.69 μm) and O_2 A band (0.76 μm), as well as a number of water vapor bands. Calculations shown in Fig. 8 were performed at a spectral resolution of 0.01 nm. In general, this resolution is high enough to resolve fine structure in gas absorptions. In the UV below 300 nm, and in parts of the O_2 A and O_2 B bands, whole-atmosphere gas absorption optical depths can reach 50 or more, and the downward irradiance is virtually zero at the ground (Fig. 8b). The inset in Fig. 8b shows a close-up view of the fine structure in absorption optical depth for the O_2 A band, with dual peaks centered at 0.761 μm (R branch) and 0.764 μm (P branch), and a deep, narrow valley around 0.762 μm (Q branch).

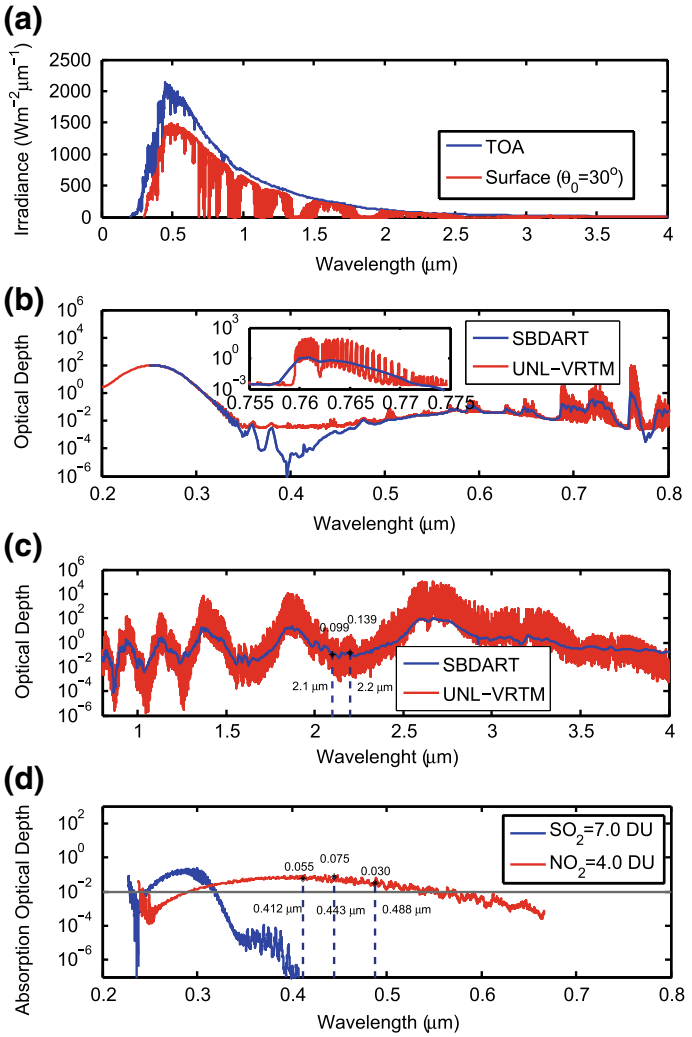

Fig. 8 Some benchmark simulations by the UNL-VRTM: **a** Downward solar spectral irradiance at the TOA and the surface for solar zenith angle 30°. **b** Total-atmosphere gas absorption optical depth in the range 0.2–0.8 μm. **c** Same as **b** but for 0.8–4 μm. **d** Optical depth of SO_2 and NO_2 in polluted cases. Also shown in **b** and **c** are optical depths computed with the Santa Barbara DISORT Atmospheric Radiative Transfer (SBDART) model (Ricchiazzi et al. 1998). The mid-latitude summer atmospheric profile is assumed. Figure adapted from Wang et al. (2014)

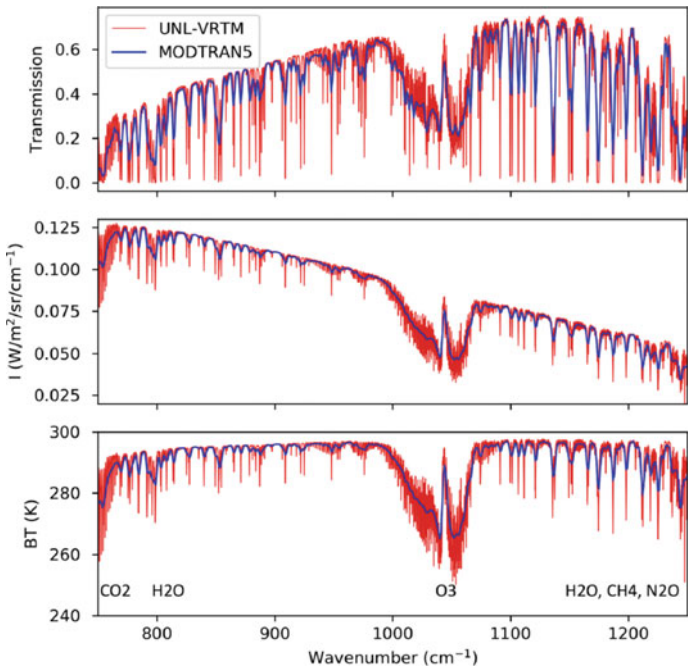

Fig. 9 UNL-VRTM benchmark simulations (red) in a typical IR 'atmosphere window', compared with those from MODTRAN5 (blue). The three panels show the transmission (top), TOA radiance (I, middle), and brightness temperature (BT, bottom), respectively. The used spectral resolution (FWHM) and sampling interval are 0.4 and 0.1 cm^{-1} for UNL-VRTM and 2 and 1 cm^{-1} for MODTRAN5, respectively. The view zenith angle is 0°. Simulations are based on the "Tropical" standard atmosphere with a surface temperature of 299.7 K. Gases are labeled according to their major absorption signatures

Also of note is significant absorption of SO_2 and NO_2 in UV and blue wavelength regions respectively (Fig. 8d). In urban regions, high SO_2 and NO_2 can together contribute optical depths of around 0.03–0.07 (Fig. 8d). Hence, in order to take advantage of low surface reflectance in the UV and the use of deep-blue wavelengths for the retrieval of AOD in urban regions, it is critical to treat absorption by SO_2 and NO_2. In contrast, calculations performed at moderate spectral resolution (such as those from SBDART (Ricchiazzi et al. 1998), shown as the blue lines in Fig. 8b, c) do not resolve fine-structure details, for example sometimes missing the absorption lines for SO_2 or NO_2, and in general producing significant underestimation of optical depths in the O_2A band.

Figure 9 shows UNL-VRTM and MODTRAN5 simulations of transmission (top), TOA radiance (I, middle), and brightness temperature (BT, bottom) as seen from space in the IR 'atmospheric window' from 750 to 1250 cm^{-1}. MODTRAN5 (MODerate resolution atmospheric TRANsmission) is a radiative transfer model developed and maintained by Spectral Sciences Inc. and the Air Force Research Laboratory

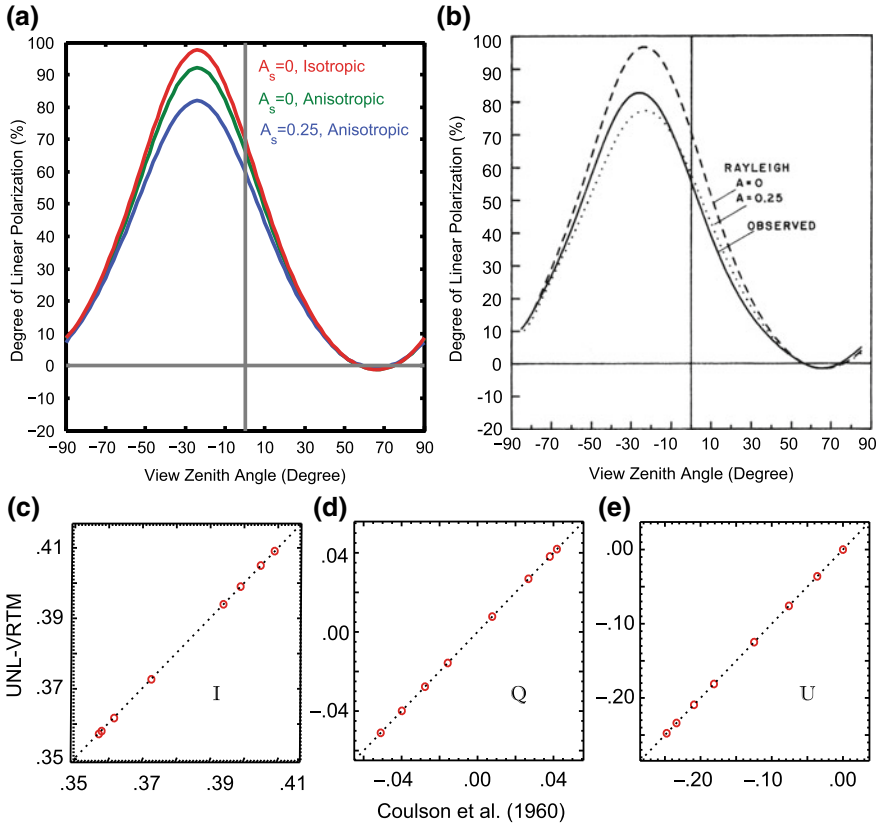

Fig. 10 Validating UNL-VRTM for calculating the degree of linear polarization $(-Q/I)$ of downward radiation for a pure Rayleigh atmosphere: **a** computed by UNL-VRTM for the case analyzed in Fig. 5.7 of Coulson et al. (1988), which is replicated here in panel (**b**). **c**–**e** shows the comparisons of I, Q, and U computed by Coulson et al. (1960) and those from UNL-VRTM. In **a** and **b**, A_s represents the surface albedo value. In **c**–**e**, the calculation is for $\tau = 1.0$, surface albedo is 0.25, $\cos\theta_0 = 0.8$, and for 8 different viewing angles. Figure adapted from Wang et al. (2014)

(Berk et al. 2004). The spectral resolution (FWHM) and sampling interval are 0.4 and 0.1 cm^{-1} for UNL-VRTM and 2 and 1 cm^{-1} for MODTRAN5, respectively. The view zenith angle is 0°. Simulations for the Tropical standard atmosphere with a surface temperature of 299.7 K take into account line absorption of H_2O, CO_2, O_3, CH_4, and N_2O, and continuum absorption of H_2O and CO_2. Clearly, UNL-VRTM and MODTRAN5 agree closely with each other in both the simulated transmission and radiance (or BT). The main difference is that the MODTRAN5 simulation uses a coarser spectral resolution then results in much smoother spectra.

Figure 10 shows the calculation for DOLP of downward radiation in a pure Rayleigh scattering atmosphere. The solid blue line in Fig. 10a (dotted line in Fig. 10b) reproduces the theoretical results shown in Fig. 5.7 of (Coulson et al. 1988).

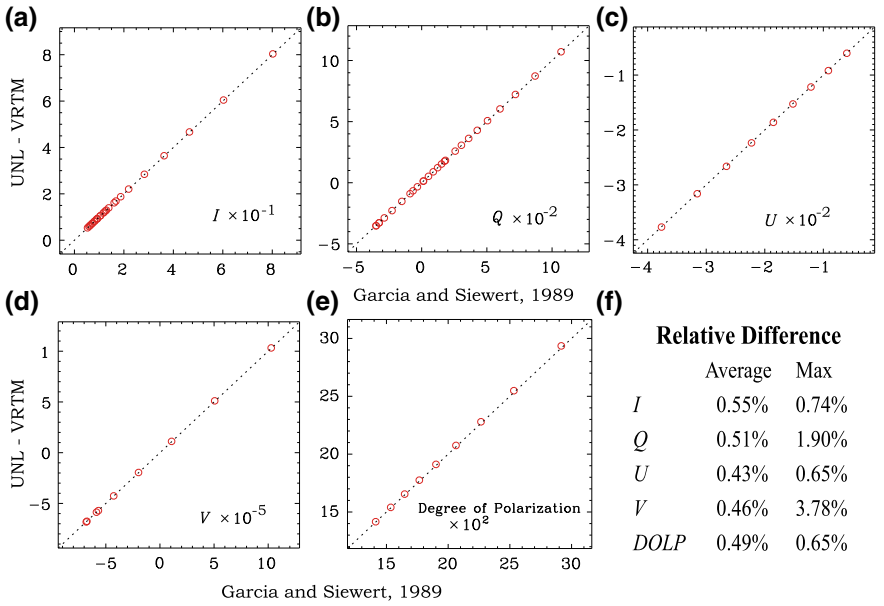

Fig. 11 Validation of UNL-VRTM for calculating DOLP $(-Q/I)$ of upwelling radiation for a Mie scattering atmosphere, against the benchmarked data in Tables 3–10 of Garcia and Siewert (1989) for the same atmospheric conditions of aerosol scattering. Gas absorption and Rayleigh scattering are excluded. Shown here are I and Q values reported in Garcia and Siewert (1989) for 9 view angles (with cosine values from 0.1 to 0.9 at equal spacing of 0.1) and 3 relative azimuth angles (0, $\pi/2$, and π), a total of 27 data points. For U and V, values are reported for the same 9 viewing angles but for one relative azimuth angle ($\pi/2$) only. The calculation is performed at 951 nm and column τ of 1.0, with lognormal aerosol size distribution parameters $r_{\text{eff}} = 0.2$, $v_{\text{eff}} = 0.07$, refractive index $m_{\text{r}} = 1.44$, and single scattering albedo 0.99. Figure adapted from Wang et al. (2014)

The plot was used to interpret the DOLP measured at Mauna Loa Observatory on February 19, 1977. Furthermore, Fig. 10a shows that the anisotropy in Rayleigh scattering reduces the peak DOLP by 5% (e.g., the difference between the green and red lines) at 0.7 μm. Surface reflection and its concomitant increase of atmosphere scattering will decrease the DOLP of downward radiation. An increase of surface reflectance from 0 to 0.25 decreases the peak DOLP by about 10%.

We also conducted a quantitative validation for a Rayleigh scattering scenario by following a VLIDORT validation (Natraj and Hovenier 2012). As seen in Fig. 10c–e, I, Q, and U components computed with UNL-VRTM differ from their counterparts found in the tables by Coulson et al. (1960) by average (relative) deviations of 1.9×10^{-4} (0.05%), 2×10^{-5} (0.14%), and 4×10^{-5} (0.03%), respectively. These differences are similar to the values 2.1×10^{-4}, 9×10^{-5}, and 7×10^{-5} identified by Evans and Stephens (1991).

Figure 11 shows benchmark calculations of four Stokes parameters for radiative transfer in an aerosol-only medium. Garcia and Siewert (1989) documented their

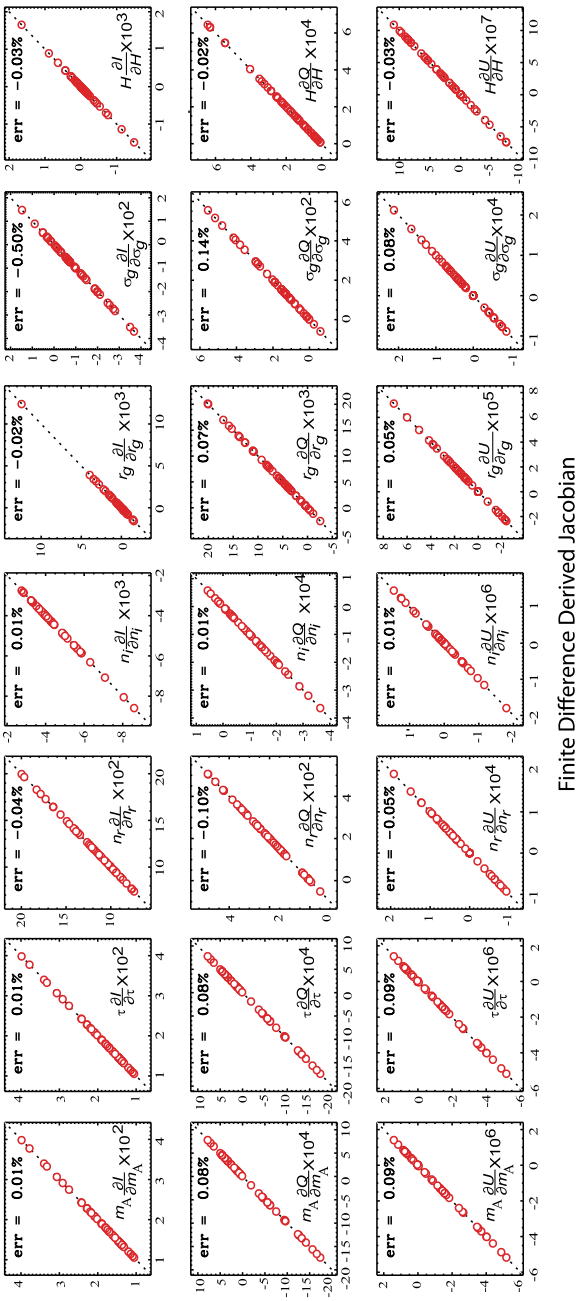

Fig. 12 Validation of UNL-VRTM's fine-mode Jacobians ($\partial\xi/\partial \ln x$) (y-axis) with those computed from UNL-VRTM using finite-difference estimates (x-axis). Here ξ is one of the Stokes parameters: I (top row), Q (middle row), and U (bottom row). x is one of 7 parameters associated with fine-mode aerosols: mass concentration m_A, τ_A, m_r, m_i, r_g and σ_g (of the lognormal PSD), and height (H) of peak aerosol concentration in the vertical. Note, the calculation is done for an atmosphere containing both fine- and coarse-mode aerosols as described in Hess et al. (1998). Jacobians with respect to coarse-mode aerosol parameters show similar validation accuracy (not shown here). Figure adapted from Wang et al. (2014)

results for unpolarized incident radiation at 951 nm and $\cos\theta_0$ of 0.2, a Lambertian reflectance 0.1, with aerosols having a gamma-function PSD with r_{eff} 0.2 μm and v_{eff} 0.07, and a refractive index yielding an aerosol single scattering albedo of 0.99. Compared to the results in Garcia and Siewert (1989), the Stokes parameters computed by UNL-VRTM show relative differences of less than 0.6%, with maximum relative differences (at certain viewing geometries) of up to 2% for Q and 3.8% for V. The DOLP computed from the UNL-VRTM (with 15 streams for the hemisphere) and documented by Garcia and Siewert (1989) (with 3 streams) differ on average by 0.5%, with a maximum relative difference of 0.65%. The results are consistent with the VLIDORT validation that used the same aerosol case (Spurr 2008; Spurr and Christi 2019).

The simultaneous calculation of analytic Jacobians of the four Stokes parameters with respect to the aerosol optical depth, size parameters, refractive indices, and aerosol-loading peak height for both fine and coarse model aerosols may be validated against Jacobians estimates obtained by the finite difference method. As seen in Fig. 12, results from the two methods are highly correlated as seen in the scatter plots shown in these figures. Relative differences in all comparisons are less than 0.5%, and in many cases the differences are less than 0.05%.

3 Optimized Inversion and Information Content Analysis

Inverse algorithms and forward modeling are the two major components for the retrieval of aerosol parameters from remote sensing observations. UNL-VRTM aims to provide a testbed will not only simulate remote sensing observations, but will also provide the kind of quantitative information contained in the observations that is useful for retrieving these aerosol parameters. In this regard, we have implemented a Bayesian-based optimal estimation (OE) algorithm to characterize and retrieve the maximal information content contained in any combination of measurements. With this, the testbed will allow us to seek the best design of a observing system that optimally balances the science value and cost.

In this section, we summarize inverse retrieval theory, looking in particular at the Bayesian-based OE method and information content analysis. Then we discuss the deployment of the OE algorithm in UNL-VRTM, in particular focusing on coupling the inverse code with the forward model component.

3.1 Maximum a Posteriori (MAP) Solution of an Inverse Problem

Let $\mathbf{x}$ denote a state vector that contains n parameters to be retrieved (e.g. PSD parameters and complex indices of refraction), and $\mathbf{y}$ an observation vector with m

elements (such as multi-band radiances from different viewing angles). Furthermore, let $\mathbf{F}$ indicate a forward-model operator (containing the UNL-VRTM forward model components) that describes the physics of how $\mathbf{y}$ and $\mathbf{x}$ are related. Then, we may write

$$\mathbf{y} = \mathbf{F}(\mathbf{x}, \mathbf{b}) + \boldsymbol{\varepsilon}_{\mathrm{y}} \tag{66}$$

where the vector $\mathbf{b}$ consists of forward model parameters (such as the surface reflectance) that are not included in $\mathbf{x}$ but will quantitatively influence retrieval accuracy, and $\boldsymbol{\varepsilon}_{\mathrm{y}}$ term is the measurement error. In this study, we use the best-estimate $\hat{\mathbf{b}}$ in the forward model and consider its contributions to the overall retrieval accuracy. Linearizing the forward model at $\mathbf{b} = \hat{\mathbf{b}}$:

$$\mathbf{y} = \mathbf{F}(\mathbf{x}, \hat{\mathbf{b}}) + \hat{\mathbf{K}}_{\mathrm{b}}(\mathbf{b} - \hat{\mathbf{b}}) + \boldsymbol{\varepsilon}_{\mathrm{y}} \tag{67}$$

where $\hat{\mathbf{K}}_{\mathrm{b}}$ is the weighting function (or Jacobian matrix) of the forward model to model parameters $\mathbf{b}$ at $\hat{\mathbf{b}}$, $\frac{\partial \mathbf{F}}{\partial \mathbf{b}}\big|_{\mathbf{b}=\hat{\mathbf{b}}}$. If we treat the forward model as linear in the vicinity of the true state of $\mathbf{x}$, the forward model can be rewritten as:

$$\mathbf{y} = \mathbf{K}\mathbf{x} + \boldsymbol{\varepsilon}. \tag{68}$$

Here, $\boldsymbol{\varepsilon}$ represents the the sum of errors from the forward modeling step and the measurements. We only consider uncertainties in $\mathbf{b}$, but omitting other sources of error in the forward modeling. Thus, $\boldsymbol{\varepsilon} = \boldsymbol{\varepsilon}_{\mathrm{y}} + \hat{\mathbf{K}}_{\mathrm{b}}\boldsymbol{\varepsilon}_{\mathrm{b}}$, where $\boldsymbol{\varepsilon}_{\mathrm{b}} = \mathbf{b} - \hat{\mathbf{b}}$ denotes the error of $\hat{\mathbf{b}}$. $\mathbf{K}$ is the $m \times n$ Jacobian matrix comprising derivatives of the forward model with respect to each retrieved parameter, $\frac{\partial \mathbf{F}}{\partial \mathbf{x}}$.

The inverse problem derives $\mathbf{x}$ from the measurement $\mathbf{y}$ by inverting the forward model $\mathbf{F}$. In most situations, the forward model is a complex process with a large number of internal uncertainties. As a result, the inverse problem tends to be an ill-posed problem, which requires imposition of a priori constraints. A priori represents the knowledge of the state before the measurements are made. Further, we assume that the true state is "close" to the a priori:

$$\mathbf{x} = \mathbf{x}_{\mathrm{a}} + \boldsymbol{\varepsilon}_{\mathrm{a}}. \tag{69}$$

where $\mathbf{x}_{\mathrm{a}}$ is the *a priori estimate* and $\boldsymbol{\varepsilon}_{\mathrm{a}}$ indicates the a priori error.

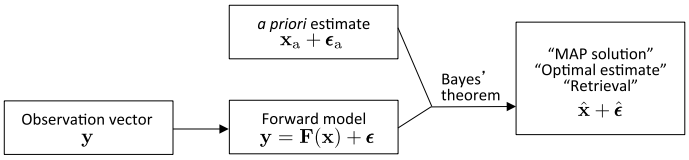

Fig. 13 The concept of an inverse problem that optimzes an estimate from observations. (Courtesy: Daniel Jacobs)

Then, the inverse problem solves the equation set (as illustrated in Fig. 13):

$$\begin{cases} \mathbf{y} = \mathbf{K}\mathbf{x} + \boldsymbol{\varepsilon} \\ \mathbf{x} = \mathbf{x}_\mathrm{a} + \boldsymbol{\varepsilon}_\mathrm{a}. \end{cases} \tag{70}$$

As long as measurement and a priori errors are characterized by a Gaussian probability distribution functions (PDFs), and the forward model is assumed linear in the vicinity of the true state, then the maximum *a posteriori* (MAP) solution of the state vector, also called the retrieval or the *a posteriori* derived with the Bayes' Theorem, is given by Rodgers (2000):

$$\hat{\mathbf{x}} = \mathbf{x}_\mathrm{a} + (\mathbf{K}^T \mathbf{S}_\varepsilon^{-1} \mathbf{K} + \mathbf{S}_\mathrm{a}^{-1})^{-1} \mathbf{K}^T \mathbf{S}_\varepsilon^{-1} (\mathbf{y} - \mathbf{K}\mathbf{x}_\mathrm{a}) \tag{71}$$

Here, $\mathbf{S}_\mathrm{a}$ is the error covariance matrix of the a priori $\mathbf{x}_\mathrm{a}$; $\mathbf{S}_\varepsilon$ is the error covariance matrix of the measurements; T denotes the matrix transpose operation.

The retrieved state vector $\hat{\mathbf{x}}$ in Eq. (71) corresponds to the maximum posterior PDF and the minimum of a cost function defined by

$$J = (\mathbf{y} - \mathbf{K}\mathbf{x})^T \mathbf{S}_\varepsilon^{-1} (\mathbf{y} - \mathbf{K}\mathbf{x}) + (\mathbf{x} - \mathbf{x}_\mathrm{a})^T \mathbf{S}_\mathrm{a}^{-1} (\mathbf{x} - \mathbf{x}_\mathrm{a}). \tag{72}$$

The posterior PDF is also Gaussion, with expected value of $\hat{\mathbf{x}}$ and error covariance matrix $\hat{\mathbf{S}}$ given by

$$\hat{\mathbf{S}}^{-1} = \mathbf{K}^T \mathbf{S}_\varepsilon^{-1} \mathbf{K} + \mathbf{S}_\mathrm{a}^{-1}. \tag{73}$$

$\hat{\mathbf{S}}$ describes the statistical uncertainties in the retrieved state vector $\hat{\mathbf{x}}$ due to measurement noise, forward model parameter uncertainty, and smoothing error. The square roots of its diagonal entries are the one-sigma uncertainties of each retrieved element of $\hat{\mathbf{x}}$. Using $\hat{\mathbf{S}}$, we can also estimate errors for additional parameters that can be fully expressed in terms of the state vector elements (for example, the error in the aerosol single scattering albedo can be estimated from aerosol refractive index and PSD parameters). If such a parameter is a function of $\hat{\mathbf{x}}$ defined by $\zeta = \zeta(\mathbf{x})$, then the uncertainty in derived ζ is:

$$\hat{\varepsilon}_\zeta = \sqrt{\sum_{i=1}^{n} \sum_{i=1}^{n} \frac{\partial \zeta}{\partial x_i} \frac{\partial \zeta}{\partial x_j} \hat{\mathbf{S}}_{i,j}}. \tag{74}$$

3.2 Information Theory

The Jacobian matrix $\mathbf{K}$ is an important source of information in the sensitivity analysis. For a linear system in the absence of measurement error, the rank of $\mathbf{K}$ is a measure of the number of independent pieces of information that can be determined

from the measurements. In practice, measurement (and other) errors will inevitably impact the effective rank. To identify the effective sensitivity of individual measurement to each retrieved parameter, we define the error-normalized (EN) Jacobian matrix by

$$\tilde{\mathbf{K}} = \mathbf{S}_{\varepsilon}^{-\frac{1}{2}} \mathbf{K} \mathbf{S}_{\mathrm{a}}^{\frac{1}{2}}. \tag{75}$$

$\tilde{\mathbf{K}}$ is also called the "pre-whitening" matrix by Rodgers (2000). The advantage of matrix $\tilde{\mathbf{K}}$ over the matrix $\mathbf{K}$ is that the former compares the observation error covariance ($\mathbf{S}_{\varepsilon}^{\frac{1}{2}}$) with the natural variability of the observation vector as expressed by its prior covariance ($\mathbf{K}\mathbf{S}_{\mathrm{a}}^{\frac{1}{2}}$). Any component whose natural variability is smaller than the observation error is not measurable. Therefore, an element in $\tilde{\mathbf{K}}_{i,j}$ that is less than unity indicates that the measurement component y_i does not contain useful information contributing to the determination of parameter x_j. In contrast, when $\tilde{\mathbf{K}}_{i,j} > 1$, and the larger the value of this quantity, then the more useful information is retained in y_i for the determination of x_j. Therefore, the $\tilde{\mathbf{K}}$ matrix not only provides the sensitivity of individual measurements to each retrieved parameter, but it is also a information-capacity metric for those observations to infer retrieved parameters.

The averaging kernel matrix is a widely-used metric to quantify retrieval information. It provides the sensitivity of the retrieval to the true state and is defined by

$$\mathbf{A} = \frac{\partial \hat{\mathbf{x}}}{\partial \mathbf{x}}. \tag{76}$$

Replacing y in Eq. (71) with Eq. (68) at $\mathbf{x} = \mathbf{x}_{\mathrm{a}}$,

$$\hat{\mathbf{x}} = \mathbf{x}_{\mathrm{a}} + (\mathbf{K}^T \mathbf{S}_{\varepsilon}^{-1} \mathbf{K} + \mathbf{S}_{\mathrm{a}}^{-1})^{-1} \mathbf{K}^T \mathbf{S}_{\varepsilon}^{-1} [\mathbf{K}(\mathbf{x} - \mathbf{x}_{\mathrm{a}}) + \boldsymbol{\varepsilon}] \tag{77}$$

Then we have

$$\mathbf{A} = \frac{\partial \hat{\mathbf{x}}}{\partial \mathbf{x}} = \left(\mathbf{K}^T \mathbf{S}_{\varepsilon}^{-1} \mathbf{K} + \mathbf{S}_{\mathrm{a}}^{-1}\right)^{-1} \mathbf{K}^T \mathbf{S}_{\varepsilon}^{-1} \mathbf{K} \tag{78}$$

Matrix $\mathbf{A}$ quantifies the ability of the retrieval to infer $\hat{\mathbf{x}}$ given the relationship between $\mathbf{y}$ and $\mathbf{x}$ (i.e., $\mathbf{K}$) and given the observation noise and *a priori* characterization. Thus, $\mathbf{A}$ represents a perfect retrieval if it is an identity matrix; if $\mathbf{A}$ is the null matrix, no information at all can be gained from the observations. The trace of $\mathbf{A}$ is the degree of freedom for signal (DFS)

$$\mathrm{DFS} = \mathrm{Trace}(\mathbf{A}), \tag{79}$$

which is a measure of the number of independent pieces of information that the observations can provide. The diagonal elements of the averaging kernel matrix $\mathbf{A}$, or the DFS components, are the partial sensitivities of individual retrieval parameters with respect to their corresponding truth values:

$$\mathbf{A}_{i,i} = \frac{\partial \hat{x}_i}{\partial x_i} \tag{80}$$

Clearly, $\mathbf{A}_{i,i} = 1$ indicates that the observations are fully capable of characterizing the truth of x_i; while $\mathbf{A}_{i,i} = 0$ indicates the observations contain no information about x_i and x_i is not measurable.

From the formulation of $\hat{\mathbf{S}}$ and $\mathbf{A}$, we conclude that only the error covariance and Jacobian matrix are important for the understanding and quantification of information content. In other words, the resulting DFS and retrieval error essentially depend on error specifications for a priori state and for the observations. Realistic uncertainty characterizations for these two quantities are thus of critical importance in retrieval studies.

Other quantities used for information analysis include the Shannon information content H_{shannon} (Shannon 1948) and the Fisher information matrix. H_{shannon} is defined as the reduction in entropy after applying the measurements

$$H_{\text{shannon}} = \frac{1}{2}\ln|\mathbf{S}_{\text{a}}| - \frac{1}{2}\ln|\hat{\mathbf{S}}| = -\frac{1}{2}\ln|\hat{\mathbf{S}}\mathbf{S}_{\text{a}}^{-1}| = -\frac{1}{2}\ln|\mathbf{I}_n - \mathbf{A}| \tag{81}$$

where $\mathbf{I}_n$ is an identity matrix of order n. Clearly, H_{shannon} is closely related to the DFS. In the Gaussian linear case, the Fisher information matrix is equal to the inverse of *a posteriori* error covariance matrix, $\hat{\mathbf{S}}^{-1}$.

4 Applications

Since the first version (Wang et al. 2014) was released, UNL-VRTM has been used to investigate retrieval capabilities for aerosol, cloud, and surface information from a variety of current and future remote sensing instruments (see https://unl-vrtm.org for a full list of scientific publications using UNL-VRTM). For instance, it was used to

- evaluate the ability to improve simultaneous aerosol and surface retrievals by combining multispectral radiances from two geostationary satellites, GOES-R and TEMPO (Wang et al. 2014);
- study the information content contained in narrow-band and hyperspectral O_2 A- and B-band measurements for inferring aerosol vertical distribution (Ding and Wang 2016; Wang et al. 2014; Xu et al. 2018);
- develop retrieval algorithms for determining aerosol layer height from the DSCOVR/EPIC observations in the O_2 A and B bands (Xu et al. 2017, 2018);
- verify the capability for joint retrieval of hyperspectral surface reflectance and aerosol properties from the airborne GeoTASO instrument, which is a spectrometer prototype for the TEMPO and GEMS satellite missions (Hou et al. 2016, 2017);
- assess the capability for retrieving bi-modal aerosol particle size and refractive index from recently launched space-borne polarimeters, such as the Cloud and Aerosol Polarimetric Imager (CAPI) carried by the TanSat (Chen et al. 2017) and the Directional Polarimetric Camera (DPC) onboard the GaoFen-5 satellite (Hou et al. 2018; Li et al. 2018);

- retrieve bi-modal aerosol size and refractive index from AERONET multi-angular polarimetric measurements (Xu and Wang 2015; Xu et al. 2015);
- study the potential of the VIIRS Day/Night Band (DNB) for monitoring nighttime air quality (Wang et al. 2016);
- examine the sensitivity of TOA reflectance measured by MODIS to aerosol optical properties (Tao et al. 2017; Wang et al. 2017);
- evaluate the potential for simultaneous retrieval of cloud and above-cloud smoke microphysical properties from hyperspectral shortwave measurements (Xu et al. 2018);
- assess the benefit of combined infrared and shortwave hyperspectral observations for determining size-resolved dust optical properties and emitting sources (Xu et al. 2017). In this application, UNL-VRTM was integrated with two global chemistry transport models (FIM-Chem and GEOS-Chem) to perform observation system simulation experiments (OSSE) for the future CLARREO (Climate Absolute Radiance and Refractivity Observatory) satellite.

Here, we will discuss two of these applications to demonstrate how UNL-VRTM works as a remote sensing testbed. In the first application (Sect. 4.1), UNL-VRTM was used to explore shortwave spectral fingerprints of above-cloud smoke and to identify the retrievable parameters of joint aerosol-cloud from a shortwave spectrometer (Xu et al. 2018). In the second application (Sect. 4.2), we used UNL-VRTM to investigate the available information contained in AERONET multi-angular polarimetric observations for retrieving bi-modal aerosol microphysical properties (Xu and Wang 2015; Xu et al. 2015).

4.1 Spectral Fingerprints of Above-Cloud Smoke

Absorbing aerosols like smoke can heat the atmosphere by absorbing solar radiation, and such heating is enhanced when these aerosols are situated above liquid (water droplet) clouds. The presence of smoke over cloud also affects satellite remote sensing of cloud properties. When a cloud pixel is contaminated by lofted smoke aerosols, the TOA reflectance as observed by a satellite sensor is reduced and the spectral contrast increases. This may lead to a low bias of 6–20% in retrieved cloud optical depth (COD) and an underestimation of cloud effective radius (Meyer et al. 2013), which in turn results in biases in satellite-based estimates of cloud liquid water content and radiative effect. As such, it is desirable to simultaneously characterize the optical properties of smoke aerosols and underlying cloud droplets.

In this experiment, UNL-VRTM was used to investigate the spectral signature of above-cloud smoke, and to assess the capability for a joint inversion of cloud and aerosol optical thickness, along with their microphysical properties and vertical separation over an ocean surface. First, the tool was used to generate synthetic TOA reflectances in a 330–4000 nm range for a typical above-cloud smoke scenario. Then, an observation error covariance matrix was set up to account for instrumental noise

and model errors. Next, the spectral signatures of cloud and smoke were analyzed by examining the Jacobian sensitivities. Lastly, information content of the synthetic data was assessed in terms of DFS, and retrieval uncertainties were estimated.

In order to highlight the advantage of *hyperspectral* inversion, we compared information content extracted from *hyperspectral* observations with that obtained from MODIS-type *multispectral* data. As listed in Table 3, the former represents observations of a shortwave spectrometer with a resolution (FWHM) of 5 cm^{-1} measuring radiances in the range 333–4000 nm. For multispectral data, 13 MODIS channels falling within our simulated spectral range were considered, i.e. channels 1–7, 17–21, and 26. For each observation scenario, we considered two different spectral settings: (A) 400–2400 nm, and (B) 333–4000 nm. Setting B covers the full solar spectral range. In contrast, spectral setting A does not include the UV and medium-wave IR (MWIR), and is similar to the spectral range of the AVIRIS-NG instrument [https://aviris-ng.jpl.nasa.gov].

4.1.1 State Vector, Synthetic Data, and Error Covariance Matrices

The state vector comprises 13 cloud and aerosol parameters listed in Table 4, namely, 550-nm COD τ^{c}_{550}, cloud effective radius $r^{\mathrm{c}}_{\mathrm{eff}}$ and effective variance $v^{\mathrm{c}}_{\mathrm{eff}}$, above-cloud smoke AOD at 550 nm τ^{a}_{550}, smoke effective radius $r^{\mathrm{a}}_{\mathrm{eff}}$ and effective variance $v^{\mathrm{a}}_{\mathrm{eff}}$, real and imaginary parts of smoke refractive index with each represented by 3 principal components (PC), and the smoke-cloud separation height H. As such, the state vector can be expressed by

$$\mathbf{x} = \left[\tau^{\mathrm{c}}_{550}, r^{\mathrm{c}}_{\mathrm{eff}}, v^{\mathrm{c}}_{\mathrm{eff}}, \tau^{\mathrm{a}}_{550}, r^{\mathrm{a}}_{\mathrm{eff}}, v^{\mathrm{a}}_{\mathrm{eff}}, H, \mathbf{w}_{\mathrm{r}}, \mathbf{w}_{\mathrm{i}}\right]^T, \tag{82}$$

where each of $\mathbf{w}_{\mathrm{r}}$ and $\mathbf{w}_{\mathrm{i}}$ contains 3 amplitude values applied to the PCs of smoke refractive index. Principal component analysis for some refractive indices was to reduce the number of retrieval parameters. Cloud water droplets were assumed polydispersed with the Gamma PSD [(Eq. (88)], with the refractive index spectra reported by Downing and Williams (1975), Hale and Querry (1973), Kou et al. (1993). Smoke particles were polydispersed with the lognormal size distribution [Eq. (93)].

Table 3 List of observation scenarios considered for above-cloud aerosol simulations

Scenario	Observations included	Remark
Hyper A	300–4000 nm per 5 cm^{-1}	Full spectral shortwave
Hyper B	400–2400 nm per 5 cm^{-1}	Close to AVIRIS-NG spectral range
MODIS A	MODIS bands in 300–4000 nm	Has MWIR bands
MODIS B	MODIS bands in 400–2400 nm	No MWIR bands

Table 4 State vector values ($\mathbf{x}_a$), prior errors (ε_a), and posterior errors ($\hat{\varepsilon}$) for different observation scenarios

	Cloud parameters			Smoke parameters				PC weights of refractive index					
	τ_{550}^{c}	$\gamma_{\text{eff}}^{c}(\mu\text{m})$	ν_{eff}^{c}	$H(\text{km})$	τ_{550}^{a}	$\gamma_{\text{eff}}^{a}(\mu\text{m})$	ν_{eff}^{a}	$w_{r,1}$	$w_{r,2}$	$w_{r,3}$	$w_{i,1}$	$w_{i,2}$	$w_{i,3}$
x_a	10.0	10.0	0.1	3.0	0.5	0.12	0.18	0.0	0.0	0.0	0.0	0.0	0.0
ε_a	5.0	5.0	0.05	2.0	0.4	0.10	0.10	3.35	1.46	0.49	0.43	0.17	0.07
$\hat{\epsilon}_{\text{Hyper A}}$	0.41	0.39	0.02	0.44	0.09	0.02	0.09	2.43	1.20	0.42	0.14	0.07	0.03
$\hat{\epsilon}_{\text{Hyper A}}$	0.36	0.24	0.02	0.38	0.04	0.01	0.09	2.16	1.12	0.39	0.03	0.07	0.02
$\hat{\epsilon}_{\text{MODIS A}}$	1.07	0.65	0.05	1.71	0.18	0.04	0.10	3.30	1.46	0.49	0.35	0.16	0.07
$\hat{\epsilon}_{\text{MODIS A}}$	0.65	0.30	0.04	1.71	0.17	0.04	0.10	3.30	1.46	0.49	0.35	0.16	0.06

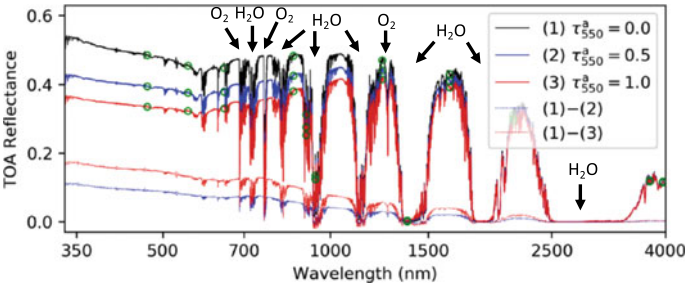

Fig. 14 TOA reflectance simulated by UNL-VRTM for cloud-only (black) and for two scenarios of over-cloud smoke with 550 nm AOD of 0.5 (solid blue) and 1.0 (solid red). Green circles indicate MODIS bands. Discontinuities in the reflectance spectra arise from the absorption of solar radiation by H_2O and O_2. Decreases in TOA reflectances due to the presence of smoke aerosols are indicated by dotted curves. Figure adapted from Xu et al. (2018)

State vector elements used by UNL-VRTM to simulate the synthetic data are compiled in Table 4. A thick optically uniform cloud layer with $\tau_{550}^{c} = 10$ between 1 and 2 km altitude was assumed. Cloud r_{eff}^{c} 10 μm and v_{eff}^{c} 0.1 were selected according to Nakajima et al. (1991). The overlying smoke plume was situated between 2 km and 8 km altitude, with the plume assumed to have a quasi-Gaussian vertical shape with peak extinction at 5 km. The relative height of smoke above cloud was thus 3 km, i.e., $H = 3$ km. Smoke r_{eff} (0.12 μm) and v_{eff} (0.18) were determined from AERONET measured biomass burning aerosols (Dubovik et al. 2002).

Figure 14 shows synthetic spectra of TOA reflectance simulated for two above-cloud smoke loadings (solid lines, $\tau_{550}^{a} = 0.5$ in blue and 1.0 in red), along with a cloud-only spectrum (black). Spectral discontinuities result from strong absorption by trace gases, such as H_2O at 0.72, 0.82, 0.94, 1.1, 1.35, 1.87, and 2.7–3.2 μm and O_2 at 0.68 and 0.76 μm and the O_2-N_2 collision-induced absorption at 1.26 μm. In the absence of smoke, the TOA reflectance of the cloud scene decreases from the UV to red spectral regions; this is largely an effect of Rayleigh scattering. In contrast, the presence of smoke over the cloud deck results in a reduction of TOA reflectance that depends linearly on the smoke burden. Such a reduction is more significant at shorter wavelengths, leading to a distinct spectral contrast.

As discussed in Sect. 3, realistic error characterizations for prior knowledge and synthetic data are of key importance in information content analysis. A priori uncertainties $\boldsymbol{\varepsilon}_a$ for retrieval parameters were specified to best represent their natural variability; these errors are listed in Table 4. The state vector error covariance matrix $\mathbf{S}_a$ was assumed diagonal, that is, a priori errors are uncorrelated.

Observation error covariance matrix is the sum of two terms

$$\mathbf{S}_{\varepsilon} = \mathbf{S}_y + \mathbf{S}_m. \tag{83}$$

Here, $\mathbf{S}_y$ is the error covariance matrix describing the instrument noises, and $\mathbf{S}_m$ the covariance matrix of forward model errors. We assumed that TOA reflectance

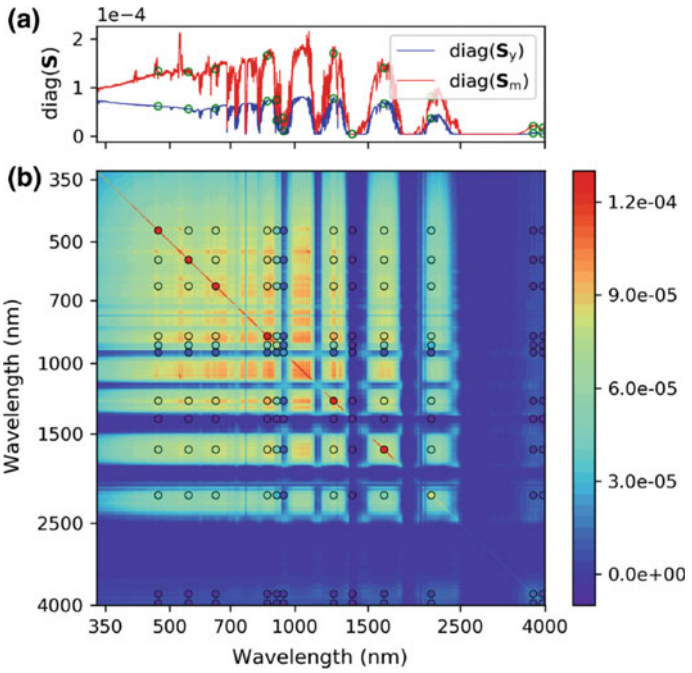

Fig. 15 Illustration of observation error covariance matrix. **a** Diagonal elements of instrumental and modeling error covariance matrices. **b** Graphics of the observation error covariance matrix. Circles indicate error covariance for MODIS-type observations. Figure adapted from Xu et al. (2018)

had a relative instrumental uncertainty of 2%, with lower-capped by an absolute reflectance error 0.002. For hyperspectral data, inter-channel correlations of instrument noise were limited to 5 adjacent channels on either side, with correlation coefficients decreasing from 0.95 to 0.20 away from the diagonal. This choice was made to reconcile spectral resolutions of some existing and future spectrometers, such as the AVIRIS-NG and TEMPO. Forward-model errors are usually caused by inaccurate model assumptions and uncertainties in model parametrizations. In practice, it is difficult to derive $\mathbf{S}_{\mathrm{m}}$ analytically, thanks to the complexity of forward model. Here, a Monte-Carlo method was used to produce an ensemble of simulations, from which the $\mathbf{S}_{\mathrm{m}}$ was calculated [see Xu et al. (2018) for details].

Figure 15a illustrates the diagonal elements of $\mathbf{S}_{\mathrm{y}}$ and $\mathbf{S}_{\mathrm{m}}$, and the summed $\mathbf{S}_{\varepsilon}$ is shown in Fig. 15b. Circles indicate $\mathbf{S}_{\varepsilon}$ for the MODIS-type observations. Diagonals are observation error variances, whereas the off-diagonal elements represent error correlations between observations, which are mainly characterized by the model error covariance matrix $\mathbf{S}_{\mathrm{m}}$. Gaps in the error covariance correspond to the locations of strong gas-absorbing bands.

4.1.2 Spectral Signatures of Cloud and Smoke

As calculated by UNL-VRTM, Jacobians of the TOA reflectances with respect to cloud and smoke parameters (found in the Jacobian matrix $\mathbf{K}$) can serve as a sensitivity metric to characterize spectral signatures for each relevant parameter. Rather than dealing directly with $\mathbf{K}$, we compared the matrices ε $(= [\mathrm{diag}(\mathbf{S}_\varepsilon)]^{\frac{1}{2}})$ and $\tilde{\varepsilon}$ $(= \mathbf{K}\mathbf{S}_\mathrm{a}^{\frac{1}{2}})$ in order to better analyze the spectral signature of each retrieved variable. Here, ε represents observation error; $\tilde{\varepsilon}$ is the Jacobian matrix normalized by prior errors, thus representing the natural variability of observation. Indeed, $\varepsilon^{-1}\tilde{\varepsilon}$ is equal to the pre-whitening matrix $\tilde{\mathbf{K}}$ defined in Eq. (75). For any spectrum, if the magnitude of $\tilde{\varepsilon}$ for a given parameter is less than the magnitude of ε, the TOA reflectance at this spectrum is not going to contain useful information for determining this parameter. Conversely, useful information will be gleaned if $\tilde{\varepsilon}$ has the larger magnitude.

Figure 16a–c shows the components of $\tilde{\varepsilon}$ for cloud droplet properties under two different smoke loadings (blue for $\tau_{550}^{\mathrm{a}} = 0.5$ and red for $\tau_{550}^{\mathrm{a}} = 1.0$). The filled grey areas indicate the ranges of observation error $\pm\varepsilon$. Clearly, the lofted smoke dims the sensitivity of TOA reflectance to cloud in the shorter wavelengths where smoke is optically significant (red versus blue curves), while the TOA reflectance could be increased by thickened cloud optical loading, reduced effective droplet size, or widened dispersion of droplet size. Also, the magnitudes of $\tilde{\varepsilon}$ for τ_{550}^{c} and $r_{\mathrm{eff}}^{\mathrm{c}}$ are significantly larger than those of the observation error. In contrast, the $\tilde{\varepsilon}$ for $v_{\mathrm{eff}}^{\mathrm{c}}$ remains weak until the spectral wavelength exceeds 1500 nm (Fig. 16c). Thus, TOA reflectances at wavelengths shorter than 1500 nm provide information for both COD and droplet size, whereas longer wavelengths provide information primarily on droplet size. This consderation has been used for satellite retrieval of $v_{\mathrm{eff}}^{\mathrm{c}}$ and COD (Platnick et al. 2003).

In contrast to cloud, the above-cloud smoke particles act distinctively on the TOA reflectance. Figure 16d–f shows $\tilde{\varepsilon}$ for smoke τ_{550}^{a}, $r_{\mathrm{eff}}^{\mathrm{a}}$, and $v_{\mathrm{eff}}^{\mathrm{a}}$, displaying overall negative sensitivities for these three variables. In particular, TOA reflectances in the UV-visible provide information primarily on τ_{550}^{a} (Fig. 16d), and at intermediate wavelengths in the visible-NIR, they provide information on both the τ_{550}^{a} and $r_{\mathrm{eff}}^{\mathrm{a}}$ (Fig. 16d–e). However, no information was found for $v_{\mathrm{eff}}^{\mathrm{a}}$, as the magnitudes of $\tilde{\varepsilon}$ for $v_{\mathrm{eff}}^{\mathrm{a}}$ are lower than observation error for the entire spectral range (Fig. 16f).

Figure 16g plots the $\tilde{\varepsilon}$ for cloud-aerosol separation H, which shows that radiances at UV and blue wavelengths reduce significantly as the aerosol smoke layer increases in altitude, because an elevated smoke layer absorbs solar radiation and reduces the chance of light being scattered by underlying clouds and air molecules. As such, the magnitude of this $\tilde{\varepsilon}$ falls off with the weakening of Rayleigh scattering at longer wavelengths. Indeed, the UV absorbing aerosol index, which represents the enhancement of spectral contrast in the UV by aerosol absorption, was found to be strongly sensitive to H (Torres et al. 1998). In addition, the signature for H is enhanced by absorptions of O_2 and H_2O at wavelengths between 680 and 1500 nm. While smoke aerosols absorb sunlight, they also scatter light back to space and reduce the chance of light being absorbed by underlying water vapor and O_2. Therefore, the higher of

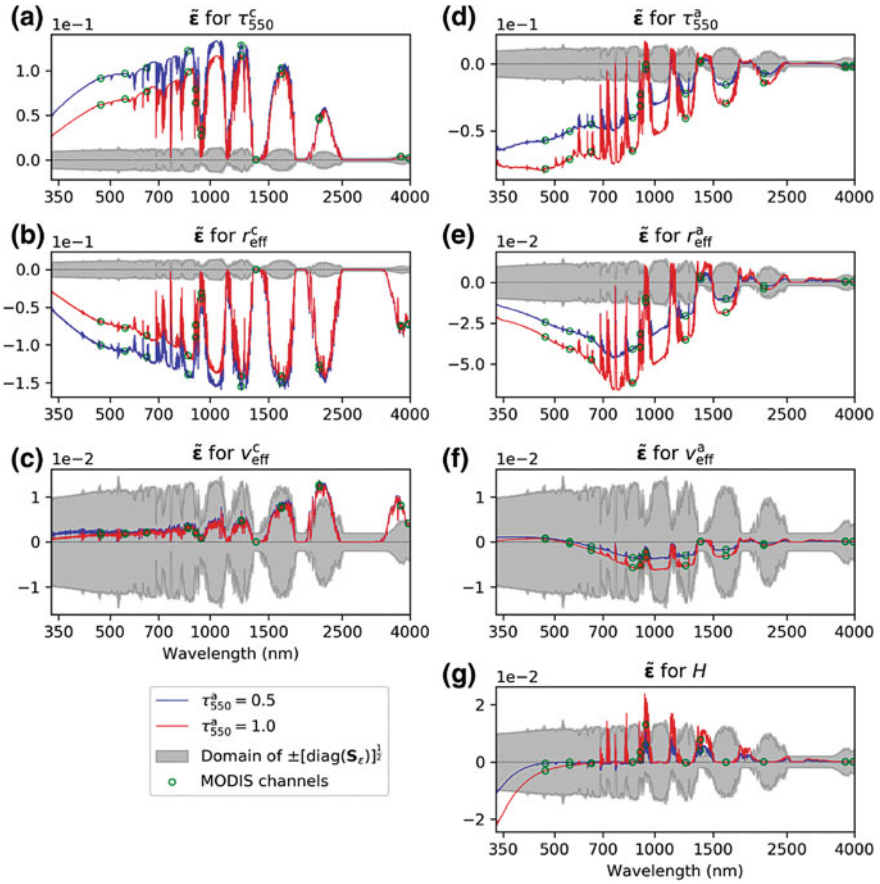

Fig. 16 $\tilde{\varepsilon}$ for seven smoke and cloud physical variables (solid lines). Filled grey areas indicates the range of observation error $\pm\varepsilon$. Circles indicate MODIS spectral bands. (Figure is adapted from Xu et al. (2018) and $\tilde{\varepsilon}$ for PC coefficients of smoke refractive index can be found from the same article.)

the smoke layer, the stronger the reflected radiative signals received by satellite; this principle has been used to derive layer height of aerosol and cloud (Dubuisson et al. 2009; Ding and Wang 2016).

4.1.3 Information Content and Retrieval Error

Based on the a priori and observation error covariances as noted already and the Jacobian matrix computed with UNL-VRTM, we have calculated the averaging-kernel matrix **A** [Eq. (78)] and the *a posteriori* error covariance matrix $\hat{\mathbf{S}}$ [Eq. (73)], for both the hyperspectral and MODIS-type observation scenarios defined in Table 3.

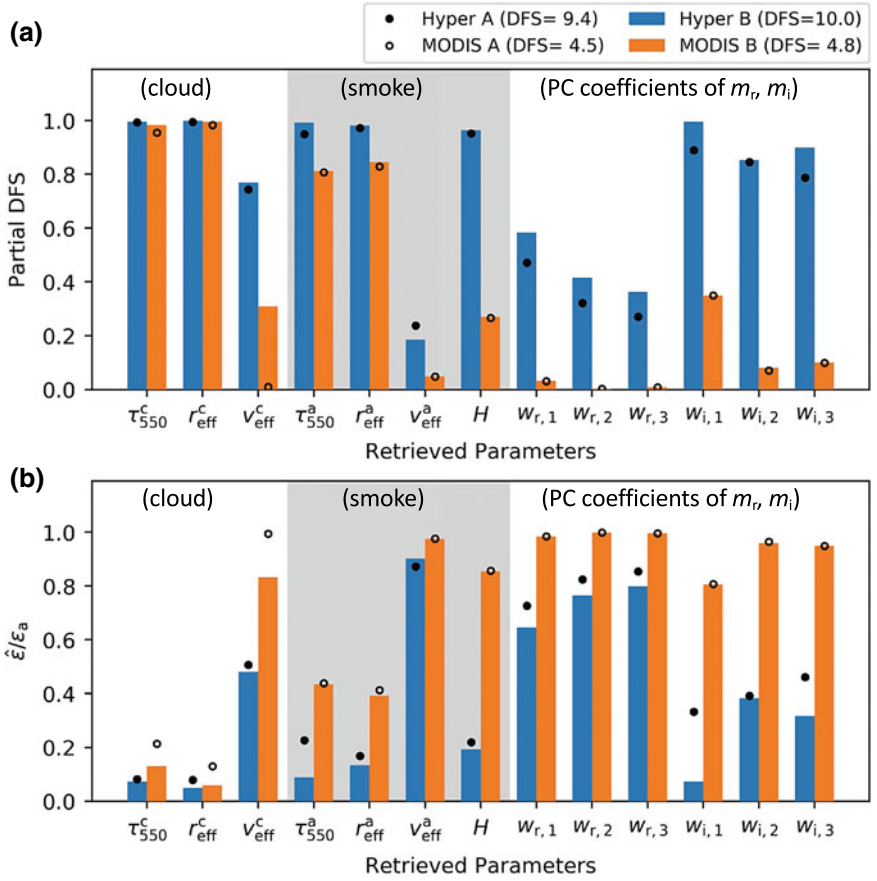

Fig. 17 Information content of hyperspectral (Hyper) and MODIS-type observations and resulting retrieval uncertainty for the cloud and smoke retrievals variable, for the case of $\tau^a_{550} = 0.5$. **a** Partial DFS values for each retrieved variable. **b** Ratio of retrieval error to prior error ($\hat{\varepsilon}/\varepsilon_a$) of each variable. Four observation scenarios are defined in Table 3. Figure adapted from Xu et al. (2018)

We then derived the total and partial DFS in Eqs. (79) and (80), as well as the retrieval error $\hat{\varepsilon}$ for each variable.

Figure 17 illustrates partial DFS values and the ratio of *a posteriori* error $\hat{\varepsilon}$ to a priori error ε_a for each state vector parameter. The values of $\hat{\varepsilon}$ for each parameter are also listed in Table 4. Overall, we found a total DFS of 10.0 for Hyper-B measurements, an increase of about 5 from that of MODIS-B measurements. In other words, the hyperspectral data contain enough additional information that can be used to retrieve about 5 extra parameters. The same amount of information increase was also found for observations in 400–2400 nm (i.e., Hyper-A versus MODIS-A).

According to Fig. 17a, MODIS-A and MODIS-B observations can yield 4.5 and 4.8 pieces of information, respectively. The difference of 0.3 DFS comes from the

information for $v_{\text{eff}}^{\text{c}}$ gained for MODIS-B measurements, as TOA reflectance in SWIR contains partial information for $v_{\text{eff}}^{\text{c}}$ (Fig. 16c). In general, information from MODIS-type observations is distributed primarily amongst the COD, $r_{\text{eff}}^{\text{c}}$, smoke AOD, and $r_{\text{eff}}^{\text{a}}$ variables. However, MODIS-type observations have difficulty resolving H, $v_{\text{eff}}^{\text{c}}$, $v_{\text{eff}}^{\text{a}}$, and the smoke refractive index.

Clearly, hyperspectral observations (for both the A and B spectral settings) can significantly advance the retrieval accuracy of these parameters excluding $v_{\text{eff}}^{\text{a}}$. Surprisingly, hyperspectral data also contain useful information for the complex smoke refractive index, especially the imaginary part, showing that aerosol absorption can be well retrieved from hyperspectral measurements. However, the use of hyperspectral data provides no additional information for improving retrievals of $v_{\text{eff}}^{\text{a}}$, and only limited information for retrieving the real part of refractive index.

4.2 Bi-Modal Aerosol Properties from Polarimetric Data

In contrast to the above example that focused on hyperspectral measurements, this application seeks to retrieve aerosol microphysical properties from polarimetric data collected by AERONET. AERONET's CIMEL-318 sun photometer measures not only direct and diffuse radiances, but also the state of light polarization from multiple viewing angles over many sites (Holben et al. 1998). The current AERONET operational inversion algorithm uses only the radiance data, although polarization measurements contain additional valuable information about aerosol size and refractive index (Hansen and Travis 1974; Mishchenko and Travis 1997). To achieve an improved aerosol microphysical characterization (Mishchenko et al. 2004), several studies have recommended the addition of polarization measurements to the AERONET inversion process (Xu and Wang 2015; Xu et al. 2015; Fedarenka et al. 2016).

In our study (Xu and Wang 2015), UNL-VRTM was used to address two key questions: (1) From a practical standpoint, what is the magnitude of the information content of AERONET's polarimetric measurements, for improving the retrieval of aerosol microphysical properties routinely derived from radiance-only measurements?; and (2) Hypothetically, how can we desgin future upgrades to the AERONET polarimetric measurements and the AERONET inversion algorithm to maximize the retrieval information contents? Answering these two questions is relevant not only to the future AERONET instrumentation design, but also for the ground-based passive polarimetric remote sensing of aerosols in general. Indeed, results from this study have helped to provide theoretical guidances towards a new AERONET research algorithm developed in a companion study (Xu et al. 2015).

Answers to above questions were sought from a theoretical perspective by investigating the available information contained in AERONET measurements with and without the inclusion of polarization data. The analysis started with the generation of synthetic measurements at four spectral bands (440, 675, 870, and 1020 nm) with UNL-VRTM for various types of spherical aerosol particles. Subsequently, the quan-

Table 5 List of AERONET observation scenarios used for information content analysis[a]

Scenario	Observations included	Remark
I1	τ_A, and I_{alm}	Observations used in AERONET inversion algorithm
I2	τ_A, I_{alm}, and I_{pp}	Scenario I1 plus principal-plane radiances
P1	τ_A, I_{alm}, I_{pp} and $DOLP_{pp}$	Scenario I2 plus principal-plane polarization
P2	τ_A, I_{alm}, and $DOLP_{alm}$	Scenario I1 plus almucantar polarization

[a]Variables are specified at four spectral wavelengths (440, 675, 870, and 1020 nm)

titative information content for retrieving aerosol parameters was identified for the four observation scenarios (I1, I2, P1, and P2) defined in Table 5.

Measurements in scenario I1 comprised the direct-sun AODs τ_A and the sky almucantar radiances I_{alm} that are used regularly in the AERONET operational inversion algorithm. The other three scenarios included different additional measurements: the solar principal-plane radiances I_{pp} were added (scenario I2), the solar principal-plane radiances I_{pp} and polarization $DOLP_{pp}$ were added (scenario P1), and the sky almucantar polarization $DOLP_{alm}$ was added (scenario P2). Here, the almucantar radiances I_{alm} are taken at a single zenith angle of the Sun but for 76 specified relative azimuth angless. The principal-plane polarization $DOLP_{pp}$ is a series of polarimetric measurements taken in the solar principal plane at 5° intervals in the viewing zenith angle, from the anti-solar side to the solar side. Note that $DOLP_{alm}$ is not routinely measured by any current sun photometer, but was included for comparative analysis.

4.2.1 State Vector, Synthetic Data, and Prior and Observation Errors

The state vector $\mathbf{x}$ has 22 parameters—11 each for the fine and coarse aerosol modes. The 11 mode variables are the columnar volume concentration V_0, the effective radius r_{eff}, the effective variance v_{eff}, and the complex refractive index $m_r + m_i i$ at 440, 675, 870, and 1020 nm. Aerosols are polydispersed with lognormal PSDs as in Eq. (50). Table 6 lists the PSD parameters for each mode that were used in the synthetic data simulation; also shown in brackets are their associated a priori uncertainties. The fine-mode particles correspondeds to water-soluble aerosol particles, while the coarse-mode is made up of large spherical particles with the refractive index for dust. In the study, fractional contributions of these two aerosols modes were varied in order to investigate scenarios from fine-dominated to well-mixed and coarse-dominated mixtures.

Synthetic AERONET observations were simulated with UNL-VRTM under various solar zenith angles from 40° to 75°. Figure 18 shows I_{alm} and $DOLP_{pp}$ for well-mixed aerosols (equal volumes of fine and coarse mode particles) at solar zenith

Table 6 Aerosol parameters (and prior errors) defined for fine and coarse modes[a]

Mode	r_{eff} (μm)	v_{eff}	m_{r}	m_{i}	ω_{A}
Fine	0.21 (80%)	0.25 (80%)	1.44, 1.44, 1.43, 1.42 (0.15)	0.009, 0.011, 0.012, 0.011 (0.01)	0.95, 0.93, 0.92, 0.91 0.151
Coarse	1.90 (80%)	0.41 (80%)	1.56, 1.55, 1.54, 1.54 (0.15)	0.004, 0.003, 0.003, 0.002 (0.005)	0.84, 0.91, 0.93, 0.96 0.198

[a]The complex refractive index $m_{\text{r}} - m_{\text{i}}i$, and single scattering albedo ω_{A} were reported at 440, 675, 870, and 1020 nm. Bracketed values are assumed a priori errors—relative errors for r_{eff} and v_{eff} but absolute for m_{r}, m_{i}, and ω_{A}

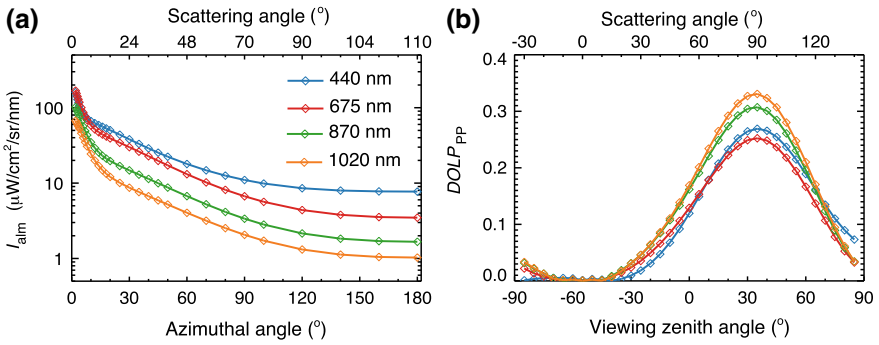

Fig. 18 Simulation of radiances and polarization by UNL-VRTM: **a** Radiances in the solar almucantar plane as a function of azimuth angle. **b** DOLP in the solar principal plane as a function of view zenith angle. Simulations are for columnar AOD of 1.0 at 440 nm. Solar zenith angle is 55° and top abscissae show the corresponding scattering angles. Figure adapted from Xu and Wang (2015)

angle of 55°. Simulations for other aerosol mixtures and other solar zenith angles show similar overall patterns. According to Fig. 18a, I_{alm} decreases as the scattering angle increases; this is as expected owing to the forward-dominated scattering phase functions of the aerosol particles. The peak DOLP_{pp} occurs at scattering angle 90°, as a result of composite effect of Rayleigh and aerosol scattering (Fig. 18b).

A priori errors ε_{a} of the retrieval parameters are given in Table 5. Uncertainties for aerosol microphysical parameters were based on aerosol climatology used in the companion study (Xu et al. 2015). The relative errors of r_{eff} and v_{eff} were set at 80% for both aerosol modes, with absolute errors 0.15 for m_{r} of both modes, 0.01 for fine-mode m_{i}, and 0.05 forcoarse-mode m_{i}. These prescribed a priori uncertainties produced errors 0.15 and 0.20 for the aerosol single scattering albedo (ω_{A}) of the fine-mode and coarse-mode, respectively. We postulated that the aerosol columnar volume concentrations for both modes were unknown with a relative uncertainty of 100%. We also assumed that the a priori uncertainties were uncorrelated, making $\mathbf{S}_{\text{a}}$ a diagonal matrix.

Observation errors for synthetic AERONET data were instrument calibration uncertainty and forward modeling error. We chose conservatively an absolute error of 0.02 for the direct-sun AOD, a relative uncertainty of 5% for I_{alm} and I_{pp}, and an absolute uncertainty of 0.01 for DOLP. These error assumptions were based on reported AERONET calibration uncertainties (Dubovik and King 2000; Holben et al. 1998). As to forward model error, a covariance matrix was calculated to represent errors in radiance and polarization incurred by limited knowledge of surface reflectivity (Xu and Wang 2015).

4.2.2 Aerosol Signatures in Angular Radiance and Polarization

The error-normalized (EN) Jacobians in Eq. (75) were calculated in order to examine the sensitivity of radiance and polarization to each element of the state vector. Figure 19 presents the EN Jacobians with respect to fine and coarse modal aerosol volumes, showing distinct angular signatures in DOLP_{pp} and I_{alm}. According to Fig. 19a, c, the radiance at scattering angles less than $\sim 10°$ decreases with increasing fine-mode aerosol loading (e.g. negative $\partial I_{\text{alm}}/\partial V_0$) and increases with increasing coarse-mode aerosol loading (e.g. positive $\partial I_{\text{alm}}/\partial V_0$), whereas the sensitivity of the I_{alm} to V_0 at larger scattering angles is more positive in the fine mode and less positive in the coarse mode. This occurs because large particles scatter more radiation than small particles at near-forward scattering angles. In contrast, the DOLP_{pp} exhibits strong sensitivity to aerosol V_0 of aerosol in both modes at the scattering angles between 45° and 135° (Fig. 19b, d).

Furthermore, the EN Jacobians of I_{alm} and DOLP_{pp} are also complementary in terms of their variation with wavelength. For example, the EN Jacobians of I_{alm} with respect to the fine-mode V_0 are lowest at 440 nm (blue curve in Fig. 19a), but those for DOLP_{pp} at 440 nm (blue curve in Fig. 19b) are the largest ones among these four spectral bands.

By comparing the EN Jacobians of I_{alm} and DOLP_{pp} with respect to all retrieved aerosol parameters (figures not shown here), our study (Xu and Wang 2015) showed in general that the DOLP_{pp} EN Jacobians have similar or larger magnitudes to these of I_{alm}, indicating that the DOLP_{pp} measurements possess equal or better than equal information for the inversion of these aerosol properties. Hence, adding such complementary DOLP_{pp} measurements to the current radiance-only inversion can potentially improve the retrieval accuracy.

4.2.3 Additional Information by Including Polarization

We calculated the averaging-kernel matrix **A**, DFS, and the *a posteriori* error for retrieved parameters for the four observation scenarios listed in Table 5. Figure 20 shows DFS as a function of solar zenith angle for three aerosol mixtures with AOD equal to 1.0 at 440 nm. The DFS in scenario I2 (red curves) ranges from 14 to 15 for the fine-dominated aerosol model, and from 17 to 19 for other two aerosol models;

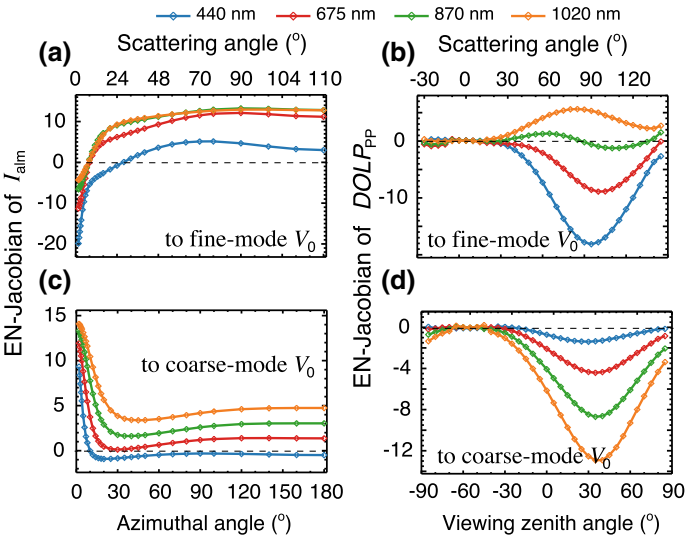

Fig. 19 Error-normalized Jacobians of almucantar radiances I_{alm} (left column) and degree of linear polarization $DOLP_{pp}$ (right column) with respect to aerosol volume, in the fine mode (top) and coarse mode (bottom). From the same UNL-VRTM simulations performed for Fig. 18. Adapted from Xu and Wang (2015)

values that are 2–3 higher than those obtained using AODs and I_{alm} measurements in the scenario I1 (black curves), indicating that sky radiances in the principal plane (I_{pp}) do contain additional information. The scenario P1 (green curves), which comprises I_{pp} and $DOLP_{pp}$, further increases DFS by 1–2. Observations in scenario P2 (blue curves)—radiance and polarization in the almucantar plane—yields DFS values slightly below those in the scenarios I2 and P1. Clearly, adding measurements in the solar principal plane into the inversion significantly increases the information content for aerosol properties, especially for combined I_{pp} and $DOLP_{pp}$. We also noted that the DFS increases with solar zenith angle for all cases; this is because observations at larger solar zenith angle enable a wider range of scattering angles, and thus contain more information on the aerosol scattering phase function and in turn on aerosol microphysical parameters.

For I1 and P1 scenarios, we further extended the analysis for 440 nm AOD varying from 0.1 to 2.0, and for fine-mode volume fraction fmf_v varying from 0.1 to 0.9. In practice, the fmf_v is inaccessible prior to inversion. To get round this, we used the Angstrom exponent (AE) from 870 to 1020 nm together with 440 nm AOD to define the aerosol conditions, because the AE in the longer pair of wavelengths is closely related to the fmf_v (Xu et al. 2015) and immediately available from the AERONET direct sun measurements. With the aerosol properties defined in the Table 5, changing the fmf_v from 0.1 to 0.9 resulted in AE values from 0.35 to 2.3.

Figure 21a, b displays the contours of DFS as a function of the AE (or fmf_v) and 440 nm AOD in the scenarios I1 and P1, respectively. We found that the DFS

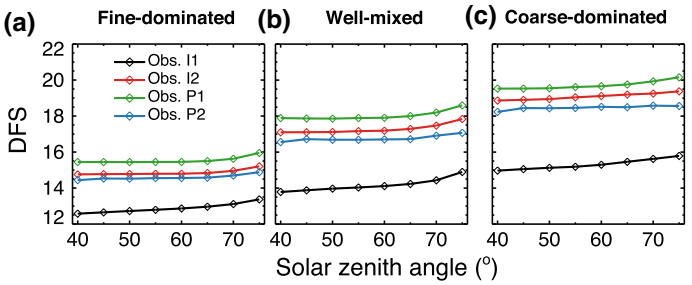

Fig. 20 DFS as a function of solar zenith angle for retrieving 22 parameters when using aerosol mixtures: **a** fine-dominated case with fmf_v of 0.8, **b** well-mixed case with fmf_v of 0.5, and **c** coarse-dominated case with fmf_v of 0.8. The four colors correspond to the observation scenarios listed in Table 5. Adapted from Xu and Wang (2015)

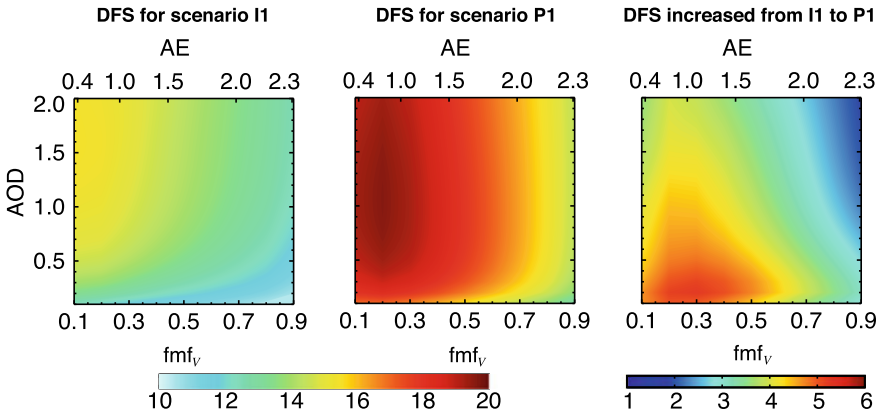

Fig. 21 Contours of DFS as a function of fmf_v and AOD in I1 (**a**) and P1 (**b**) scenarios. (**c**) the increase of DFS from (**a**) to (**b**). Simulations are for solar zenith angle of 55°. Adapted from Xu and Wang (2015)

decreases with the increase of fmf_v for the same AOD. This is because the coarse-mode parameters are more difficult to retrieve than their fine-mode counterparts, the former being constrained by their weaker sensitivities to the I_{alm} and $DOLP_{pp}$. Thus, lowering the coarse-mode fraction can significantly reduce aerosol information for coarse-mode parameters, but it will retain the information for fine-mode parameters, although resulting in a net decrease of the total DFS.

We also noticed from Fig. 21a that the DFS increases with an increasing AOD in scenario I1. However, AOD change has less impact in the scenario P1 (Fig. 21b). For example, the DFS values are lower than 14 when AOD < 0.4 in the scenario I1, whereas even larger DFS can be found in scenario P1 when AOD < 0.2. Therefore, we may expect that the inversion in the scenario P1 will be capable of retrieving aerosol parameters for situations with smaller aerosol loading. Finally, as seen in Fig. 21c, the addition of I_{pp} and $DOLP_{pp}$ in the inversion can add 2–5 pieces of

useful information. Such an improvement is apparent for all aerosol conditions but is more marked when larger numbers of coarse particles are present: $fmf_v < 0.5$ (or AE< 1.6), in which the radiance-only inversion usually yields a large retrieval error for the fine-mode aerosol.

We also analyzed the improvements in retrieval accuracy for individual parameters. The smallest retrieval errors were always found in the scenario P1, showing that the addition of principal-plane polarization data could reduce retrieval uncertainties by at least 50% for all parameters (Xu and Wang 2015). In addition, our findings also agreed with those of Dubovik and King (2000), in that the radiance-only inversion was unable to resolve bimodal refractive index values and single scattering albedo under. However, observations in scenario P1 could allow bimodal retrievals of these parameters when $0.7 < AE < 1.6$. Such considerations can help us in practical to determine whether a monomodal or bimodal retrieval of aerosol refractive index is possible.

5 Summary and Outlook

With integrated components for forward scattering and radiative transfer modeling, and Bayesian-based inverse modeling, UNL-VRTM is an ideal testbed for the investigation of remote sensing applications, especially for those involving aerosol retrievals. The forward modeling components of UNL-VRTM take advantage of many valuable developments from the community, including the state-of-the-art VLIDORT model, the linearized Mie and T-matrix codes, the HITRAN line-spectroscopic absorption database, and the MT_CKD continuum absorption code, etc. Our development emphasizes the integration of these available modules into a unified testbed tool that can objectively assess useful information of an observation system. The model package is public available through https://unl-vrtm.org. In summary, UNL-VRTM has following features:

- It gives a rigorous and integrated treatment of the necessary physical processes (such as absorption of trace gases, molecular and particle scattering, surface reflection, and radiative transfer);
- It can perform accurate simulations of measured quantities for any remote sensing observation system, including radiances and polarization;
- It can perform accurate hyperspectral simulations from the UV to thermal IR in the spectral range of 0.2–40 μm;
- It can compute directly the profile and columnar sensitivities (Jacobians) of measured quantities with respect to aerosol parameters (bi-modal AOD, volume, single scattering albedo, particle size parameters, refractive index, particle shape factor, and vertical profile), gas absorption optical depth and mixing ratio, and surface reflectance parameters;
- It can be used to quantify information content for any observational system for retrieving interested aerosol, gas, and/or surface parameters;

- It has a simple interface allowing the user to flexibly configure forward modeling simulations in a versatile manner.

There are several ongoing efforts to improve UNL-VRTM's capability. First, a database of scattering optical properties for non-spherical particles provided by Meng et al. (2010) is being incorporated (Chen et al. 2018). This dataset will extend the aerosol capability, as the linearized T-matrix code in UNL-VRTM has difficulties dealing with large non-spherical dust-like particles. Second, a UNL-VRTM-based night-time radiative transfer model is under construction (Zhou et al. 2018). Such a development involves adding spectral illumination sources from the moon, nighttime city lights, and wild fires. This additional model will be useful for night-time aerosol and cloud remote sensing [such as from the VIIRS DNB (Wang et al. 2016)]. Thirdly, the bi-modal treatment of aerosols is being expanded to incorporate multiple aerosol modes; this will enable modeling for a greater variety of aerosol (and cloud) mixtures. Finally, with further upgrades in the future and an expanding user community, we anticipate that UNL-VRTM will find more applications in Earth remote sensing, and we look forward to collaborations on these subjects with colleagues in the user community.

Acknowledgements The authors would like to particularly thank Robert Spurr for his generosity sharing and supporting his VLIDORT, linearized Mie, and Linearized T-matrix codes, Xiong Liu and Kelly Chance for their help on implementing HITRAN calculations, and Daven Henze for many discussions on inverse modeling. We are grateful to all those who have provided support and advice during the UNL-VRTM development: Jing Zeng, Xianglei Huang, Xu Liu, Oleg Dubovik, Ping Yang, and Michael Mishchenko. We also appreciate data support from HITRAN team and the ASTER Spectral Library. Xiuhong Chen and Xianglei Huang kindly provided MODTRAN5 simulations and IR validation. We thank all the users of UNL-VRTM for their constructive feedback. We also thank Robert Spurr and Alexander Kokhanovsky for their insightful comments to the original manuscript. We thank the following programs for supporting the development of UNL-VRTM: NASA Radiation Science program, NASA Atmospheric Composition Modeling and Analysis program (ACMAP), NASA Earth and Space Science Fellowship, NASAs TEMPO, MAIA, and GEO-CAPE satellite mission programs, as well as Office of Naval Research (ONR)'s Multidisciplinary University Research Initiatives (MURI) program.

Appendices

Appendix 1 Particle Size Distributions (PSDs)

Size distribution is an important microphysical property describing the size dispersion of a collection of aerosol particles in the atmosphere. The particle *number* size distribution function is often expressed by $N(r)$, and with $N(r)\mathrm{d}r$ denoting the number of particles per unit volume with radii between r and $r + \mathrm{d}r$. One can also write $N(r) = \frac{\mathrm{d}N}{\mathrm{d}r}$. If r_1 and r_2 are the smallest and largest radii, the total number of particles per unit volume is

$$N_0 = \int_{r_1}^{r_2} N(r)\mathrm{d}r. \tag{84}$$

It is often convenient to normalize the distribution function to unity, that is, $N_0 = 1$.

Two important parameters of a size distribution are the effective radius r_{eff} and effective variance v_{eff}, defined as

$$r_{\mathrm{eff}} = \frac{1}{G}\int_{r_1}^{r_2} r\pi r^2 N(r)\mathrm{d}r, \tag{85}$$

$$v_{\mathrm{eff}} = \frac{1}{Gr_{\mathrm{eff}}^2}\int_{r_1}^{r_2} (r - r_{\mathrm{eff}})^2 \pi r^2 N(r)\mathrm{d}r, \tag{86}$$

where G is the geometric cross-sectional area of particles per unit volume,

$$G = \int_{r_1}^{r_2} \pi r^2 N(r)\mathrm{d}r. \tag{87}$$

Here we summarize the analytical PSD functions implemented in the linearized Mie and linearized T-matrix codes (Spurr et al. 2012), including the 'gamma', 'modified gamma', 'lognormal', and 'power law' size distributions. Fuller descriptions for these functions can be found in Hansen and Travis (1974), Mishchenko and Travis (1998). Among these, the lognormal function has seen probably the widest applications in modeling aerosol microphysics, and for this PSD, we will discuss further the conventions for lognormal distribution applied to particle *number*, *area*, and *volume* distributions.

Gamma Distributions

The standard gamma distribution function is given by

$$N(r) = \frac{N_0\beta}{\Gamma(\alpha+1)}(\beta r)^{\alpha}\exp(-\beta r), \tag{88}$$

where Γ indicates the gamma function. There are two free parameters α and β, which are related to effective radius r_{eff} and effective variance v_{eff} by

$$\alpha = \frac{1-3v_{\mathrm{eff}}}{v_{\mathrm{eff}}} \quad \text{and} \quad \beta = \frac{1}{r_{\mathrm{eff}}v_{\mathrm{eff}}}. \tag{89}$$

The bimodal gamma distribution is given by

$$N(r) = \frac{1}{2}\frac{N_0\beta_1}{\Gamma(\alpha+1)}(\beta_1 r)^{\alpha}\exp(-\beta_1 r) + \frac{1}{2}\frac{N_0\beta_2}{\Gamma(\alpha+1)}(\beta_2 r)^{\alpha}\exp(-\beta_2 r). \tag{90}$$

The two modes are described by two different r_{eff} values, but with the same value for v_{eff} and the same number of particles.

Another related gamma distribution is the modified gamma PSD, which is controlled by three free parameters α, r_c, and γ:

$$N(r) = \frac{N_0 \gamma}{r_c \Gamma\left(\frac{\alpha+1}{\gamma}\right)} \left(\frac{\alpha}{\gamma}\right)^{(\alpha+1)/\gamma} \left(\frac{r}{r_c}\right)^{\alpha} \exp\left[-\frac{\alpha}{\gamma}\left(\frac{r}{r_c}\right)^{\gamma}\right]. \tag{91}$$

Power Law Distribution

The power law size distribution is

$$N(r) = N_0 \frac{2 r_1 r_2}{r_2^2 - r_1^2} r^{-\alpha}, \quad \text{for} \quad r_1 \le r \le r_2. \tag{92}$$

This distribution also has three free parameters: the smallest radius r_1, the largest radius r_2, and the exponential term α; the value $\alpha = 3$ was used by Hansen and Travis (1974).

Lognormal Distribution

The basic definition for the lognormal PSD in terms of the *number* distribution is

$$N(r) = \frac{N_0}{r \ln \sigma_g \sqrt{2\pi}} \exp\left(-\frac{(\ln r - \ln r_g)^2}{2 \ln^2 \sigma_g}\right), \tag{93}$$

where the two parameters r_g and σ_g are the geometric *number* mean radius and standard deviation with $\sigma_g > 1$.

However, it turns out that N_0, r_g, and σ_g are not so convenient to characterize the PSD from the observational and modeling perspectives. A better alternative is to use the *area* or *volume* distributions, which are similarly formulated with the same σ_g but with two other parameters, namely, the total cross-sectional area of particles S_0 and geometric area mean radius r_s for the *area* distribution, and total particle volume V_0 and geometric volume mean radius r_v for the *volume* distribution (Seinfeld et al. 2006):

$$S(r) = \frac{S_0}{r \ln \sigma_g \sqrt{2\pi}} \exp\left(-\frac{(\ln r - \ln r_s)^2}{2 \ln^2 \sigma_g}\right), \tag{94}$$

$$V(r) = \frac{V_0}{r \ln \sigma_g \sqrt{2\pi}} \exp\left(-\frac{(\ln r - \ln r_v)^2}{2 \ln^2 \sigma_g}\right). \tag{95}$$

The geometric mean radius r_s and r_v can be calculated from r_g and σ_g by

$$r_s = r_g \exp(2\ln^2 \sigma_g) \quad \text{and} \quad r_v = r_g \exp(3\ln^2 \sigma_g). \tag{96}$$

The total cross-sectional area S_0 and volume V_0 can also be derived analytically from the total number N_0 by

$$S_0 = N_0 \pi r_g^2 \exp\left(\frac{4\ln^2 \sigma_g}{2}\right) \quad \text{and} \quad V_0 = N_0 \frac{4\pi}{3} r_g^3 \exp\left(\frac{9\ln^2 \sigma_g}{2}\right). \tag{97}$$

Moreover, the effective size parameters are related to the geometric number and volume mean radius by

$$r_{\text{eff}} = r_g \exp\left(\frac{5}{2}\ln^2 \sigma_g\right) = r_v \exp\left(-\frac{1}{2}\ln^2 \sigma_g\right), \tag{98}$$

$$v_{\text{eff}} = \exp(\ln^2 \sigma_g) - 1. \tag{99}$$

Relating AOD to extinction efficiency factor: The aerosol optical thickness can be defined in terms of the extinction cross section C_{ext} multiplied by the total particle number:

$$\tau = N_0 C_{\text{ext}}. \tag{100}$$

When we replace N_0 by V_0 from Eq. (97) and apply r_{eff} with Eq. (98), we can derive τ directly from the total aerosol particle volume

$$\begin{aligned}
\tau &= \frac{3}{4\pi r_g^3 \exp\left(\frac{9\ln^2 \sigma_g}{2}\right)} V_0 C_{\text{ext}} \\
&= \frac{3}{4\pi r_g^2 \exp\left(\frac{4\ln^2 \sigma_g}{2}\right) r_g \exp\left(\frac{5\ln^2 \sigma_g}{2}\right)} V_0 C_{\text{ext}} \\
&= \frac{3V_0}{4r_{\text{eff}}} \frac{C_{\text{ext}}}{G} = \frac{3V_0}{4r_{\text{eff}}} Q_{\text{ext}},
\end{aligned} \tag{101}$$

where $G = S_0/N_0$ is the geometric cross-sectional area, and $Q_{\text{ext}} = C_{\text{ext}}/G$ is the extinction efficiency factor. Moreover, aerosol particle mass burden M can also be related to τ through the aerosol density ρ:

$$\tau = \frac{3M}{4\rho r_{\text{eff}}} Q_{\text{ext}}. \tag{102}$$

Appendix 2 BRDF and BPDF Kernels

For convenience, we list here the anisotropic BRDF and BPDF kernels used in UNL-VRTM. Program codes of these kernels are part of the VLIDORT model as a supplementary package (Spurr 2006). Full details may be found in the literature. These kernels were analytically linearized to calculate partial derivatives with respect to specific kernel input parameters, and detailed derivations for the linearization of most kernels can be found in Spurr (2004).

Note that these kernels are functions of the incident and reflected directional angles (zenith angle of incident beam θ_0, zenith angle of reflected beam θ, and the relative azimuth angle $\Delta\phi$) and spectral wavelength λ. λ is omitted in these equations for simplification. In most situations, we use μ and μ_0 to respectively represent $\cos\theta$ and $\cos\theta_0$. In addition, many kernels also use the *phase angle* of scattering (or reflection) ξ which is supplementary to the scattering angle Θ, i.e., $\xi = \pi - \Theta$, and thus

$$\cos\xi = \cos\theta\cos\theta_0 + \sin\theta\sin\theta_0\cos\Delta\phi. \tag{103}$$

Ross-Thin and Ross-Thick Kernels

Ross-type kernels are empirical volume-scattering models applied to optically thick and thin vegetation canopies (Ross 1981; Wanner et al. 1995):

$$f_{\text{thick}}(\theta, \theta_0, \Delta\phi) = \frac{(\pi/2 - \xi)\cos\xi + \sin\xi}{\mu + \mu_0} - \frac{\pi}{4}, \tag{104}$$

$$f_{\text{thin}}(\theta, \theta_0, \Delta\phi) = \frac{(\pi/2 - \xi)\cos\xi + \sin\xi}{\mu\mu_0} - \frac{\pi}{2}. \tag{105}$$

Ross-type kernels have no non-linear parameters and were derived from radiative transfer theory applied to a layer of randomly oriented scattering facets (leaves) over a surface of known Lambertian albedo (Ross 1981).

Li-Sparse and Li-Dense Kernels

Li-type kernels are geometric scattering models derived for sparse and dense vegetation cover by consideration of the mutual shadowing effect of the canopy (Li and Strahler 1992; Wanner et al. 1995). Tree crowns are assumed to be spheroids of vertical dimension b, horizontal dimension r, with their centers at height h above the ground. Two free parameters thus characterize the kernel's shape, namely, the crown ratio b/r and height ratio h/b. The BRDF functions are given by

$$f_{\text{sparse}}(\theta, \theta_0, \Delta\phi) = \frac{1}{2}(1 - \cos\xi')\sec\theta'\sec\theta_0' - \left[\sec\theta_0' + \sec\theta' - O(\theta, \theta_0, \Delta\phi)\right], \quad (106)$$

$$f_{\text{dense}}(\theta, \theta_0, \Delta\phi) = \frac{(1 - \cos\xi')\sec\theta'\sec\theta_0'}{\sec\theta_0' + \sec\theta' - O(\theta, \theta_0, \Delta\phi)} - 2, \quad (107)$$

where θ', θ_0', and ξ' are locally adjusted adjusted view zenith angle, solar zenith angle, and phase angle:

$$\theta' = \tan^{-1}\left(\frac{b}{r}\tan\theta\right), \qquad \theta_0' = \tan^{-1}\left(\frac{b}{r}\tan\theta_0\right), \quad \text{and} \quad (108)$$

$$\cos\xi' = \cos\theta'\cos\theta_0' + \sin\theta'\sin\theta_0'\cos\Delta\phi. \quad (109)$$

The term $O(\theta, \theta_0, \Delta\phi)$ in Li kernels represents the overlapping area between view and solar shadows and is expressed by

$$O(\theta, \theta_0, \Delta\phi) = \frac{1}{\pi}(1 - \sin t\cos t)(\sec\theta_0' + \sec\theta'), \quad (110)$$

where t satisfies

$$\cos t = \frac{h}{b}\frac{\sqrt{D^2 + (\tan\theta_0'\tan\theta'\tan\Delta\phi)^2}}{\sec\theta_0' + \sec\theta'}, \quad (111)$$

$$D = \sqrt{\tan^2\theta_0' + \tan^2\theta' - 2\tan\theta_0'\tan\theta'\cos\Delta\phi}. \quad (112)$$

Hapke Kernel

The Hapke (1993) has three free parameters:

$$f_{\text{hapke}}(\theta, \theta_0, \Delta\phi) = \frac{\omega}{4(\mu_0 + \mu)}\left[(1 + B(\xi))P(\xi) + T(\theta_0)T(\theta) - 1\right], \quad (113)$$

where ω and $P(\xi)$ are the single scattering albedo and phase function of the surface material. The phase function is given by $P(\xi) = 1 + \frac{1}{2}\cos\xi$. The term $1 + B(\xi)$ explicitly accounts for the hot spot with

$$B(\xi) = \frac{B_0 h}{h + \tan\frac{\xi}{2}}. \quad (114)$$

The multi-scattering term $T(\theta_0)T(\theta)$ is defined factors

$$T(\theta) = \frac{1 + 2\cos\theta}{1 + 2\cos\theta\sqrt{1-\omega}}. \tag{115}$$

The three free parameters are the single scattering albedo ω, the amplitude (B_0) and the angular width (h) of the hot spot.

Roujean Kernel

This is a geometric kernel developed by Roujean et al. (1992). It has no free parameter and is given by

$$f_{\text{roujean}}(\theta, \theta_0, \Delta\phi) = \frac{1}{2\pi}[(\pi - \Delta\phi)\cos\Delta\phi + \sin\Delta\phi]\tan\theta_0\tan\theta - \frac{1}{\pi}(\tan\theta + \tan\theta_0 + G), \tag{116}$$

with a geometric factor G defined by

$$G(\theta, \theta_0, \Delta\phi) = \sqrt{\tan^2\theta_0 + \tan^2\theta - 2\tan\theta_0\tan\theta\cos\Delta\phi} \tag{117}$$

Rahman (RPV) Kernel

The Rahman or the Rahman-Pinty-Verstraete(RPV) BRDF model was developed by Rahman et al. (1993), and is based on a reflection mode developed for lunar surface (Minneaert 1941):

$$f_{\text{rahman}}(\theta, \theta_0, \Delta\phi) = \rho_0 \frac{(\mu_0\mu)^{k-1}}{(\mu_0 + \mu)^{1-k}} F(\xi)[1 + R(G)], \tag{118}$$

where ξ is scattering phase angle defined in Eq. (103) and $F(\xi)$ is the Henyey-Greenstein scattering phase function characterized by an asymmetry factor g,

$$F(\xi) = \frac{1 - g^2}{\left[1 + g^2 - 2g\cos(\pi - \xi)\right]^{3/2}}. \tag{119}$$

And $1 + R(G) = 1 + (1 - \rho_0)/(1 + G)$ explicitly accounts for the hot spot with G the same geometric factor defined for the Roujean kernel in Eq. (117).

Hence, Rahman kernel has three free parameters, namely ρ_0 for overall amplitude, g for Henyey-Greenstein phase function, and k for characterizing the angular spread.

Maignan Kernel

This is a land surface BPDF kernel developed by Maignan et al. (2009) through an analysis of multi-year PARASOL observations. It has one free parameters ν, the Normalized Difference Vegetation Index (NDVI). The polarized reflectance tends to decrease (by a factor of $e^{-\nu}$) with increasing vegetation cover, and the kernel function is given by

$$f_{\text{maignan}}(\theta, \theta_0, \Delta\phi) = \frac{Ce^{-(\nu+\tan\gamma)}}{4(\mu_0+\mu)}\mathbf{F}_{\text{r}}(\gamma, m), \tag{120}$$

where C is a constant chosen for certain surface type, m is the refractive index of the vegetation canopy (taken to be 1.5), and $\gamma = \xi/2$. $\mathbf{F}_{\text{r}}(\gamma, m)$ is the Fresnel reflection matrix having 8 non-zero elements (Kokhanovsky et al. 2015):

$$F_{\text{r11}} = F_{\text{r22}} = (R_{\parallel}R_{\parallel}^{*} + R_{\perp}R_{\perp}^{*})/2, \tag{121}$$

$$F_{\text{r12}} = F_{\text{r21}} = (R_{\parallel}R_{\parallel}^{*} - R_{\perp}R_{\perp}^{*})/2, \tag{122}$$

$$F_{\text{r33}} = F_{\text{r44}} = (R_{\parallel}R_{\perp}^{*} + R_{\perp}R_{\parallel}^{*})/2, \tag{123}$$

$$F_{\text{r34}} = F_{\text{r43}} = i(R_{\parallel}R_{\perp}^{*} - R_{\perp}R_{\parallel}^{*})/2. \tag{124}$$

Here, the asterisk symbol indicates the conjugate of a complex number, and $R_{\parallel}$ and $R_{\perp}$ are defined as

$$R_{\parallel} = \frac{m\cos\gamma - \cos\gamma\prime}{m\cos\gamma + \cos\gamma\prime}, \tag{125}$$

$$R_{\perp} = \frac{\cos\gamma - m\cos\gamma\prime}{\cos\gamma + m\cos\gamma\prime}, \tag{126}$$

where $\gamma\prime$ is related to γ through the Snell's refraction law and is given as:

$$\sin\gamma\prime = \frac{\sin\gamma}{m}. \tag{127}$$

Cox-Munk and GISS-Cox-Munk Kernels

The ocean glitter specular kernels in the VLIDORT package include a scalar Cox-Munk kernel (Cox et al. 1954) and a vector GISS-Cox-Munk kernel (Mishchenko and Travis 1997). Both the kernels have two free parameters; one is the water refractive index m, and the other one is the geometric factor σ^2 empirically related to wind speed w through $\sigma^2 = 0.003 + 0.00512w$.

The scalar Cox-Munk kernel is given by

$$f_{\text{cox-munk}} = F_{\text{r11}}(\gamma, m)P(\theta_0, \theta, \Delta\phi, \sigma^2), \tag{128}$$

where $F_{r11}(\gamma, m)$ is the (1,1) element of the Fresnel reflection matrix, and $\gamma = \xi/2$. The probability function describing the glitter is given by

$$P(\theta_0, \theta, \Delta\phi, \sigma^2) = \frac{4\cos^4\frac{\xi}{2}}{\mu\mu_0\pi\sigma^2}\exp\left[-\frac{\tan^2(\frac{\pi}{2} - \sin^{-1}\frac{\xi}{2})}{\sigma^2}\right]. \tag{129}$$

To account for shadowing effects of water waves, the kernel is multiplied by a bidirectional shadow function given by Sancer (1969).

The vector GISS-Cox-Munk kernel function was based on the description in Mishchenko and Travis (1997), which has a similar formulation to the above, but it now considers the full 4×4 Fresnel reflection matrix. However, *it should be noted that the input parameters in UNL-VRTM is defined as* (σ^2, m^2) *for the Cox-Munk kernel, but as* $(0.5\sigma^2, m)$ *for the GISS-Cox-Munk kernel.*

Appendix 3 Derivation of the Transformation Matrix $\boldsymbol{\Pi}$

This appendix presents derivations of equations (57) and (59) in the main text, along with the expressions in Tables 1 and 2. It should be noted that all optical parameters are functions of wavelength and defined for each atmospheric layer, but for reasons of clarity, we will omit the wavelength dependence and drop the layer index in the following.

Let x be an aerosol microphysical parameter. The aerosol extinction and scattering optical thickness (τ_A and δ_A), single scattering albedo (ω_A), and Greek coefficient matrix ($\mathbf{B}_A^j$) are functions of x. However, gaseous absorption and Rayleigh scattering parameters are independent of x.

First, we transform Eq. (56) as follows:

$$\phi_x = \frac{x}{\tau}\frac{\partial\tau}{\partial x} = \frac{x}{\tau}\frac{\partial(\tau_G + \tau_R + \tau_A)}{\partial x} = \frac{1}{\tau}x\frac{\partial\tau_\mathbf{A}}{\partial x} \tag{130}$$

$$\begin{aligned}\varphi_x &= \frac{x}{\omega}\frac{\partial\omega}{\partial x} = \frac{x}{\omega}\frac{\partial[(\delta_A + \tau_G)/\tau]}{\partial x} \\ &= \frac{x}{\omega}\frac{1}{\tau^2}\left[\tau\frac{\partial(\delta_A + \tau_R)}{\partial x} - (\delta_A + \tau_R)\frac{\partial\tau}{\partial x}\right] \\ &= \frac{x}{\omega\tau}\frac{\partial\delta_\mathbf{A}}{\partial x} - (\delta_A + \tau_R)\frac{x}{\omega\tau^2}\frac{\partial\tau_\mathbf{A}}{\partial x} \\ &= \frac{x}{\delta_A + \tau_R}\frac{\partial\delta_\mathbf{A}}{\partial x} - \frac{1}{\tau}\frac{\partial\tau_\mathbf{A}}{\partial x} \\ &= \frac{x}{\delta_A + \tau_R}\frac{\partial\delta_\mathbf{A}}{\partial x} - \phi_x\end{aligned} \tag{131}$$

$$\boldsymbol{\Psi}_x^j = \frac{x}{\mathbf{B}^j}\frac{\partial\mathbf{B}^j}{\partial x} = \frac{x}{\mathbf{B}^j}\frac{\partial[(\tau_R\mathbf{B}_R^j + \delta_A\mathbf{B}_A^j)/(\delta_A + \tau_R)]}{\partial x}$$

$$= \frac{x}{\mathbf{B}^j}\frac{1}{(\delta_\mathrm{A}+\tau_\mathrm{R})^2}\left[(\delta_\mathrm{A}+\tau_\mathrm{R})\frac{\partial(\delta_\mathrm{A}\mathbf{B}_\mathrm{A}^j)}{\partial x} - (\tau_\mathrm{R}\mathbf{B}_\mathrm{R}^j + \delta_\mathrm{A}\mathbf{B}_\mathrm{A}^j)\frac{\partial\delta_\mathbf{A}}{\partial x}\right]$$

$$= \frac{x}{\mathbf{B}^j}\frac{1}{\delta_\mathrm{A}+\tau_\mathrm{R}}\left[\frac{\partial(\delta_\mathrm{A}\mathbf{B}_\mathrm{A}^j)}{\partial x} - \mathbf{B}^j\frac{\partial\delta_\mathbf{A}}{\partial x}\right]$$

$$= \frac{1}{(\delta_\mathrm{A}+\tau_\mathrm{R})\mathbf{B}^j}\left[\delta_\mathrm{A}x\frac{\mathbf{B}_\mathrm{A}^j}{\partial x} + (\mathbf{B}_\mathrm{A}^j - \mathbf{B}^j)x\frac{\partial\delta_\mathbf{A}}{\partial x}\right] \tag{132}$$

These expressions are linear combinations of ϕ'_x, φ'_x, and $\boldsymbol{\Psi}'^j_x$ (as defined by Eq. (58)), where

$$\left[\phi'_x, \varphi'_x, \langle\boldsymbol{\Psi}'^j_x\rangle_{j=1,J}\right]^T = \left[x\frac{\partial\tau_\mathbf{A}}{\partial x}, x\frac{\partial\delta_\mathbf{A}}{\partial x}, \langle x\frac{\partial\mathbf{B}_\mathbf{A}^j}{\partial x}\rangle_{j=1,J}\right]^T \tag{133}$$

We then can then write the above Eqs. (130)–(132) in a vector formulism (as in Eq. (57)):

$$\left[\phi_x, \varphi_x, \langle\boldsymbol{\Psi}^j_x\rangle_{j=1,J}\right]^T = \boldsymbol{\Pi}\left[\phi'_x, \varphi'_x, \langle\boldsymbol{\Psi}'^j_x\rangle_{j=1,J}\right]^T \tag{134}$$

Here, $\boldsymbol{\Pi}$ is a matrix comprising the relevant coefficients, as noted in Eq. (59). Equations (134) and (59) then provide a general framework for preparing linearized optical property inputs necessary for VLIDORT. Computation of $\left[\phi_x, \varphi_x, \langle\boldsymbol{\Psi}^j_x\rangle_{j=1,J}\right]$ can then be achieved by the calculation of $\left[\phi'_x, \varphi'_x, \langle\boldsymbol{\Psi}'^j_x\rangle_{j=1,J}\right]$ for a given parameter x.

Let us first consider the derivation of $\left[\phi'_x, \varphi'_x, \langle\boldsymbol{\Psi}'^j_x\rangle_{j=1,J}\right]$ for certain aerosol optical properties in a given atmospheric layer, i.e., τ_A, ω_A, and β_A^k, where β_A^k indicates one of the elements in the kth aerosol scattering Greek matrix $\mathbf{B}_\mathrm{A}^k$.

For $x = \tau_\mathrm{A}$, we have

$$\phi'_x = \tau_\mathrm{A}\frac{\partial\tau_\mathbf{A}}{\partial\tau_\mathbf{A}} = \tau_\mathrm{A} \tag{135}$$

$$\varphi'_x = \tau_\mathrm{A}\frac{\partial\delta_\mathbf{A}}{\partial\tau_\mathbf{A}} = \tau_\mathrm{A}\omega_\mathrm{A} \tag{136}$$

$$\boldsymbol{\Psi}'^j_x = \tau_\mathrm{A}\frac{\partial\mathbf{B}_\mathbf{A}^j}{\partial\tau_\mathbf{A}} = \mathbf{0} \tag{137}$$

For $x = \omega_\mathrm{A}$, we have

$$\phi'_x = \omega_{\mathrm{A}} \frac{\partial \tau_{\mathbf{A}}}{\partial \omega_{\mathbf{A}}} = 0 \tag{138}$$

$$\varphi'_x = \omega_{\mathrm{A}} \frac{\partial \delta_{\mathbf{A}}}{\partial \omega_{\mathbf{A}}} = \omega_{\mathrm{A}} \tau_{\mathrm{A}} \tag{139}$$

$$\boldsymbol{\Psi}'^{j}_{x} = \omega_{\mathrm{A}} \frac{\partial \mathbf{B}^{j}_{\mathbf{A}}}{\partial \omega_{\mathbf{A}}} = \mathbf{0} \tag{140}$$

For $x = \beta^k_{\mathrm{A}}$, we have

$$\phi'_x = \beta^k_{\mathrm{A}} \frac{\partial \tau_{\mathbf{A}}}{\partial \beta^k_{\mathrm{A}}} = 0 \tag{141}$$

$$\varphi'_x = \beta^k_{\mathrm{A}} \frac{\partial \delta_{\mathbf{A}}}{\beta^k_{\mathrm{A}}} = 0 \tag{142}$$

$$\boldsymbol{\Psi}'^{j}_{x} = \beta^k_{\mathrm{A}} \frac{\partial \mathbf{B}^{j}_{\mathbf{A}}}{\beta^k_{\mathrm{A}}} = \begin{cases} \frac{\delta_{\mathrm{A}} \beta^k_{\mathrm{A}}}{\beta^k} & \text{if } j = k \\ 0 & \text{if } j \neq k \end{cases} \tag{143}$$

Expressions in Table 1 are then derived by substituting equations (135)–(143) into Eq. (134).

The UNL-VRTM tool integrates the VLIDORT with linearized Mie/T-matrix codes, and this combination allows us to generate Stokes vectors and associated analytical Jacobians with respect to any group of aerosol microphysical parameters for two aerosol modes. Thus, we must supply the $\left[\phi'_x, \varphi'_x, \langle \boldsymbol{\Psi}'^{j}_{x} \rangle_{j=1,J}\right]$ quantities for all such parameters. We give an example here, assuming that the aerosols are bimodal, having lognormal size distributions parameterized by geometric standard deviations ($\sigma^{\mathrm{f}}_{\mathrm{g}}$ and $\sigma^{\mathrm{c}}_{\mathrm{g}}$), geometric median radii ($r^{\mathrm{f}}_{\mathrm{g}}$ and $r^{\mathrm{c}}_{\mathrm{g}}$), and non-sphericity parameters (ε^{f} and ε^{c}) for the fine and coarse modes. We note that ε is available only when non-spherical particles are assumed (T-matrix code is applied). Complex refractive indices are $m^{\mathrm{f}}_{\mathrm{r}} - m^{\mathrm{f}}_{\mathrm{i}} i$ and $m^{\mathrm{c}}_{\mathrm{r}} - m^{\mathrm{c}}_{\mathrm{i}} i$. Given these microphysical properties, the linearized Mie/T-matrix codes will compute for each mode the scattering and extinction efficiencies (Q_{sca} and Q_{ext}), the set of expansion coefficients ($\mathbf{B}^{j}_{\mathrm{A}}$) of scattering phase matrix, as well as the derivatives of these quantities with respect to these microphysical properties. The optical thickness for aerosol extinction and scattering and the associated Greek matrix coefficients within for one atmospheric layer can be calculated through

$$\tau_{\mathrm{A}} = \tau^{\mathrm{f}}_{\mathrm{A}} + \tau^{\mathrm{c}}_{\mathrm{A}} = \frac{3 V^{\mathrm{f}}_0 Q^{\mathrm{f}}_{\mathrm{ext}}}{4 r^{\mathrm{f}}_{\mathrm{eff}}} + \frac{3 V^{\mathrm{c}}_0 Q^{\mathrm{c}}_{\mathrm{ext}}}{4 r^{\mathrm{c}}_{\mathrm{eff}}} \tag{144}$$

$$\delta_{\mathrm{A}} = \delta^{\mathrm{f}}_{\mathrm{A}} + \delta^{\mathrm{c}}_{\mathrm{A}} = \frac{3 V^{\mathrm{f}}_0 Q^{\mathrm{f}}_{\mathrm{sca}}}{4 r^{\mathrm{f}}_{\mathrm{eff}}} + \frac{3 V^{\mathrm{c}}_0 Q^{\mathrm{c}}_{\mathrm{sca}}}{4 r^{\mathrm{c}}_{\mathrm{eff}}} \tag{145}$$

$$\mathbf{B}^{j}_{\mathrm{A}} = \frac{\delta^{\mathrm{f}}_{\mathrm{A}} \mathbf{B}^{\mathrm{f}j}_{\mathrm{A}} + \delta^{\mathrm{c}}_{\mathrm{A}} \mathbf{B}^{\mathrm{c}j}_{\mathrm{A}}}{\delta^{\mathrm{f}}_{\mathrm{A}} + \delta^{\mathrm{c}}_{\mathrm{A}}} \tag{146}$$

We can compute vector $\left[\phi'_x, \varphi'_x, \langle \boldsymbol{\Psi}'^j_x \rangle_{j=1,J}\right]$ for a given parameter by differentiating the above Eqs. (144)–(146). For $x = V_0^{\mathrm{f}}$ as an example:

$$\phi'_x = V_0^{\mathrm{f}} \frac{\partial \tau_{\mathbf{A}}}{\partial V_0^{\mathrm{f}}} = V_0^{\mathrm{f}} \frac{3 Q_{\mathrm{ext}}^{\mathrm{f}}}{4 r_{\mathrm{eff}}^{\mathrm{f}}} = \tau_{\mathrm{A}}^{\mathrm{f}} \tag{147}$$

$$\varphi'_x = V_0^{\mathrm{f}} \frac{\partial \delta_{\mathbf{A}}}{\partial V_0^{\mathrm{f}}} = V_0^{\mathrm{f}} \frac{3 Q_{\mathrm{sca}}^{\mathrm{f}}}{4 r_{\mathrm{eff}}^{\mathrm{f}}} = \delta_{\mathrm{A}}^{\mathrm{f}} \tag{148}$$

$$\boldsymbol{\Psi}'^j_x = V_0^{\mathrm{f}} \frac{\partial \mathbf{B}_{\mathbf{A}}^j}{\partial V_0^{\mathrm{f}}} = \frac{\delta_{\mathrm{A}}^{\mathrm{f}}}{\delta_{\mathrm{A}}} (\mathbf{B}_{\mathrm{A}}^{\mathrm{f},j} - \mathbf{B}_{\mathrm{A}}^j) \tag{149}$$

And similarly for $x = r_{\mathrm{g}}^{\mathrm{f}}$, we have

$$\phi'_x = \tau_{\mathrm{A}}^{\mathrm{f}} \left(\frac{r_{\mathrm{g}}^{\mathrm{f}}}{Q_{\mathrm{ext}}^{\mathrm{f}}} \frac{\partial Q_{\mathrm{ext}}^{\mathrm{f}}}{\partial r_{\mathrm{g}}^{\mathrm{f}}} - \frac{r_{\mathrm{g}}^{\mathrm{f}}}{r_{\mathrm{eff}}^{\mathrm{f}}} \frac{\partial r_{\mathrm{eff}}^{\mathrm{f}}}{\partial r_{\mathrm{g}}^{\mathrm{f}}} \right) \tag{150}$$

$$\varphi'_x = \delta_{\mathrm{A}}^{\mathrm{f}} \left(\frac{r_{\mathrm{g}}^{\mathrm{f}}}{Q_{\mathrm{sca}}^{\mathrm{f}}} \frac{\partial Q_{\mathrm{sca}}^{\mathrm{f}}}{\partial r_{\mathrm{g}}^{\mathrm{f}}} - \frac{r_{\mathrm{g}}^{\mathrm{f}}}{r_{\mathrm{eff}}^{\mathrm{f}}} \frac{\partial r_{\mathrm{eff}}^{\mathrm{f}}}{\partial r_{\mathrm{g}}^{\mathrm{f}}} \right) \tag{151}$$

$$\boldsymbol{\Psi}'^j_x = \frac{\varphi'_x}{\delta_{\mathrm{A}}} (\mathbf{B}_{\mathrm{A}}^{\mathrm{f},j} - \mathbf{B}_{\mathrm{A}}^j) + r_{\mathrm{g}}^{\mathrm{f}} \frac{\partial \mathbf{B}_{\mathbf{A}}^{\mathrm{s}j}}{\partial r_{\mathrm{g}}^{\mathrm{f}}} \tag{152}$$

In a similar fashion, we can obtain the vector $\left[\phi'_x, \varphi'_x, \langle \boldsymbol{\Psi}'^j_x \rangle_{j=1,J}\right]$ for other fine-mode aerosol parameters including $\tau_{\mathrm{A}}^{\mathrm{f}}$, $\omega_{\mathrm{A}}^{\mathrm{f}}$, V_0^{f}, $m_{\mathrm{r}}^{\mathrm{f}}$, $m_{\mathrm{i}}^{\mathrm{f}}$, $r_{\mathrm{g}}^{\mathrm{f}}$, $\sigma_{\mathrm{g}}^{\mathrm{f}}$, and ε^{f} (as listed in Table 2). For coarse-mode aerosol parameters, the derivations are the same with superscript 's' replaced by 'c'.

We have implemented various aerosol-loading vertical profiles into the UNL-VRTM, including uniform, exponential-decreasing, and quasi-Gaussian profile shapes (Sect. 2.3). Derivatives of layer aerosol optical thickness with respect to these profile parameters [such as H in Eq. 31, γ and z_{peak} in Eq. (32)] are also included in order to calculate Jacobians of Stokes vector to these parameters, and the vectors $\left[\phi'_x, \varphi'_x, \langle \boldsymbol{\Psi}'^j_x \rangle_{j=1,J}\right]$ for these derivatives are also shown in Table 2.

References

Baldridge AM, Hook SJ, Grove CI, Rivera G (2009) The ASTER spectral library version 2.0. Remote Sens Environ 113:711–715

Bak J, Kim JH, Liu X, Chance K, Kim J (2013) Evaluation of ozone profile and tropospheric ozone retrievals from GEMS and OMI spectra. Atmos Meas Tech 6:239–249

Berk A, Cooley TW, Anderson GP et al (2004) MODTRAN5: a reformulated atmospheric band model with auxiliary species and practical multiple scattering options. Proc SPIE 5571 Remote Sensing of Clouds and the Atmosphere IX. https://doi.org/10.1117/12.564634

Bodhaine BA, Wood NB, Dutton EG et al (1999) On Rayleigh optical depth calculations. J Atmos Ocean Tech 16:1854–1861

Boucher O, Randall D, Artaxo P, (2013) Clouds and Aerosols. In: Stocker TF, Qin D, Plattner FG-K et al (ed) Climate Change, et al (2013) The Physical Science Basis. Cambridge University Press, Cambridge, UK and New York, USA

Chen X, Wang J, Liu Y et al (2017) Angular dependence of aerosol information content in CAPI/TanSat observation over land: effect of polarization and synergy with A-train satellites. Remote Sens Environ 196:163–77

Chen X, Wang J, Liu Y et al (2018) Sensitivity of CO_2 retrieval from space to the shape of aerosol particles: a theoretical analysis. Presented in AGU Fall Meeting 2018, Washington DC

Clough SA, Kneizys FX, Davies RW (1989) Line shape and the water vapor continuum. Atmos Res 23:229–241

Coulson KL, Dave JV, Sekera Z (1960) Tables related to radiation emerging from a planetary atmosphere With Rayleigh scattering. University of California Press, Berkeley, California, USA

Coulson KL (1988) Polarization and intensity of light in the atmosphere. VA A Deepak Pub, Hampton, Virginia, USA

Cox C, Munk W (1954) Measurement of the roughness of the sea surface from photographs of the Sun's Glitter. J Opt Soc Am 44:838–850

de Rooij WA, van der Stap CCAH (1984) Expansion of Mie scattering matrices in generalized spherical functions. Astron Astrophy 131:237–248

Diner D, Brauer M, Bruegge C et al (2018) Advances in multiangle satellite remote sensing of speciated airborne particulate matter and association with adverse health effects: from MISR to MAIA. J Appl Remote Sens 12:042603

Ding S, Wang J (2016) Xu X. Polarimetric remote sensing in oxygen A and B bands: sensitivity study and information content analysis for vertical profile of aerosols. Atmos Meas Technol 9:2077–92

Downing HD, Williams D (1975) Optical constants of water in the infrared. J Geophys Res 180:1656–61

Dubovik O, King MD (2000) A flexible inversion algorithm for retrieval of aerosol optical properties from Sun and sky radiance measurements. J Geophys Res 105(20):673–96

Dubovik O, Holben B, Eck TF et al (2002) Variability of absorption and optical properties of key aerosol types observed in worldwide locations. J Atmos Sci 59:590–608

Dubovik O, Sinyuk A, Lapyonok T et al (2006) Application of spheroid models to account for aerosol particle nonsphericity in remote sensing of desert dust. J Geophys Res 111:D11208

Dubovik O, Herman M, Holdak A et al (2011) Statistically optimized inversion algorithm for enhanced retrieval of aerosol properties from spectral multi-angle polarimetric satellite observations. Atmos Meas Tech 4:975–1018

Dubovik O, Li Z, Mishchenko MI et al (2019) Polarimetric remote sensing of atmospheric aerosols: Instruments, methodologies, results, and perspectives. J Quant Spectrosc Radiat Transf 224:474–511

Dubuisson P, Frouin R, Dessailly D et al (2009) Estimating the altitude of aerosol plumes over the ocean from reflectance ratio measurements in the O2 A-band. Remote Sens Environ 113:1899–911

Evans KF, Stephens GL (1991) A new polarized atmospheric radiative transfer model. J Quant Spectrosc Radiat Transf 46:413–423

Fedarenka A, Dubovik O, Goloub P et al (2016) Utilization of AERONET polarimetric measurements for improving retrieval of aerosol microphysics: GSFC, Beijing and Dakar data analysis. J Quant Spectrosc Radiat Transf 179:72–97

Fougnie B, Marbach T, Lacan A et al (2018) The multi-viewing multi-channel multi-polarisation imager Overview of the 3MI polarimetric mission for aerosol and cloud characterization. J Quant Spectrosc Radiat Transf 219:23–32

Garcia RDM, Siewert CE (1989) The FN method for radiative transfer models that include polarization effects. J Quant Spectrosc Radiat Transf 41:117–145

Gautschi W (1970) Efficient computation of the complex error function. SIAM J Numer Anal 7:187–198
Giles DM, Sinyuk A, Sorokin MG et al (2019) Advancements in the Aerosol Robotic Network (AERONET) Version 3 database automated near-real-time quality control algorithm with improved cloud screening for Sun photometer aerosol optical depth (AOD) measurements. Atmos Meas Tech 12:169–209
Hale GM, Querry MR (1973) Optical constants of water in the 200-nm to 200-m wavelength region. Appl Opt 12:555–563
Hansen JE, Travis LD (1974) Light scattering in planetary atmospheres. Space Sci Rev 16:572–610
Hapke B (1993) Theory of reflectance and emittance spectroscopy. Cambridge University Press, Cambridge, UK
Hess M, Koepke P, Schult I (1998) Optical properties of aerosols and clouds: the software package OPAC. B Am Meteorol Soc 79:831–844
Hoff RM, Christopher SA (2009) Remote sensing of particulate pollution from space: have we reached the promised land? J Air Waste Manag Assoc 59:6645–6675
Holben BN, Eck TF, Slutsker I et al (1998) AERONET A federated instrument network and data archive for aerosol characterization. Remote Sens Environ 66:1–16
Hou W, Wang J, Xu X et al (2016) An algorithm for hyperspectral remote sensing of aerosols: 1. Development of theoretical framework. J Quant Spectrosc Radiat Transf 178:400–15
Hou W, Wang J, Xu X, Reid JS (2017) An algorithm for hyperspectral remote sens- ing of aerosols: 2. Information content analysis for aerosol parameters and principal components of surface spectra. J Quant Spectrosc Radiat Transf 192:14–29
Hou W, Li Z, Wang J et al (2018) Improving remote sensing of aerosol microphysical properties by near-infrared polarimetric measurements over vegetated land: information content analysis. J Geophys Res Atmos 123:2215–2243
Hou W, Li Z, Zheng F, Qie L (2018) Retrieval of aerosol microphysical properties based on the optimal estimation method: Information content analysis for satellite polarimetric remote sensing measurements. Int Arch Photogramm, Remote Sensing Spatial Informat Sci XLII-3:533–537
Hovenier JW, van der Mee CVM (1983) Fundamental relationships relevant to the transfer of polarized light in a scattering atmosphere. Astron Astrophys 128:1–16
Hovenier JW, Mee C, Domke H (2004) Transfer of polarized light in planetary atmospheres. Kluwer Academic Publishers, Dordrecht, The Netherlands
Jackson JM, Liu H, Laszlo I et al (2013) Suomi NPP VIIRS aerosol algorithms and data products. J Geophys Res Atmos 118(12):673–89
Kahn R, West R, McDonald D, Rheingans B (1997) Sensitivity of multiangle remote sensing observations to aerosol sphericity. J Geophys Res 102(16):861–70
Kalashnikova OV, Kahn R (2006) Ability of multiangle remote sensing observations to identify and distinguish mineral dust types: 2. Sensitivity over dark water. J Geophys Res 111:D11207
Kaufman YJ, Tanre D, Boucher O (2002) A satellite view of aerosols in the climate system. Nature 419:215–223
Kokhanovsky AA, Breon FM, Cacciari A et al (2007) Aerosol remote sensing over land: a comparison of satellite retrievals using different algorithms and instruments. Atmospheric Res 85:372–394
Kokhanovsky AA, Davis A, Cairns B et al (2015) Space-based remote sensing of atmospheric aerosols: the multi-angle spectro-polarimetric frontier. Earth-Sci Rev 145:85–116
Kou L, Labrie D, Chylek P (1993) Refractive indices of water and ice in the 0.65 to 2.5-m spectral range. Appl Opt 32:3531–40
Levy RC, Remer LA, Mattoo S et al (2007) Second generation operational algorithm: retrieval of aerosol properties over land from inversion of moderate resolution imaging spectroradiometer spectral reflectance. J Geophys Res 112:D13211
Li X, Strahler AH (1992) Geometrical-optical bidirectional reflectance modeling of the discrete crown vegetation canopy: effect of crown shape and mutual shadowing. IEEE T Geosci Remote 30:276–292

Li Z, Hou W, Hong J et al (2018) Directional Polarimetric Camera (DPC): monitoring aerosol spectral optical properties over land from satellite observation. J Quant Spectrosc Radiat Transf 218:21–37

Liou KN (2002) An Introduction to Atmospheric Radiation. Academic Press, San Diego, California, USA

Litvinov P, Hasekamp O, Cairns B (2011) Models for surface reflection of radiance and polarized radiance: comparison with airborne multi-angle photopolarimetric measurements and implications for modeling top-of-atmosphere measurements. Remote Sens Environ 115:781–792

Lucht W, Schaaf CB, Strahler AH (2000) An algorithm for the retrieval of albedo from space using semiempirical BRDF models. IEEE T Geosci Remote 38:977–998

Maignan F, Bron F-M, Fdle E, Bouvier M (2009) Polarized reflectances of natural surfaces: spaceborne measurements and analytical modeling. Remote Sens Environ 113:2642–2650

McClatchey RA, Fenn RW, Selby JEA et al (1972) Optical properties of the atmosphere, 3rd edn. Air Force Cambridge Research Labs, Hanscom AFB, Massachusetts, USA

McHardy TM, Zhang J, Reid JS et al (2015) An improved method for retrieving nighttime aerosol optical thickness from the VIIRS Day/Night Band. Atmos Meas Tech 8:4773–4783

Meng Z, Yang P, Kattawar GW et al (2010) Single-scattering properties of tri-axial ellipsoidal mineral dust aerosols: a database for application to radiative transfer calculations. J Aerosol Sci 41:501–512

Meyer K, Platnick S, Oreopoulos L, Lee D (2013) Estimating the direct radiative effect of absorbing aerosols overlying marine boundary layer clouds in the southeast Atlantic using MODIS and CALIOP. J Geophys Res 118:4801–15

Minneaert M (1941) The reciprocity principle in lunar photometry. J Astrophys 93:403–410

Mishchenko MI, Cairns B, Hansen JE et al (2004) Monitoring of aerosol forcing of climate from space: analysis of measurement requirements. J Quant Spectrosc Radiat Transf 88:149–161

Mishchenko MI, Travis LD (1997) Satellite retrieval of aerosol properties over the ocean using polarization as well as intensity of reflected sunlight. J Geophys Res 102:16989–17013

Mishchenko MI, Travis LD (1998) Capabilities and limitations of a current FORTRAN implementation of the T-matrix method for randomly oriented, rotationally symmetric scatterers. J Quant Spectrosc Radiat Transf 60:309–324

Mishchenko MI, Travis LD, Lacis AA (2002) Scattering, absorption, and emission of light by small particles. Cambridge University Press, Cambridge, UK

Mishchenko MI, Cairns B, Hansen JE et al (2007) Accurate monitoring of terrestrial aerosols and total solar irradiance: introducing the glory mission. B Am Meteorol Soc 88:677–691

Mlawer EJ, Payne VH, Moncet J-L et al (2012) Development and recent evaluation of the MT_CKD model of continuum absorption. Phil Trans R Soc A 370:2520–2556

Myhre G, Shindell D, Breon F-M (2013) Anthropogenic and natural radiative forcing. In: Stocker TF, Qin D, Plattner FG-K et al (ed) Climate change, The Physical Science Basis. Cambridge University Press, Cambridge, UK and New York, USA

Nakajima T, King MD, Spinhirne JD, Radke LF (1991) Determination of the optical thickness and effective particle radius of clouds from reflected solar radiation measurements. Part II: Marine stratocumulus observations. J Atmos Sci 48:728–51

Natraj V, Hovenier JW (2012) Polarized light reflected and transmitted by thick Rayleigh scattering atmospheres. Astrophys J 748:28

Omar AH, Tzortziou M, Coddington O, Remer LA (2018) Plankton aerosol, cloud, ocean ecosystem mission: atmosphere measurements for air quality applications. J Appl Remote Sens 12:042608

Orphal J, Chance K (2003) Ultraviolet and visible absorption cross-sections for HITRAN. J Quant Spectrosc Radiat Transf 82:491–504

Penndorf R (1957) Tables of the refractive index for standard air and the Rayleigh scattering coefficient for the spectral region between 0.2 and 20.0 and their application to atmospheric optics. J Opt Soc Amer 47:176–182

Platnick S, King MD, Ackerman SA et al (2003) The MODIS cloud products: algorithms and examples from Terra. IEEE Trans Geosci Remote Sens 41:459–73

Rahman H, Pinty B, Verstraete M (1993) Coupled surface atmosphere reectance (CSAR) model: 2. Semi-empirical surface model usable with NOAA AVHRR data. J Geophys Res 98:20791–20801
Remer LA, Kaufman YJ, Tanre D et al (2005) The MODIS aerosol algorithm, product, and validation. J Atmos Sci 62:947–973
Ricchiazzi P, Yang S, Gautier C, Sowle D (1998) SBDART: A research and teaching software tool for plane-parallel radiative transfer in the earth's atmosphere. B Am Meteorol Soc 79:2101–2114
Rodgers CD (2000) inverse methods for atmospheric sounding: theory and practice. World Scientific, Singapore
Ross JK (1981) The radiation regime and architecture of plant stands. Junk Publishers, The Hague, The Netherlands, Dr. W
Rothman LS, Gordon IE, Barbe A et al (2009) The HITRAN 2008 molecular spectroscopic database. J Quant Spectrosc Radiat Transf 110:533–572
Rothman LS, Gordon IE, Babikov Y et al (2013) The HITRAN2012 molecular spectroscopic database. J Quant Spectrosc Radiat Transf 130:4–50
Roujean J-L, Leroy M, Deschamps PY (1992) A bidirectional model of the earth's surface for the correction of remote sensing data. J Geophys Res 97:20455–20468
Sancer M (1969) Shadow-corrected electromagnetic scattering from a randomly-rough ocean surface. IEEE Trans Antennas Propag, AP-17:557–585
Sanders AFJ, de Haan JF, Sneep M et al (2015) Evaluation of the operational aerosol layer height retrieval algorithm for Sentinel-5 Precursor: application to O2 A band observations from GOME-2A. Atmos Meas Tech 8:4947–4977
Seinfeld JH, Pandis SN (2006) Atmospheric chemistry and physics: from air pollution to climate change, 2nd edn. John Wiley & Sons Inc., Hoboken, New Jersey, USA
Shannon CE (1948) A mathematical theory of communication. Bell Syst Tech J 27:379–423
Spurr R (2004) A new approach to the retrieval of surface properties from earthshine measurements. J Quant Spectrosc Radiat Transf 83:15–46
Spurr R (2006) VLIDORT: a linearized pseudo-spherical vector discrete ordinate radiative transfer code for forward model and retrieval studies in multilayer multiple scattering media. J Quant Spectrosc Radiat Transf 102:316–342
Spurr R (2008) LIDORT and VLIDORT: Linearized pseudo-spherical scalar and vector discrete ordinate radiative transfer models for use in remote sensing retrieval problems. In: Kokhanovsky A (ed) Light scattering reviews 3. Springer, Berlin Heidelberg
Spurr R, Wang J, Zeng J et al (2012) Linearized T-matrix and Mie scattering computations. J Quant Spectrosc Radiat Transf 113:425–439
Spurr R, Christi M (2014) On the generation of atmospheric property Jacobians from the (V)LIDORT linearized radiative transfer models. J Quant Spectrosc Radiat Transf 142:109–115
Spurr R, Christi M (2019) The LIDORT and VLIDORT linearized scalar and vector discrete ordinate radiative transfer models: updates in the last 10 years. In: Kokhanovsky A (ed) Springer Series in Light Scattering 3: Radiative Transfer and Light Scattering. Springer International Publishing, Cham
Tanre D, Breon FM, Deuze JL, et al (2011) Remote sensing of aerosols by using polarized, directional and spectral measurements within the A-Train: the PARASOL mission. Atmos Meas Tech 4:1383–95
Tao M, Chen L, Wang Z et al (2017) Evaluation of MODIS deep blue aerosol algorithm in desert region of East Asia: ground validation and inter-comparison. J Geophys Res Atmos 122:10357–68
Torres O, Bhartia PK, Herman JR et al (1998) Derivation of aerosol properties from satellite measurements of backscattered ultraviolet radiation: theoretical basis. J Geophys Res 103:17099–110
Torres O, Tanskanen A, Veihelmann B et al (2007) Aerosols and surface UV products from ozone monitoring instrument observations: an overview. J Geophys Res 112: D24S47
Veefkind JP, Aben I, McMullan K et al (2012) TROPOMI on the ESA sentinel-5 precursor: a GMES mission for global observations of the atmospheric composition for climate, air quality and ozone layer applications. Remote Sens Environ 120:70–83

Wang J, Xu X, Ding S et al (2014) A numerical testbed for remote sensing of aerosols, and its demonstration for evaluating retrieval synergy from geostationary satellite constellation. J Quant Spectrosc Radiat Transf 146:510–528

Wang J, Aegerter C, Xu X, Szykman J (2016) Potential application of VIIRS Day/Night Band for monitoring nighttime surface PM2.5 air quality from space. Atmos Environ 124:55–63

Wang Y, Wang J, Levy RC et al (2017) MODIS retrieval of aerosol optical depth over turbid coastal water. Remote Sens 9:595

Wanner W, Li X, Strahler AH (1995) On the derivation of kernels for kernel-driven models of bidirectional reflectance. J Geophys Res Atmos 100:21077–89

World Health Organization (2017) Ambient air pollution: A global assessment of exposure and burden of disease. WHO Document Production Services, Geneva, Switzerland

Xu X, Wang J (2015) Retrieval of aerosol microphysical properties from aeronet photopolarimetric measurements: 1. Information content analysis. J Geophys Res Atmos 120:7059–78

Xu X, Wang J, Zeng J et al (2015) Retrieval of aerosol microphysical properties from aeronet photopolarimetric measurements: 2. A new research algorithm and case demonstration. J Geophys Res Atmos 120:7079–98

Xu X, Wang J, Wang Y et al (2017) Sense size-dependent dust loading and emission from space using reflected solar and infrared spectral measurements: an observation system simulation experiment. J Geophys Res Atmos 122:8233–54

Xu X, Wang J, Wang Y et al (2017) Passive remote sensing of altitude and optical depth of dust plumes using the oxygen A and B bands: first results from EPIC/DSCOVR at Lagrange-1 point. Geophys Res Lett 44:7544–54

Xu X, Wang J (2018) Users guide for UNLVRTM: a UNified linearized vector radiative transfer model version 2.0.1. https://unl-vrtm.org (accessed 12 Jan 2019)

Xu X, Wang J, Wang Y, Kokhanovsky A (2018) Passive remote sensing of aerosol height. in Islam et al (ed) Remote sensing of aerosols, clouds, and precipitation. Elsevier, Cambridge, MA, USA

Xu X, Wang J, Wang Y et al (2018) Detecting layer height of smoke aerosols over vegetated land and water surfaces via oxygen absorption bands: Hourly results from EPIC/DSCOVR satellite in deep space. Atmos Meas Tech Discuss. https://doi.org/10.5194/amt-2018-414

Xu X, Wang J, Zeng J et al (2018) A pilot study of shortwave spectral fingerprints of smoke aerosols above liquid clouds. J Quant Spectrosc Radiat Transf 221:38–50

Zhou M, Wang J, Xu X, Roudini S (2018) Model development for mighttime light radiative transfer and application to VIIRS Day Night Band (DNB). Presented in AGU Fall Meeting 2018, Washington DC

Zoogman P, Liu X, Suleiman RM et al (2017) Tropospheric emissions: monitoring of pollution (TEMPO). J Quant Spectrosc Radiat Transf 186:17–39